DOSIMETRIC EVALUATION AND VERIFICATION OF TREATMENT PLANNING SYSTEMS

by

Cathy Neath

A thesis presented to the Faculty of Graduate Studies of the University of Manitoba in partial fulfillment of the requirements for the degree of

MASTER OF SCIENCE

Department of Physics

University of Manitoba

Winnipeg, Manitoba, Canada

THE UNIVERSITY OF MANITOBA

FACULTY OF GRADUATE STUDIES

*****

COPYRIGHT PERMISSION PAGE

Dosimetric Evaluation and Verification of Treatment Planning Systems

BY

Cathy Neath

A Thesis/Practicum submitted to the Faculty of Graduate Studies of The University of Manitoba in partial fulfillment of the requirements of the degree of

Master of Science

ACKNOWLEDGEMENTS

I would like to thank my supervisor, Dr. S. Rathee, for his guidance, support and patience. In addition I would like to thank the physicists and students at CancerCare Manitoba, especially Dr. S. Pistorius, Dr. J. Lewis, and Anita Berndt, for their assistance and knowledgeable advice. Finally, I would like to thank my friends and family for their support and encouragement.

The use of the facilities at CancerCare Manitoba is acknowledged. Financial support for this work was, in part, provided by CancerCare Manitoba.

ABSTRACT

The accuracy of treatment planning system's (TPS) external photon beam dose calculations for complex fields involving the use of blocks, multi-leaf collimator (MLC), virtual wedges and asymmetric jaws are evaluated in this study. The treatment planning systems investigated were: (1) Helax-TMS (Version 4.1) which implements an energy fluence based model of the treatment head of a linac and pencil beam algorithm for determination of the dose in the patient; and (2) CMS FOCUS (Version 2.5) which employs the Clarkson's algorithm and a scatter phantom ratio model to calculate the dose. Measured output factors (OF) and head scatter factors (HSF) for several square fields, fields formed by independent jaws, MLC formed fields and blocked fields were determined and compared with OFs and HSFs predicted by the TPSs. OFs for virtual wedges, formed by independent jaws, were also measured and compared with those predicted by CMS and TMS. The output in-phantom is expressed relative to the output for a 10x10 field at the depth of maximum dose (dmax). The output in-air is expressed relative to the output for a 10x10 field at the source to axis distance (SAD) of 100 cm. In addition, several isodose distributions resulting from independent jaws, MLC, and blocks were measured and compared with isodose distributions as predicted by CMS and TMS. All measurements were performed on the Siemens dual energy (6MV and 23MV) linac (KD2B), equipped with a MLC and virtual wedge™.

CMS and TMS performed accurately for the square (<2.0%), asymmetric (<2.0%) and blocked fields (<3.0%). CMS demonstrated difficulty (<5%) for calculations of MLC fields since the MLC head scatter model is not implemented in CMS-FOCUS. The virtual wedge OF calculations were, in general, inaccurate. The deviations observed for TMS

were as large as 4.6% for the 60° virtual wedge. Deviations as large as –3.6% were observed for CMS calculated virtual wedge OFs. For the isodose distributions, both CMS and TMS performed accurately in the low gradient central beam region. TMS dose calculations were superior in comparison to CMS in the low gradient inner beam, high gradient, and penumbra region, particularly for the block and MLC fields..

In addition, a method of independent verification of the monitor unit calculations of TMS was developed. This method, designed and implemented in an EXCEL spreadsheet, uses measured beam data to calculate the monitor units for the beams designed by TMS. In general, the average deviation between TMS and this method for linac plans is less than 2% while for a ^{60}Co treatment unit is less than 4%. The MU calculation program successfully provides an independent verification of MUs calculated by TMS.

TABLE OF CONTENTS

TABLE OF FIGURES

1 Introduction

Radiation therapy is the process of using ionizing (and in some cases non-ionizing) radiation to treat malignant disease. The main goal is to cure the patient by eliminating the malignant disease while minimizing complications. This is achieved by delivering a large uniform dose to the planning target volume, encompassing the tumor, while minimizing the dose to nearby normal organs and tissues. The process is complex and involves a series of steps, including patient diagnosis, determination of the treatment volume, planning the treatment, and finally delivery and verification of the treatment. Each of the above steps inherently involves uncertainties, which have a direct impact on the success of the treatment. This particular study investigates the ability of computerized treatment planning systems to calculate the radiation dose being delivered to the patient undergoing treatment.

Computerized treatment planning systems play a significant role in the process of radiation therapy treatment design and in achieving it's goal [Fra 98]. In particular, they acquire and display patient anatomical information and perform dose calculations within the patient according to the plan designed by the user. The optimal treatment plan, customized to treat the patient, is therefore determined. Dose calculations are performed using models, which incorporate measured beam data as well as anatomical information of the patient derived from CT images. In the conventional approach, these models are empirical and obtain treatment beam parameters by interpolation from measured data. The newer, more sophisticated treatment planning systems model the radiation transport through the patient. However, due to the complexity of the processes involved in

radiation interactions with matter, all models include approximations, inevitably leading to uncertainties in the dose calculations and limitations of the treatment planning computers [Fra 98]. Furthermore, significant technological improvement in the treatment beam delivery systems in the past decade has further increased the complexity of the treatment planning process. Some of these improvements include multi-leaf collimators (MLC), virtual wedges, and asymmetric jaws. These advances, although desirable, offer a challenge in terms of their evaluation and may lead to further uncertainties in the dose calculations. Uncertainties in the dose calculations limit the ability of the treatment plan in achieving it's goal, ie. curing the patient. In particular, overestimating the dose to the tumor, and underestimating the dose to nearby critical structures will result in an increased risk of complications as well as reduced probability of eliminating the malignant disease.

The purpose of this study was to evaluate the accuracy of external photon beam dose calculations for complex fields involving the use of blocks, MLC, virtual wedges, and asymmetric jaws. Similar investigations of other TPSs have been done [Lyd 98]. Specifically, measured output factors and head scatter factors for several square fields, fields formed by independent jaws, MLC formed fields, and blocked fields were determined and compared with output factors and head scatter factors as predicted by the treatment planning systems for corresponding fields. Output factors for virtual wedges, formed by independent jaws, were also measured and compared with those predicted by the treatment planning systems. In addition, several isodose distributions resulting from independent jaws, MLC and blocks, were measured and compared with isodose distributions as predicted by the treatment planning systems for similar situations.

In particular, two treatment planning systems were investigated: (1) Helax-TMS (Version 4.1) which implements an energy fluence based model of the treatment head of a linac and pencil beam algorithm for determination of the dose in the patient [AT 91 & Ahn 92a]; and (2) CMS FOCUS (Version 2.5) which employs a simpler method, namely Clarkson's algorithm and a scatter phantom ratio (SPR) model, to calculate the dose [CMS]. This study determines the relative accuracy of these treatment planning systems and demonstrates which treatment planning system can more accurately model a given clinical situation. The remainder of this chapter is committed to reviewing the dose formalisms and models implemented in the two treatment planning systems under investigation. This will provide the background necessary for an understanding and confidence in the dose calculated by the treatment planning systems.

1.1 Dose Formalism and Models in Helax-TMS

The Helax TMS system is a 3D treatment planning system, which calculates the dose in the patient for all customized treatment plans from an energy fluence distribution, energy deposition kernels, and convolution models. The dose calculations are performed in a two step procedure. Firstly, energy fluence matrices, which describe the energy per unit area, traversing a cross section of an incident beam on the patient produced by a linear accelerator, are derived. Secondly, a pencil beam algorithm is used to calculate the dose distribution in the patient from first principles using the photon beam energy fluence and a pencil beam kernel. A pencil beam kernel is a type of energy deposition kernel describing the energy deposited, per unit mass, per unit fluence, in a semi-infinite medium from a point monodirectional beam [TMS]. The use of an energy fluence matrix

allows for a general and flexible description of the characteristics of a photon beam [AAC 98].

1.1.1 Energy Fluence from a Clinical Beam

The basis of the Helax-TMS dose calculations is the energy fluence of a treatment unit beam. Energy fluence describes the amount of radiant energy per area traversing a cross section of a radiation beam. More specifically, an energy fluence distribution, $\Psi_{tot}(x,y)$, is the amount of radiant energy per area ΔA at position (x,y) traversing a plane perpendicular to the beam, and is given by

$$\Psi_{tot}(x,y) = \sum_{E} \frac{N_E(x,y) \cdot E}{\Delta A}. \qquad 1.1$$

The radiant energy is determined by the product of the number of photons $N_E(x,y)$, having energy E at (x,y), and the energy E of the photons, summed over all energies. The coordinates (x,y) are defined at a particular reference distance, z_o from the source, usually taken to be the isocentre [Helax].

The total energy fluence can be divided into two parts: (1) the primary energy fluence, $\Psi_{prim}(x,y)$, due to unscattered primary photons; and (2) the scattered energy fluence, $\Psi_{cont}(x,y)$, due to scattered or contaminating photons. Furthermore, the scatter radiation component can be separated into three groups: (1) *flattening filter effective scatter, $\Psi_f(A;x,y)$,* including scatter from the flattening filter and primary collimator; (2) *collimator scatter, $\Psi_c(A;x,y)$,* arising from scatter interactions at the edge surfaces of the beam collimating devices, including upper and lower secondary collimators, MLC, and

blocks; and (3) *modulator scatter,* $\Psi_m(A;x,y)$, from wedges, filters, and trays. The sources of scattered radiation are illustrated below in Figure 1-1.

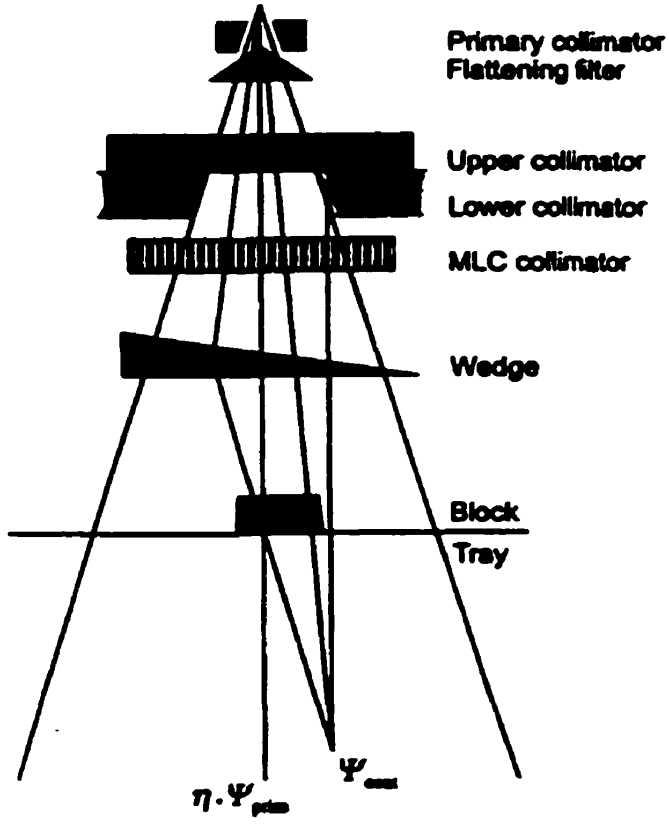

Figure 1-1 *Sources of scatter radiation: (1) Flattening filter and primary collimators (flattening filter effective scatter); (2) collimators, and block edges (collimator scatter); and (3) modulators including wedges, filters, and trays (modulator scatter).*[Helax]

The influence of the modulating devices on the primary energy fluence is taken into account by a modulation correction function, denoted by η(x,y), applied to the primary energy fluence. The total energy fluence for a given point (x,y) at the reference distance z_o is given by

1.2 $$\Psi_{tot}(A;x,y) = \eta(x,y)\Psi_{prim}(x,y) + \Psi_{cont}(A;x,y)$$

where A represents the aperature and

1.3 $$\Psi_{cont}(A;x,y) = \Psi_f(A;x,y) + \Psi_c(A;x,y) + \Psi_m(A;x,y).$$

The primary energy fluence can also be broken down into a reference energy fluence level, Ψ_o, on the beam axis at z_o and a relative distribution function, f(x,y), as follows

1.4 $$\Psi_{prim}(x,y) = \Psi_o \cdot f(x,y).$$

Equation 1.2 can now be written as

1.5 $$\Psi_{tot}(A;x,y) = \Psi_o \cdot \eta(x,y) \cdot f(x,y) + \Psi_{cont}(A;x,y)$$

Finally, a relative energy fluence distribution is obtained by dividing equation 1.5 by the reference level, Ψ_o, as follows

1.6 $$\frac{\Psi_{tot}(A;x,y)}{\Psi_o} = \eta(x,y) f(x,y) + \frac{\Psi_{cont}(A;x,y)}{\Psi_o}$$

The incident beam can therefore be described by three relative energy fluence matrices: (1) a primary fluence matrix, f(x,y); (2) a head scatter fluence matrix, Ψ_{cont}/Ψ_o; and (3) a modulation matrix, $\eta(x,y)$, describing the modulation of the primary energy fluence.

1.1.2 Modeling the Energy Fluence Distribution

The primary and head scatter fluence matrices are derived during the beam set-up procedure and stored in two separate matrices for later use during dose calculations. The lateral relative energy fluence distribution, f(x,y) is derived via beam characterization and is discussed later in section 1.1.3. The following is a discussion of the modeling of the energy fluence distributions: (1) the modulation of the primary energy fluence; and (2) the modeling of the head scatter fluence. Since blocks are not treated as explicit head

scatter sources, the modulation induced by blocks is discussed in a third section titled *Modulation by Blocks*.

1.1.2.1 Modulation of the Primary Energy Fluence

Modulation of the primary energy fluence is separated into two groups: (1) modulation by attenuators, including physical wedges, compensators and trays; and (2) modulation by dynamic collimation, such as for virtual or dynamic wedges and dynamic MLC.

1.1.2.1.1 Modulation by Attenuators

The modulation of the primary energy fluence produced by wedges and filters is described by

$$\eta(x,y) = \frac{\int \Psi_E e^{-k_\mu \mu(E) t(x,y)} dE}{\int \Psi_E dE} \tag{1.7}$$

where Ψ_E is the effective energy spectrum, t(x,y) is the thickness of the attenuator at (x,y), $\mu(E)$ is the narrow beam attenuation coefficient for the attenuator material for photons of energy E, and k_μ is a correction factor applied to filter medium mass attenuation coefficients, equal to unity for wedges. Specifically, the correction factor, k_μ, is introduced to account for: inherent uncertainties in the attenuation coefficients; spectrum uncertainties; and the neglect of multiple scatter in the above proposed model for modulation of primary unscattered photons. The k_μ values have been found to be less than unity, as one would expect due to the neglect of multiple scatter [Ahn 95b]. It is determined empirically by minimizing the deviation between dose ratio measurements

and calculations. A further discrepancy in the tabulated attenuation coefficients is that they include all of the coherent scatter, while the forward peaked coherent scatter at small angles more appropriately blurs the source rather than attenuate the beam [Ahn 95b]. This phenomenon is accounted for by an additional correction factor, $k_{\Delta\mu coh}(x,y)$, derived from an attenuation calculation [Ahn 95b]. The values of $k_{\Delta\mu coh}(x,y)$, are greater than unity and increase with increasing filter atomic number. Incorporating these correction factors into equation 1.7 gives the resultant effective modulation of the primary energy fluence due to the attenuator, ie.,

1.8
$$\hat{\eta}(x,y) = k_{\Delta\mu_{coh}} \frac{\int \Psi_E e^{-k_\mu \mu(E) t(x,y)} dE}{\int \Psi_E dE}.$$

The modulation matrix is evaluated by varying the modulation (ie. t), as calculated above, while fitting the calculated dose to measured dose from star profile measurements, obtained at a depth of 10cm in a water phantom. Thus, there is no explicit use of a wedge factor. A limitation of this model is that the energy fluence is assumed to be independent of the position in the beam, therefore, it does not account for off-axis softening of the primary energy fleunce spectrum.

This model is also used for determination of transmission through trays, however, with the correction factors set to unity. The specifications of the trays including the thickness, mass density and composition are stored in the Helax database, and the user selects from the available selection. The monoenergetic attenuation coefficients are calculated using the mass density and composition of the tray material from standard tables [Hig 92].

1.1.2.1.2 Modulation by Dynamic Collimation

Dynamic collimation indicates that the collimating device (secondary collimators or MLC) defining the field is moving during beam delivery, as opposed to static collimation where the collimating devices remain stationary. The modulation induced by dynamic collimation [Helax] is determined from: (1) the modulation induced by the transmission through the moving collimators, $\eta_{colltrans}$; (2) a collimating function C[A(m);x,y], which determines whether a point (x,y) is inside or outside the dynamic field A(m), as a function of relative delivered monitor units (m); and (3) a monitor correction factor describing the perturbation of the monitor signal from collimator backscatter, B(m); ie.,

$$\eta(x,y) = \eta_{colltrans} + (1 - \eta_{colltrans}) \frac{\int_0^1 B(m) \cdot C[A(m);x,y]dm}{\int_0^1 B(m)dm} \tag{1.9}$$

where A(m) is the dynamic field size, and m = Total monitor units delivered at a given dynamic jaw position / Total monitor units to be delivered for the field. The collimating function takes on the value of 1 inside the bounds of the dynamic field (A(m)), and zero outside. The monitor correction factor, B(m), is defined [Ahn 92b] as

$$B(m) = \frac{1}{1 + \frac{M_b(m)}{M_0}} \tag{1.10}$$

where M_b is the MU signal proportional to the energy fluence of backscattered particles and M_o is the MU signal proportional to the forward energy fluence. M_b is described by: the magnitude of the primary energy fluence (Ψ_0) incident on the collimator jaws

corrected for the inverse square law by $(z_o/z_{coll})^2$, where z_{coll} is the distance from the source to the face of the collimators, z_o is the source to isocenter distance; a view factor (F) describing the fraction of radiant energy emanating from the scattering element, which strikes the monitor chamber; and a proportionality constant k_{back} relating the fluence to the monitor chamber signal, ie., [Ahn 92b]

1.11 $$M_b(m) = k_{back} F(m) \frac{\Psi_0 z_0^2}{z_{coll}^2}, \qquad F(m) = \iint_{\substack{Irradiated \\ Col\,lim\,ator \\ Area}} \frac{\cos\theta_A(m)}{\pi(z_{coll} - z_{mon})^2} dA$$

where k_{back} is determined empirically (see section 1.1.2.2.1), z_{mon} is the distance from the source to the monitor chamber, and θ_A is the view angle as shown in Figure 1-2. Substitution of equations (1.11) into (1.10) results in the following expression for B,

1.12 $$B(m) = \frac{1}{1 + \frac{\Psi_0}{M_0} k_{back} F(m) \frac{z_0^2}{z_{coll}^2}}$$

where Ψ_0/M_0 is the absolute energy fluence on the central axis of a calibration beam at a distance z_o from the source per unit monitor chamber signal due to the forward directed fluence, derived from the absolute dose beam calibration process [Helax 2.2.4].

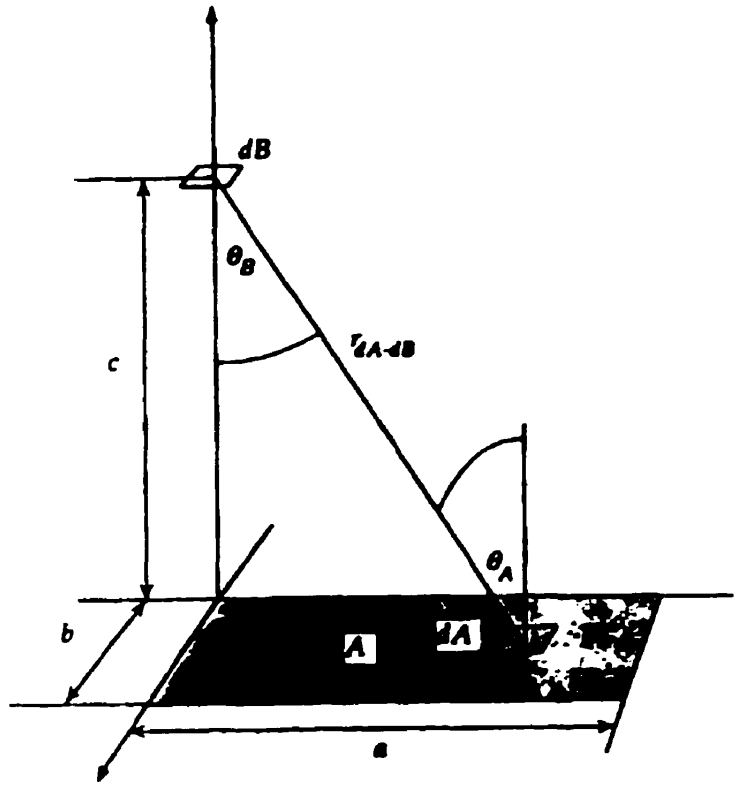

Figure 1-2 Geometry of view factor calculation with dB assumed as the monitor [Ahn 92b].

1.1.2.2 Modeling of the Head Scatter Fluence

The scatter fluence from various parts of the treatment head is calculated from the area of the scattering elements visible from the calculation point's eye view. This becomes a function of secondary collimator position for extended sources of scatter, which are located upstream from the remainder of the collimating system. The visible area of the scattering elements is determined by delineating polygons. The polygons are created by extending vectors, joining the calculation point in the patient and the edges of the collimators, MLC, and blocks, to the plane of the extended source, and connecting their points of intersection. The resultant polygon may represent either an open or blocked part of the beam.

1.1.2.2.1 Flattening Filter Effective Scatter

Since the entire primary energy fluence generated in the target passes through the flattening filter, it is one of the largest scatter sources in the beam. The filter is designed to produce a relatively uniform dose distribution at a depth in the patient in a plane perpendicular to the beam direction. For determination of the scatter fluence from this filter, a generic function is proposed [Ahn 94] which assumes the scatter fluence to be radially symmetric. The analytic expression describes the scatter released per filter area, or scatter distribution, as a linear function of the distance from the beam central axis, denoted in angular units by θ, as follows

$$1.13 \qquad \frac{d(\Psi_f/\Psi_o)}{dA} = \begin{cases} k_\sigma(\phi)k_C(\phi)\cdot\dfrac{3\tau(\theta_{prim}-\theta(1-\varepsilon))}{\pi\theta_{prim}^3(1+2\varepsilon)\cdot(r_{calc}-r_{filt})^2} & , \quad \theta \le \theta_{prim} \\ 0 & , \quad \theta \ge \theta_{prim} \end{cases}$$

where ε is the ratio of the scatter source distribution at the filter edge to that at the center, τ is the scatter emitted per solid angle integrated over the entire filter area, r_{calc} is the distance of the calculation point from the source, r_{filt} is the distance of the flattening filter from the source, and θ_{prim} is opening angle of the primary collimators, located upstream of the flatterning filter. The parameters, τ and ε, are fitted, along with k_{back}, to reconstruct measured output in air. This provides a scatter distribution representative of the scatter produced in the flattening filter as well as that produced by the primary collimators, hence there is no explicit modeling of the scatter from the primary collimators. k_σ is a correction factor that depends on the scattering angle φ, and describes the mean angular dependence of the cross section for the spectrum. k_c is also a correction factor, dependent

on ϕ, that compensates for the energy loss in the Compton process. Their values are a maximum of unity at ϕ=0°, decrease with increasing scattering angle, and decrease with increasing beam energy. In particular, k_σ = 0.4 and k_c = 0.7 for ϕ=15° in a 24 MV beam [Ahn 1994].

The total scatter reaching a calculation point is retrieved through integration of the distribution in equation 1.13 over the visible part of the filter and evaluation of the correction factors at an effective scattering angle, ϕ_{eff} [Ahn 94].

$$1.14 \qquad \frac{\Psi_f}{\Psi_0}(r) = k_\sigma(\phi_{eff}) \cdot k_C(\phi_{eff}) \cdot \frac{1}{(r_{calc} - r_{filt})^2} \iint_{\substack{visible \\ area}} \frac{3\tau(\theta_{prim} - \theta(1-\varepsilon))}{\pi\theta_{prim}^3(1+2\varepsilon)} dA$$

As previously noted the visible area of the flattening filter from the calculation points eye view is represented by a polygon. The polygon can be broken down further into numerous right angle triangles, which have a closed form solution of the integral [Ahn 94]. The scatter is then determined as the sum of integrals over each of the triangles.

Modulation of the Flattening Filter Effective Scatter

In the presence of an attenuator or dynamic collimation, the flattening filter scatter is affected. This is accounted for by introducing a mean modulation matrix as follows

$$1.15 \qquad \frac{\Psi_f}{\Psi_0}(r) = k_\sigma(\phi_{eff}) \cdot k_C(\phi_{eff}) \cdot \frac{1}{(r_{calc} - r_{filt})^2} \cdot \langle \eta \rangle \iint_{\substack{visible \\ area}} \frac{3\tau(\theta_{prim} - \theta(1-\varepsilon))}{\pi\theta_{prim}^3(1+2\varepsilon)} dA$$

where

1.16
$$\langle \eta(x,y) \rangle \approx \frac{\sum_k \frac{3\tau(\theta_{prim} - \theta_k(1-\varepsilon))}{\pi\theta_{prim}^3(1+2\varepsilon)} \eta(X_k, Y_k)}{\sum_k \frac{3\tau(\theta_{prim} - \theta_k(1-\varepsilon))}{\pi\theta_{prim}^3(1+2\varepsilon)}}.$$

θ_k is a set of grid points covering the visible area of the flattening filter. X_k and Y_k are the coordinates of the point of intersection of the vector, joining the scatter element at θ_k to the calculation point (x,y), with the plane of the modulator. Note that modulation of the flattening filter scatter due to transmission through blocks is neglected.

1.1.2.2.2 Collimator Scatter from Collimator Edges

Collimator scatter is a result of scattering of photons from the edge surfaces of beam collimating devices. Beam collimating devices comprise secondary collimators, MLC and blocks. Although blocks are considered here to be a collimating device, the scatter introduced in the interior of the blocks and the modulation of the beam due to the blocks are modeled in a different manner, to be discussed in section 1.1.2.3.

The model for collimator scatter in photon therapy beams presented here was developed by Ahnesjo [Ahn 95a]. Essentially, a scatter kernel is integrated around the collimating beam periphery. The scatter kernel describes the energy fluence distribution of scattered photons resulting from a narrow line beam striking a collimator block, per unit length of the collimator. The model begins by separating collimator scatter into two types: (1) front face scatter –describing scatter from photons entering tangentially through the side facing the field periphery; and (2) inner edge scatter - defined as scatter

from photons entering the collimator through the surface facing the source. Since the two types of scatter are found to be related, the total scatter is derived from the inner edge scatter. A kernel modeling the inner edge scatter fluence onto a reference plane (at the isocenter) for a standard geometry (SAD=100cm, and the source to collimator block edge = 30cm), parameterized as a function of beam energy, is implemented. The total scatter kernel, also parameterized as a function of energy, is then derived from the inner edge scatter kernel, and scaled from the standard geometry to the actual geometry [Ahn 95a]. Finally the total scatter fluence is obtained through integration over the collimator peripheries of all the collimating devices exposed to the beam and visible from the calculation point [Helax 4.8]. The uncertainty in these calculations is approximately ±15%, however, since the contribution to the total dose from the collimator scatter is only about 1%, this results in only 0.15% uncertainty in the total dose [Ahn 95a].

1.1.2.2.3 Modulator Scatter

Modulator scatter originates from wedges, compensators, and trays. The model developed here [Ahn 95b] uses the scattering theory in the forward direction for a monoenergetic beam, and then applies corrections for angular and spectral effects to approximate the distribution of scatter released per filter area. The fluence scattered per solid angle per area from a scattering element dA at (x',y',z_m) of a modulator is given by,

$$\frac{d\Psi_m(x,y,z)}{dA} \approx \Psi_0 f(x'',y'') S^2 N_A \frac{Z}{A} \rho r_0^2 k_\sigma k_C k_s k_b \frac{-\eta \ln \eta}{\bar{\mu}}. \qquad 1.17$$

where: $\Psi_o(x'',y'')$ is the primary fluence in the reference plane ($z''=0$) at the position of the scattering element projected to the reference plane; $(N_AZ/A)\ \rho r_o^2$ represents the total Klein-Nishina cross section for forward scatter, where N_AZ/A and ρ are the electron and

mass densities, and r_o is the classical electron radius. The factor S^2 is the combined inverse square law for both primary (source to scatterer) and scattered (scattering element to the calculation point) radiation (see Figure 1-3), defined as

1.18 $$S^2 = \frac{z_s^2}{R_s^2 (z_s - z_m)^2}; \qquad R_s^2 = (x - x')^2 + (y - y')^2 + (z - z_m)^2$$

where z_s is the distance of the source from the reference plane (isocenter), z_m is the distance of the scattering modulator from the reference plane (isocenter), and R_s is the scatterer (x',y',z_m) to calculation point (x,y,z) distance. The modulation of the scattered fluence due to the attenuator is represented by $-\eta \ln \eta / \bar{\mu}$, where $\eta = e^{-\mu t}$ and $\bar{\mu}$ is the attenuation coefficient for the modulator material averaged over the incident spectrum. The corrections, k_σ, k_C, k_s, and k_b are determined from analytic parameterizations as functions of nominal energy, scattering angle, atomic number, attenuator thickness, and density. Specifically, k_σ corrects for angular and energy variations in the Klein-Nishina scattering cross section, taking on a maximum value of unity in the forward direction and decreases with increasing angle and increasing energy. k_C corrects for photon energy loss during Compton scatter as a function of scattering angle θ by determining the relative mean energy of photons scattered through the Compton process in a given direction θ. The k_c values are a maximum of unity in the forward direction and decrease with increasing scattering angle and increasing energy. k_s corrects for the change in the attenuation coefficient of the scattered photons, with a value of unity in the forward direction and increases with increasing energy. k_b corrects for radiative loss of energy from the generation of secondary bremsstrahlung. The k_b values are all greater than unity and increase with increasing atomic number and increasing energy.

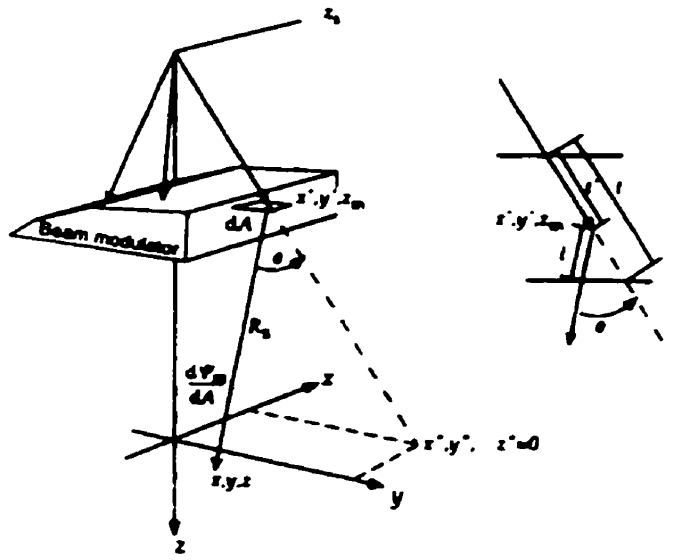

Figure 1-3: Geometry of modulator scatter. t' and l are the attenuation pathlengths of the primary and scattered photons, respectively.[Ahn 95b]

The total relative modulator scatter fluence would most obviously be determined through integration over the area of the filter irradiated by the beam and visible from the calculation points eye view. This integration procedure is, however, simplified by approximating it with a summation over pixels of a matrix, whose dimensions depends on the type of modulation [Helax pg. 50]. The summation is given by

$$1.19 \qquad \frac{\Psi_m(x,y,z)}{\Psi_0} = N_A \frac{Z}{A} r_0^2 \frac{k_b}{\overline{\mu}/\rho} \sum_i \eta_i^{above} f_i \eta_i^{below} S_i^2 \cdot k_\sigma(\phi_i) k_C(\phi_i) k_s(\phi_i) \langle -\eta \ln \eta \rangle_i \Delta A_i'$$

where ΔA_i is the area of pixel i, η_i^{above} and η_i^{below} account for modulation due to additional attenuators above and below the modulator under consideration and are evaluated at the centre of each pixel, similarly for the scattering angle ϕ_i. The brackets $\langle\rangle$ indicate an average of the bracketed term over the pixel.

1.1.2.3 Modulation by Blocks

Modulation of the primary beam and scatter introduced from the interior of the blocks are combined to produce an effective transmission coefficient. Modulation of the primary beam from blocks is modeled in a manner similar to that used for modulation of attenuators, section 1.1.2.1.1. The correction factors are neglected, resulting in a primary transmission coefficient as follows

1.20
$$\eta_{prim} = \frac{\int \Psi_E e^{-\mu(E)l} dE}{\int \Psi_E dE}.$$

The mean Z and Z/A for the block material are used to determine the appropriate monoenergetic attenuation coefficients obtained from standard tables. Specification of the block material and thickness is required by the Helax database prior to installation from which the user selects the block being used.

Scatter produced in the interior of blocks is calculated using the Modulator scatter Model, discussed in section 1.1.2.2.3, and neglecting the angular corrections, k_σ, k_C, and k_S, ie.,

1.21
$$\frac{\Psi_m}{\Psi_0} = N_A \frac{Z}{A} r_0^2 \frac{k_b}{\bar{\mu}/\rho} \sum_i \eta_i^{above} f_i \eta_i^{below} S_i^2 \cdot \langle -\eta \ln \eta \rangle_i \Delta A_i'$$

The scatter fluence calculated from this method is then summed with the primary transmitted fluence to give an effective transmission coefficient, ie.

1.22
$$\eta_{eff} = \eta_{prim} + \frac{\Psi_m}{\Psi_0}.$$

1.1.3 Determination of Lateral Primary Energy Fluence Distribution

The relative lateral primary energy fluence distribution, f(x,y) is required for determination of the dose and is calculated by a method proposed by Ahnesjo and Trepp [AT 91]. A Cartesian dose matrix is obtained via interpolation from a set of star profile measurements taken at a depth in water (10cm) for the maximum field size [Helax]. A corresponding lateral pencil kernel matrix is determined from a pencil kernel distribution, describing the energy deposited from a point monodirectional beam in a semi-infinite medium, derived from Monte Carlo calculated monoenergetic pencil kernels and the effective energy spectrum, and the spectrum is assumed to be laterally invariant. The energy fluence matrix, $\tilde{f}(x,y)$, is then obtained by deconvolving the dose matrix by the kernel matrix. The resulting fluence distribution is filtered to remove the head scatter fluence and renormalized on the central axis, yielding a relative primary lateral fluence distribution, ie.,

1.23
$$f(x,y) = \frac{\tilde{f}(x,y) - \Psi_{cont}^{max\ field}(x,y)/\Psi_0}{1 + \Psi_{cont}^{max\ field}(0,0)/\Psi_0}.$$

1.1.4 Dose Calculation Algorithm

The dose per incident energy fluence is calculated in Helax through convolution of energy deposition kernels with an energy fluence distribution. Determination of the energy fluence distribution was described in the previous section. The following

discussion describes the energy deposition kernels and the convolution techniques implemented in TMS for determination of the dose.

1.1.4.1 Energy Deposition Kernels

The type of energy deposition kernels implemented here are pencil beam kernels which describe the energy deposited per unit mass per unit incident fluence in a semi-infinite medium from a point monodirectional beam [Helax]. Convolution of these pencil beam kernels with the energy fluence distribution yields the dose per incident energy fluence. The convolution technique implemented is based on triangulation of the field. The dose is given by the sum of the dose over each triangle, determined by the product of the mean fluence for the triangle and integration of the pencil beam kernel over the triangle area.

1.1.4.1.1 Primary and Phantom Scatter Kernels

Primary dose is defined as the energy deposited by charged particles generated in primary photon interactions. Scattered dose, is the dose resulting from charged particles generated in secondary photon interactions or from bremsstrahlung and/or annihilation photons created in the medium. The pencil beam kernel, describing the energy deposition from primary and scatter dose due to a clinical beam, requires a poly-energetic representation. This is achieved through superposition of Monte Carlo derived monoenergetic pencil kernels and an effective energy spectrum. The effective spectrum is determined by fitting measured depth doses for several square field sizes to the depth doses calculated using Monte Carlo generated point spread functions [Ahn 92a]. Poly-

energetic pencil beam kernels, defined for each depth in the medium, are described analytically by the sum of two exponentials, ie.,

1.24 $$\frac{p}{\rho}(r,z) = \frac{A_z e^{-a_z r}}{r} + \frac{B_z e^{-b_z r}}{r}$$

where r is the radial distance from the pencil beam axis, and the parameters A_z, a_z, B_z, and b_z are depth dependent fitting parameters. These parameters are determined by performing a least squares fit of the radial integral of the analytic kernel with radially cumulative distributions of the Monte Carlo generated polyenergetic kernels [Ahn 92a].

In the above expression, the first exponential can be assumed to result from primary dose and the second from scatter dose, ie. $a_z > b_z$. To make this differentiation more accurate a correction factor C_z is introduced and resolved by fitting the radial integral of the primary kernel (equivalent to the primary dose per incident energy fluence), to the primary dose per incident energy fluence as determined by the independently calculated Monte Carlo data, ie.,

1.25 $$d_p^{MC}(z) = \frac{D_p^{MC}(z)}{\Psi} = C_z 2\pi \frac{A_z}{a_z}.$$

The phantom scatter dose is then given by

1.26 $$d_s(z) = \frac{D_s(z)}{\Psi} = 2\pi \int_0^{\text{Field radius}} \frac{B_z e^{-b_z r}}{r} r dr + (1 - C_z) 2\pi \frac{A_z}{a_z}.$$

At the geometric edge of the field, the dose in the patient does not fall off instantly because of: (1) the geometric penumbra due to the finite size of the source and beam collimation; (2) scattered photon dose; and (3) lateral transport of charged particles. Helax system starts by ignoring the penumbra broadening due to phantom scatter. The

lateral transport of charged particles is given by the lateral spread of the primary pencil beam kernel. Therefore, the primary pencil beam kernel in the penumbra region is calculated by convolving the primary exponential term with a Guassian, width σ_z, describing the source distribution projected to the depth of calculation., ie.,

1.27 $$\frac{p_p}{\rho}(r,z) = C_z\left[\frac{1}{\pi\sigma_z^2}e^{-r^2/\sigma_z^2} \otimes \frac{A_z e^{-a_z r}}{r}\right].$$

The primary pencil kernel was approximated by carrying out numerical convolutions over the relevant parameter ranges, and fitting them to a linear superposition of a Guassian, and an exponential. The accuracy of this approximation was tested, and the deviation between measured and fitted penumbra was found to be generally less than 1mm, with a maximum deviation of 1.3 mm [Ahn 92a].

Finally one last fitting is performed to further optimize the fit of the measured depth dose curves. Parameters, A_z and B_z are replaced by $a_{corr,z}A_z$ and $b_{corr,z}B_z$, respectively and the new correction factors are derived by optimizing the fit of reconstructed depth dose curves to measured depth dose curves.

1.1.4.1.2 Charged Particle Contamination Kernel

Charged particle contamination refers to the presence of charged particles in the build-up region, produced by primary photon interactions in the air, filters, and block trays. The pencil beam kernel for charged particles, modeling the energy deposition per unit incident primary photon energy, is assumed to be a product of a Guassian and an exponential

1.28 $$\frac{P_{c_z}}{\rho}(r,z) = \alpha e^{-\beta z} e^{-\gamma r^2}.$$

The Guassian, representing the contaminant dose in the patient, has a depth independent radius, as proposed by Nilsson [Nil 85]. The exponential models the broad beam depth dose behavior of the contaminant charged particles, as demonstrated by Mackie and Scrimger [MS 82] and Beauvais et al [BBD 93]. The contamination is estimated by taking the difference between measured and calculated (primary plus scatter) depth dose distributions in the build-up region. The parameters α, β, and γ (depth independent), are then derived by fitting the depth dose distributions resulting from the above pencil beam kernel to the contamination dose, calculated at depth z on the beam axis for a square field size f, by integrating the pencil kernel defined in equation (1.28) as follows [Ahn 92a]

1.29 $$\frac{D_{c_z}(z,f)}{\Psi} = \alpha e^{-\beta z} \int_{-f/2}^{f/2}\int_{-f/2}^{f/2} e^{-\gamma(x^2+y^2)}dxdy,$$

yielding the contaminant dose per incident primary photon energy fluence. The integral is evaluated with the use of an error function, ie.,

1.30 $$\frac{D_{c_z}}{\Psi} = \alpha e^{-\beta z}\frac{\pi}{\gamma} erf^2\left(\sqrt{\gamma}\frac{f}{2}\right), \text{ where } erf(x) = \frac{2}{\sqrt{\pi}}\int_0^x e^{-t^2}dt.$$

Since the contamination dose varies depending on the accessories inserted in the beam, different sets of parameters are determined for open and wedged beams.

1.1.4.1.3 Photon Contamination Kernels

The dose from head scatter photons has two constituents: (1) primary head scatter dose; and (2) phantom head scatter dose. The primary pencil beam kernel described

previously in section 1.1.4.1.1, assuming lateral electron equilibrium, is used as the primary photon contamination kernel, ie.,

1.31 $$\frac{p_p^{hvcont}}{\rho}(r) = C_z a_{corr,z} \frac{A_z e^{-a_z r}}{r}.$$

The primary head scatter dose is estimated from the relative head scatter fluence $(\Psi_f+\Psi_c+\Psi_m)/\Psi_0$ converted to dose by means of the radial integral of the primary kernel using the approximation of lateral charged particle equilibrium, ie.,

1.32 $$d_p^{hvcont}(r) = C_z a_{corr,z} 2\pi \frac{A_z}{a_z}\left(\frac{\Psi_f + \Psi_c + \Psi_m}{\Psi_0}\right).$$

The dose contribution from the phantom head scatter photons are approximated by assuming its dose per fluence behavior to be identical to that of the phantom scattered primary photons, ie. [Helax],

1.33 $$d_s^{hvcont}(r) = \frac{d_s(r)}{f(x,y)\eta(x,y)}\left(\frac{\Psi_f + \Psi_c + \Psi_m}{\Psi_0}\right)$$

where $d_s(r)$ is the phantom scatter dose, $D_s(x,y,z)$, per primary energy fluence, Ψ_o.

1.1.4.2 Convolution Techniques

In the section describing the modeling of the head scatter (1.1.2.2), delineation of the field shape into polygons was described. These polygons are modified by removing possible parts of the field located outside the patient, cutting off intersecting parts of block polygons etc. [Helax]. The convolution techniques implemented here are based on the method of triangulation, decomposing the polygon into a set of triangles [Ahn 92a]. The convolution is then carried out by replacing the integral over the polygon as a sum of

integrals over triangles. Figure 1-4 demonstrates how the field shape given by a polygon can be decomposed into a set of triangles. A triangle is formed from each segment of the polygon by connecting the vertices of the segment to the calculation point. The dose per incident primary energy fluence at depth z in a homogeneous half slab from a non-divergent beam with mean uniform energy fluence $\langle \Psi_i \rangle$ over each triangular section i, is given by

1.34 $$d(x,y,z) = \frac{D(x,y,z)}{\Psi_0} = \sum_i \left\langle \frac{\Psi_i}{\Psi_0} \right\rangle \kappa_i \int_{\theta_1}^{\theta_2} \int_0^{(L_i / \cos\theta)} \frac{p}{\rho}(r,z) \cdot r dr d\theta$$

where p/ρ is the analytic pencil beam kernel (primary or scatter) at depth z, and κ_i is ± 1, depending on the sign of the cross product of the vectors from the calculation point to the triangle vertices. θ_1 and θ_2 are the angles between the vector (L_i), stemming from the calculation point and normal to the polygon segment, and sides of the triangle. L_i is the length of the vector decomposing triangle i into two right angle triangles (Figure 1-4).

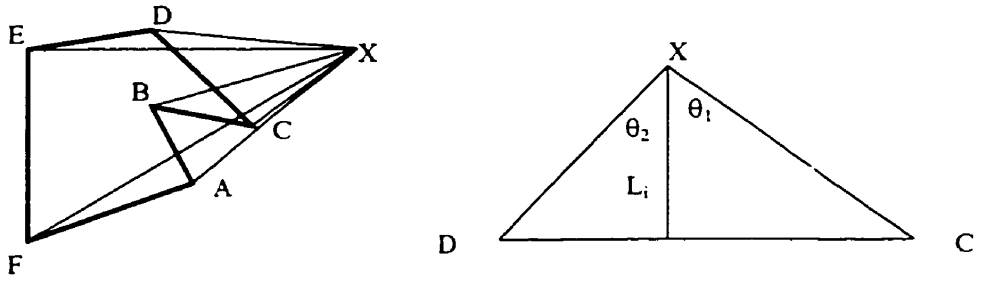

Figure 1-4 A polygon ABCDEF, representing a field shape, is decomposed into triangles XAB, XBC, etc [Ahn 92a]. Shown to the right is the decomposition of each triangle into two right angle triangles, where θ_1 and θ_2 are the angles at the calculation point between the normal (L_i) and the directions to the endpoints of the segment [Helax].

A mean relative energy fluence is used in equation (1.34) to correct for fluence variations. For primary dose calculations the mean energy fluence calculated is the same for all triangles. Specifically, for primary dose, d_p, calculations of open beams, the relative energy fluence at the calculation point is used since the lateral range of charged particles is short. For primary dose calculations of modulated beams, fluence gradients exist, and a weighted mean over a circular region around the calculation point is implemented, ie.,

1.35
$$\left\langle \frac{\Psi_i}{\Psi_0} \right\rangle_p^{\text{mod}} = \frac{\sum_j \frac{\Psi(x_j, y_j)}{\Psi_0} \cdot k_{PQ} \cdot w_j}{\sum_j w_j}$$

where k_{PQ} is a beam hardening correction factor for the primary dose due to changes in spectrum and energy absorption coefficients with beam penetration in a modulator. The sampling region radius is determined by a combination of the beam source size, projected to the calculation point and the kernel width. The sampling region is decomposed into segments, j, of circular rings, around the calculation point, where (x_j,y_j) represents the center of each segment j. The weight is proportional to the integral of the primary pencil beam kernel over segment j [Helax].

The mean relative energy fluence is calculated differently then above for phantom scatter dose, d_s, as the lateral gradient of the energy fluence is more significant. Specifically, variations in the energy fluence are accounted for by calculating a weighted average of the relative energy fluence in each triangle,

1.36
$$\left\langle \frac{\Psi_i}{\Psi_0} \right\rangle_s = \frac{\sum_j \frac{\Psi(x_{ij}, y_{ij})}{\Psi_0} \cdot k_{SQ} \cdot e^{-b_2 r_{ij}}}{\sum_j e^{-b_2 r_{ij}}}$$

where the weights are the pencil kernel values, r_{ij} is the distance of the sampling point j in triangle i to the calculation point, and (x_{ij}, y_{ij}) are the coordinates of the sampling point j in triangle i. The sampling resolution is varied depending on the energy fluence gradient. k_{SQ} is a beam hardening correction factor for the patient scatter dose due to changes in spectrum and energy absorption coefficients with beam penetration in a modulator. It is determined by the ratio of phantom scatter dose at a given depth, d, in the patient for a modulated field of filter thickness ,t, versus an open field. Full details of this expression are provided in Ahnesjo *et al* [Ahn 95b]. In the above expressions

1.37
$$\frac{\Psi(x,y)}{\Psi_0} = \begin{cases} \eta(x,y)\cdot f(x,y)\cdot \dfrac{r_{ref}^2}{r_{calc}^2}, & primary \\ \dfrac{r_{ref}^2}{r_{calc}^2}\cdot\left(\dfrac{\Psi_f + \Psi_m + \Psi_C}{\Psi_0}\right), & headscatter \end{cases}.$$

1.1.4.3 Dose per Incident Energy Fluence

The total dose per incident primary energy fluence is given by

1.38
$$d(x,y,z) = d_p(x,y,z) + d_s(x,y,z) + d_s^{hvcont}(x,y,z) + d_p^{hvcont}(x,y,z) + d_{C_\pm}(z,f)$$

where $d_p(r)$ is the primary dose per primary energy fluence, d_s is the phantom scatter dose per primary energy fluence, $d_{C\pm}$ is the charge particle contamination dose, d_s^{hvcont} is the dose per incident primary energy fluence from the phantom scattered head scatter, and d_p^{hvcont} is the dose per incident primary energy fluence from the primary head scatter. All doses displayed in TMS are relative doses. The type of relative normalization dose implemented in this study was dose plan normalization, where the relative dose Level L displayed for a single beam is given by

1.39 $$L(r) = \frac{L_{norm}}{d_{norm}} d(r)$$

where L_{norm} is a normalization level (set to 100 in this study), d(r) is the total dose per primary energy fluence, given in equation 1.38, and d_{norm} is the dose per primary energy fluence at the point of normalization. The relative dose L(r) is the level displayed in the isodoses generated by the *display doses* tool in the *beam modeling* work module.

For a comparison between measurements and calculations, output factors and head scatter factors were measured and calculated. The output factor normalized dose is calculated in TMS as the ratio of the dose per monitor unit for the treatment beam, i, to that for the calibration beam

1.40 $$d_i^{OFN}(r) = \frac{(D(r)/M)_i}{(D/M)_i^{calib}}$$

where the dose per monitor unit for the treatment beam is given by

1.41 $$(D(r)/M)_i = \frac{\Psi_0}{M_0} \frac{1}{1+b_i} d_i(r)$$

where (Ψ_o/M_o) is a constant for a given beam quality as discussed in section 1.1.2.1.2, and b_i is the backscatter fraction, describing the monitor unit perturbation due to the fluence of particles scattered back into the monitor, ie. $b=M_b/M_o$, where M_b and M_o are discussed in section 1.1.2.1.2. The dose per monitor unit for the calibration beam is also given by the above expression where, b_i and $d_i(r)$ are for the calibration beam. The calibration geometry is a 10cm x 10cm field with isocenter placed at a depth of dmax in water.

Head scatter factors are calculated in the dose plan protocol as the ratio of the total energy fluence per monitor unit for a test field at a test point, to that for the calibration beam at the isocenter, ie.,

1.42 $$OF_{headscatter.TMS} = \frac{(\Psi(r_{test})/M)^{test}}{(\Psi_0/M)^{calib}} = \frac{\eta(r_{test})\cdot f(r_{test}) + \Psi_{cont}^{test}(r_{test})/\Psi_0}{1+\Psi_{cont}^{calib}/\Psi_0}\cdot\frac{1+b^{calib}}{b^{test}}.$$

The monitor units output in the dose plan protocol (later used to calculate output factors where the line dose option fails to properly normalize) for a single beam plan are calculated according to

1.43 $$M_i = \frac{D_{presc}}{L_{presc}}\cdot\frac{L_{norm}}{d'_{norm}}\cdot\frac{1+b_i}{1+b_i^{calib}}\cdot\frac{d_i'^{calib}}{(D/M)_{meas}^{calib}},$$

where $d_i'^{calib}$ is the calibration beam normalized dose, ie., $d_i'^{calib} = \frac{d_i^{calib}}{d_i^{std}}$, and similarly $d'_{norm} = \frac{d_i^{norm}}{d_i^{std}}$. d_i^{std} is a standard dose calculated for the beam quality in beam i, for a standard geometry (10cm x10cm, dmax, SSD=100cm). The prescription dose, D_{presc}, is the dose prescribed to a percent isodose line, L_{presc}. This is assumed to be 100 cGy prescribed to the normalization point, where the prescription level, L_{presc}, is equal to L_{norm} (ie. usually 100), unless otherwise specified.

1.2 Dose Calculations in CMS

In this thesis, the Clarkson algorithm of CMS Focus version 2.4.0 treatment planning system is evaluated. The FFT convolution and the multi-grid superposition algorithms were not evaluated since these algorithms have not been clinically implemented yet. In the Clarkson implementation, the treatment head is characterized by a single parameter ie. output factor (OF) for a given collimator setting, which is interpolated between the OF measured for several square field sizes. Therefore, unlike TMS, a separate head scatter model is not considered. Clarkson's method of sector integration is based on derivation of scatter phantom ratios (SPR) from a set of percentage depth doses (PDDs) measured for several square field sizes. The basis of this method is the separation of the absorbed dose in a patient into two components, namely: (1) the primary component, which is independent of the field size and shape; and (2) the scatter component, which is dependent on the field size and shape. The primary component of a beam is characterized by a flattening filter function and then modified by the attenuation through the beam modifying devices and the patient. To determine the scattered dose, the field is divided into sectors and the scatter contribution from each sector is summed by considering the sector to be part of its own circle, for which the scatter phantom ratio (SPR) is already known. This process yields an average SPR for the irregular field at the calculation point [Khan 94].

The algorithm takes into account primary dose corrections for transmission by wedges, and blocks, however, scatter modifications due to variations in field intensity, such as for wedges are not explicitly considered.

1.2.1 Clarkson Algorithm

In this section, a brief review of dose calculations using Clarkson's integration using TPRs and SPRs is provided. The system calculates a relative dose distribution for each beam with respect to the user defined weight point, at a number of points of intersection between fan line and depth line grids, see Figure 1-5. A connection to the absolute dose is then established by normalizing the sum of weighted relative dose distributions for several beams in a treatment plan.

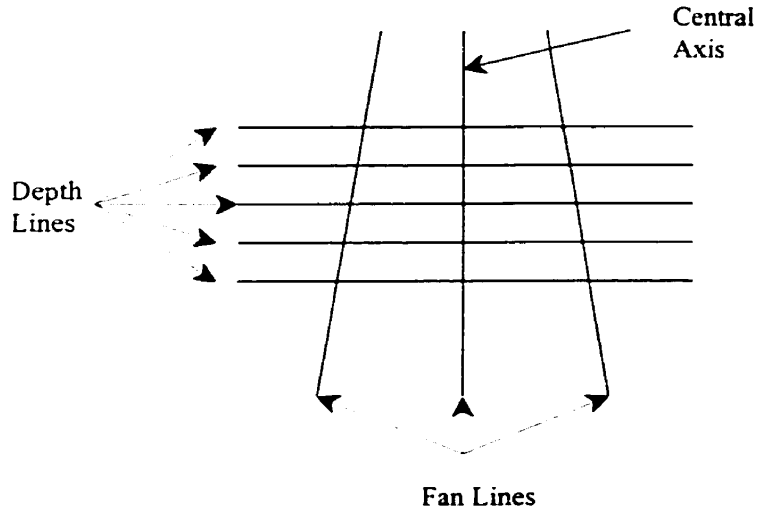

Figure 1-5: Fan line and depth line grids. The relative dose is calculated at each intersection point and a patient dose matrix, defined by the user, is determined via interpolation of the relative doses at these intersection points.

1.2.1.1 Dose per monitor unit

The basic equation to calculate dose per monitor unit (MU) at each point along the fan lines for a given beam, is determined by [CMS Appendix A]

$$\frac{D(d,l;fd,fco,ba;r,th,s)}{MU} = \left[\frac{\frac{Dc(dc;ec;0;sc)}{MU}}{TPR(dc;ec;0)}\right] \cdot \left[\frac{Sp(0)}{Sp(ec)}\right]$$

1.44
$$\left(\frac{sc}{s}\right)^2 \cdot WEGFAC(;;r,th) \cdot \{INT(l;;r) \cdot TRAY \cdot [TPR(l;0;0) \cdot PT(;fd,fco,ba;r,th,s) + SPR(l;fd,fco,ba;r,th)]\}$$

where

$$\frac{D(d,l;fd,fco,ba;r,th,s)}{MU}$$

is the dose per monitor units for an arbitrary point P, illustrated in Figure 1-6. The point of dose calculation is at a physical depth (projected to the central axis), d, and radiological depth, *l*, located at a transverse distance r from the central axis. The angle between the vector r and the collimator axis along the beam width is denoted by th, and s is the axial distance along the central axis from the radiation source. The field size is defined by: the collimator setting, fd, with a field center off-set from the central axis denoted by fco; and a customized port or MLC denoted by the blocking arrangement, ba.

Various parameters on the right hand side of equation 1.44 are described in detail in the following pages.

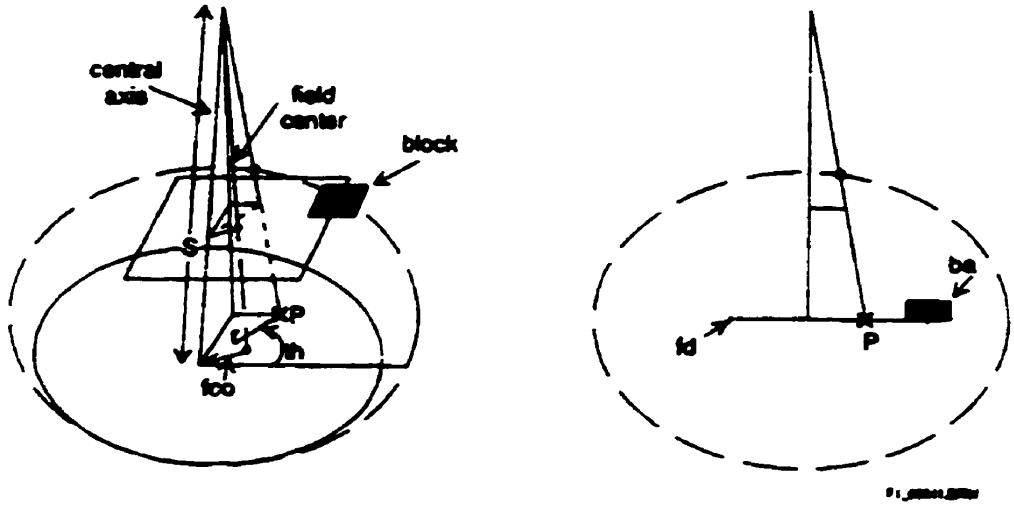

Figure 1-6 Geometry of the point of dose calculation D(d,l;fd,fco,ba;r,th,) where, parameters fd, fco, and ba are determined at depth d.[CMS]

$$\frac{Dc(dc;ec;0,sc)}{MU}$$

is the calibration dose output, defined as the dose per monitor unit, with the tray removed, at the calibration depth, dc, axial calibration distance on the central axis, sc {usually the source to axis distance (SAD)}, and for the open field equivalent square, ec. At CancerCare Manitoba (CCMB) sc is set to the nominal SAD of 100cm for linacs and 80 cm for Cobalt units. All our beams are calibrated at a depth of maximum dose, ie. dmax, and source to calibration point distance of SAD. The field size ec is defined at SAD. This factor is the same as the commonly known output factor.

TPR (dc;ec;0)

is the central axis tissue phantom ratio (TPR) for the open field equivalent square, ec, at the calibration depth, dc. At CCMB, TPRs are normalized to a depth of dmax for each field size. Therefore (TPR(dc;ec;0) is set to unity for each ec.

$$\left[\frac{Sp(0)}{Sp(ec)}\right]$$

is the ratio of phantom scatter factors, defined at the reference depth where the TPRs are normalized, for a zero field size to that for the open equivalent square field. The function $TPR(dc;ec;0)\cdot\frac{SP(ec)}{SP(0)}$ can be shown to be the same as peak scatter factor PSF(ec) [Khan]. Therefore,

1.45 $$\frac{D(dc;ec;0,sc)}{MU}\cdot\frac{1}{TPR(dc;ec;0)}\cdot\frac{SP(0)}{SP(ec)}$$

is the dose per MU measured in air for a collimator setting ec at a distance SAD from the source. Also,

1.46 $$\frac{D(dc;ec;0,sc)}{MU}\cdot\frac{1}{TPR(dc;ec;0)}\cdot\frac{SP(0)}{SP(ec)}\cdot\left(\frac{sc}{s}\right)^2$$

is the dose per MU, measured in air for the same collimator setting at a distance s from the source at the central axis of the beam.

$$\left(\frac{sc}{s}\right)^2$$

is the inverse square law correction, taking the dose from the calibration distance, sc, to the axial distance of the point of calculation, s.

TPR(*l*;0;0)

is the central axis TPR at the radiological depth, extrapolated to zero field size. For the case when TPRs are referenced to dmax, it can be shown [Khan] that TPR(*l*;0;0) is the same as TAR(*l*;0;0).

PT(;fd,fco,ba;r,th,s)

accounts for primary dose corrections due to transmission and penumbra effects arising from secondary collimators, and customized ports.

SPR(*l*;fd,fco,ba;r,th)

is the scatter phantom ratio at the radiological depth, *l*, for the blocking arrangement, ba, at the dose point located at (r,th,s). The SPR is calculated using Clarkson's integral. For the case when TPRs are referenced to dmax, SPR can be shown to be the same as scatter air ratio (SAR). Therefore, the function [TPR(*l*;0;0)•PT(;fd,fco,ba;r,th,s) + SPR(*l*;fd,fco,ba;r,th)] is the effective tissue air ratio (TAR) at radiological depth *l*, for the blocking arrangement ba, at the dose point located at (r,th,s). It is now clear that multiplying in air dose at the calculation point, ie. equation 1.46, by the effective TAR, the term [] above, yields in phantom dose. The remaining factors such as TRAY, WEGFAC, INT(*l*,r) are then applied to in-phantom dose.

INT(*l*;;r)

is a radially symmetric function which accounts for radial variations in beam intensity due to the flattening filter. It is estimated from measured diagonal beam profiles at a number of depths by removing the effect of secondary collimators and in-phantom scatter. This function defines, the radial variations of primary

dose in water due to the flattening filter and hence depends upon the radiological depth *l*.

WEGFAC(;;r,th)

is the transmission through the wedge along the appropriate fanline and includes changes to both primary and scatter dose due to the wedges. The evaluation of this transmission is discussed in section 1.2.1.1.1.

TRAY

is the transmission factor for tray(s) used for holding blocks and compensators. This factor is measured in-phantom and hence accounts for primary plus the scatter changes due to the tray.

Equation 1.44 is rearranged to a value proportional to the dose, and is evaluated at each fanline/depthline intersection point from the right hand side of the following equation

$$D_{pt} \propto \frac{\frac{D(d,l;fd,fco,ba;r,th,s)}{MU}}{\frac{Dc(dc;ec;0,sc)}{MU}} * \frac{TPR(dc;ec;0) * \left[\frac{Sp(ec)}{Sp(0)}\right]}{(TRAY * sc^2)} =$$

$$\left(\frac{1}{s}\right)^2 \cdot WEGFAC(;;r,th) \cdot \{INT(l;;r) \cdot [TPR(l;0;0) \cdot PT(;fd,fco,ba;r,th,s) + SPR(l;fd,fco,ba;r,th)]\} \quad 1.47$$

where the term in the brackets {} is referred to as the tissue ratio{TXR}. Calculation of the individual terms in TXR, and WEGFAC will de discussed in the following sections.

1.2.1.1.1 WEGFAC

Wedge transmission values, calculated for each fan ray, depend on the distance, t, the ray travels through the wedge, and the linear attenuation coefficient, μ, specific for the wedge material and beam energy, as follows

$$WEGFAC(r,th) = e^{-\mu t(r,th)} \cdot \frac{WF}{e^{-\mu T}}$$

where T is the thickness of the wedge on the central axis and WF is the wedge transmission on the central axis. WF is determined via linear interpolation for the field size determined by blocking arrangement ba or fd for unblocked fields from a table of stored values for square field sizes. CMS focus version 2.4.0 dose not support wedges of arbitrary wedge angle as realized by the virtual wedge software of Siemens KD2 linac. A set of four, ie. 15°, 30°, 45°, and 60°, wedges at each energy have been mimicked by physical wedge modeling by using measured isodose distributions for virtual wedges.

1.2.1.1.2 TXR

TPR for Zero Field Size

See section 1.2.1.1.

Primary Correction Due to Penumbra PT(;fd,fco,ba;r,th,s)

Customized ports, having diverging edges parallel to the fanlines, are entered as a set of contour points and presented as polygons, representing either a cutout (where the radiation is blocked outside of the polygon) or a block (where the radiation is blocked inside of the polygon). The fraction of radiation passing through each blocked area is described by a transmission value, assigned to each polygon. These transmission values

are used in the primary correction to account for the modulation of the primary dose. MLCs are defined only as cutouts, however, they have not been commissioned in the CMS version implemented at CancerCare Manitoba. Since CMS focus dose not have an explicit head scatter model, the dose calculation for MLCs are expected to be the same as for blocks. The correction can be separated into the individual contributing components as follows,

$$PT(;fd,fco,ba;r,th,s) = PT(;fu,fco,0;r,th,s)\cdot PT(;fl,fco,0;r,th,s)\cdot [PT(;0,0,cutout;r,th,s) - PT(;0,0,blocks;r,th,s)] \quad (1.48)$$

where

PT(;fu,fco,0;r,th,s) is the penumbra for the upper collimators,

PT(;fl,fco,0;r,th,s) is the penumbra for the lower collimators,

PT(;0,0,cutout;r,th,s) is the penumbra for the cutout, and

PT(;0,0,blocks;r,th,s) is the penumbra for the custom blocks.

Collimator Penumbra

The collimator penumbra is estimated by the following relation [CMS]

$$PT(;fx,fco,0;r,th,s) = Tx + (1-Tx)\cdot Fx \quad (1.49)$$

where x is substituted with u for upper or l for lower collimators. Tx is the transmission through the collimator (same for both), and Fx is the fraction of radiation at the dose point, from the extended source unobscured by the field defining collimator jaws (assuming the other jaws set to infinity). Fx is determined from the double integral of the radiation source strength distribution. Assuming, the source strength to be normally distributed with the radial distance from the center of the source [CMS], Fx, reduces to

$$Fx = \begin{cases} 0.5 \cdot \{erf[Bc \cdot (x_0 + \left(\frac{W}{2}\right) - x)] - erf[Bc \cdot (x_0 - \frac{W}{2} - x)], & x = u \\ 0.5 \cdot \{erf[Bc \cdot (y_0 + \left(\frac{L}{2}\right) - y)] - erf[Bc \cdot (y_0 - \frac{L}{2} - y)]\}, & y = l \end{cases} \quad 1.50$$

where erf is the error function, given in equation 1.30, W and L are the beam width and length, respectively, (x_o,y_o) are the field center coordinates at the depth of the calculation point, (x,y) are the calculation point coordinates with respect to the central axis, and Bc is a function parameterizing the size of the penumbra, ie.,

$$Bc = 2 \cdot AL_c \cdot \frac{scd}{sd \cdot (s - scd)} \quad 1.51$$

where AL_c is a source size scaling parameter for the collimator, scd is the source to collimator distance, sd is the source diameter, and s is the source to calculation point distance, projected to the central axis [CMS].

Cutout and Block Penumbra

The cutout and block penumbra are given by expressions similar to that determined for the collimator penumbra, ie.,

$$PT(;0,0,cutout;r,th,s) = Tp + (1 - Tp) \cdot Fp \quad 1.52$$

$$PT(;0,0,blocks;r,th,s) = \sum_k (1 - Tb_k) \cdot Fb_k \quad 1.53$$

where Tp is the transmission through the blocked portion of the field for cutout, and Tb_k is the transmission of the kth block. The penumbra functions, Fp and Fb, are evaluated by sector summations. The polygon is divided into triangles (sectors) by connecting the calculation point to two neighboring contour points in the polygon. The angle subtended

by the line segments joining the calculation point to the contour points is denoted by θ_n. If θ_n is greater than 10°, the sector is divided into smaller subsectors of angle $\Delta\theta_m$, where m denotes the side of the polygon side [CMS]. The penumbra functions, Fp and Fb, are given by the same equations, ie., suppressing the p and b,

1.54
$$F = \sum_{m=1}^{sides} \frac{\Delta\theta_m}{2\pi} \sum_{n=1}^{sectors} [1 - e^{-(B_{cp} \cdot R_n)^2}]$$

where $\Delta\theta_m$ is the sector angle for the mth side of the cutout/block, R_n is the radius of the nth sector on the mth side of the cutout [CMS], and Bcp parameterizes the size of the penumbra according to equation 1.51 where scd becomes, std, the source to tray distance. See Figure 1-7.

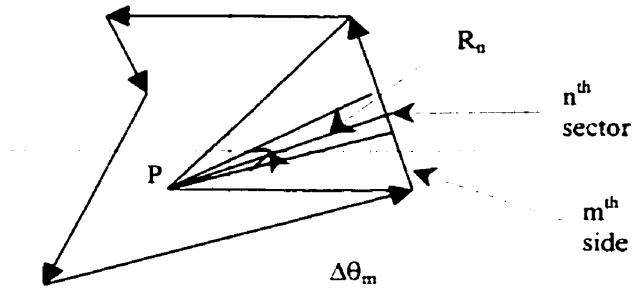

Figure 1-7 Sectorization of Cutouts and Customized Ports. The polygon represents an irregular-shaped field projected to the depth of calculation point P. The cross hairs represent the beam axis, and there intersection point is the position of the central axis of the beam.

SPR Integral

Phantom scatter is the scattered radiation produced in phantom, and can be calculated as the scatter produced by the field defined by the collimator (SPR(l;fd,fco,0;r,th) and cutouts (l;0,fco,cutout;r,th), minus the scatter reduced by blocks (SPR(l;0,fco,$blocks_k$;r,th), ie.,

$$SPR(l;fd,fco,ba;r,th) = Tp \cdot SPR(l;fd,fco,0;r,th) + (1-Tp) \cdot SPR(l;0,fco,cutout;r,th) - \sum_{k=1}^{blocks}(1-Tb_k) \cdot SPR(l;0,fco,blocks_k;r,th) \quad 1.55$$

where the term $Tp \cdot SPR(l;fd,fco,0;r,th)$ is the phantom scatter ratio for an open field, size fd, modified by the transmission through the collimators, ie. assumes the field is completely blocked by a cutout, $(1-Tp) \cdot SPR(l;0,fco,cutout;r,th)$ is the phantom scatter ratio for the field defined by the cutout minus the transmitted phantom scatter already accounted for in the first term, and the last term on the right hand side of equation 1.55 is the phantom scatter ratio for the blocked field minus the transmission of this scatter through the blocks. For an irregularly shaped field, the scatter at a point is determined by sectorization of the polygon (see Figure 1-7), as for the penumbra calculations, and integration of the scatter reaching the point over each of the sectors, ie.,

$$SPR(l;0,fco,polygon;r,th) = \sum_{m=1}^{sides} \frac{\Delta\theta_m}{2\pi} \sum_{n=1}^{sectors} SPR(1;Rn;0) \quad 1.56$$

where $SPR(l;R_n;0)$ is the scatter phantom ratio on the central axis for a field of radius R_n at depth l, given by,

$$SPR(l;R_n;0) = TPR(l;e_n;0) \cdot \frac{Sp(e_n)}{Sp(0)} - TPR(l;0;0) \quad 1.57$$

where $TPR(l;e_n;0)$ is the TPR for an equivalent square of side $e_n = (1.782+0.00184R_n)*R_n$. Note if R_n extends beyond the collimators it is clipped to the collimator edge. Also note that if R_n extends beyond the patient skin and is still within the collimator, it is not modified.

The following assumptions are made in this scatter calculation:

(1) the primary beam is laterally invariant, ie. the scatter component only depends on the distance between the calculation point and the field edge;

(2) a homogeneous scattering medium exists over the region defined by the field, resulting in an overestimation of scatter near the field edges.

Flattening Filter Correction INT(l;;r)

This function accounts for variations in primary beam dose in water as caused by the flattening filter. Specifically, the intensity function INT(l;;r) is the relative beam intensity along the beam fanlines, excluding the effects of the collimators and phantom scatter. The basis of the calculation is a set of diagonal off center ratios (OCD) measured, at the machine reference distance (SAD), and stored in the source file maintenance. The intensity function is assumed to be radially symmetric and is calculated at the radial distance r of the calculation point from the central axis, scaled to the radiological depth below the OCD measurement surface (see Figure 1-8), ie., [CMS Appendix B]

$$1.58 \qquad INT(l;;r) = \frac{TPR(l;emx_{p\cdot};0)\cdot OCD(l;emx_{p\cdot};r',45,SSD_{OCD})\cdot \dfrac{S_p(emx_{p\cdot})}{S_p(0)}}{TPR(l;0;0)\cdot PT(;emx_{p\cdot};r',45,SSD_{OCD}) + SPR(l;emx_{p\cdot};r')}$$

where SSD_{OCD} is the source to skin distance in the OCD measurement geometry, r' is the radial distance scaled to depth l from SSD_{OCD}, and $emx_{p\cdot}$ is the maximum square field size used to measure the OCDs. $OCD(l;\ emx_{p\cdot};r',45,SSD_{OCD})$ is calculated by interpolation from a table, and $PT(;emx_{p\cdot};r',45,SSD_{OCD})$ is calculated by the product of

PT for the maximum collimator width and maximum collimator length. The scatter phantom ratio, SPR(l;$emx_{p'}$;r') is estimated by Day's [Day 50] rule [CMS Appendix C], where the field is divided into four sections, and each contribution is computed separately. The division of the field is illustrated in Figure 1-9. The four rectangular fields are: E_1xE_1, E_2xE_2, E_1xE_2, and E_2xE_1, where $E_1 = emx_{p'}+1.4142*r'$, and $E_2 = |emx_{p'}-1.4142*r'|$. Thus

$$SPR(l;emx_{p'};r') = 0.25 \cdot SPR(l;E_1xE_1;0) + g \cdot 0.25 \cdot SPR(l;E_1xE_2;0) + g \cdot 0.25 \cdot SPR(l;E_2xE_1;0) + 0.25 \cdot SPR(l;E_2xE_2;0) \quad (1.59)$$

where

$$g = \begin{cases} 1 & if\ emx_{p'} > 1.4142 \cdot r' \\ -1 & if\ emx_{p'} < 1.4142 \cdot r' \end{cases}.$$

Furthermore, SPR(l;ExE;0) is calculated using equation 1.57, and substituting R_n with ExE, and e_n with E.

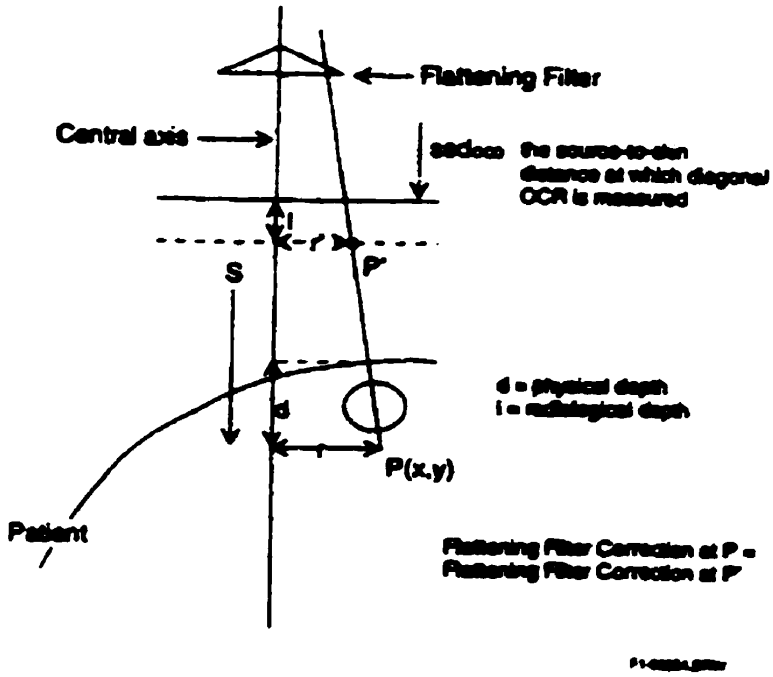

Figure 1-8 INT(l;;r) calculation geometry and OCD measurement geometry [CMS]

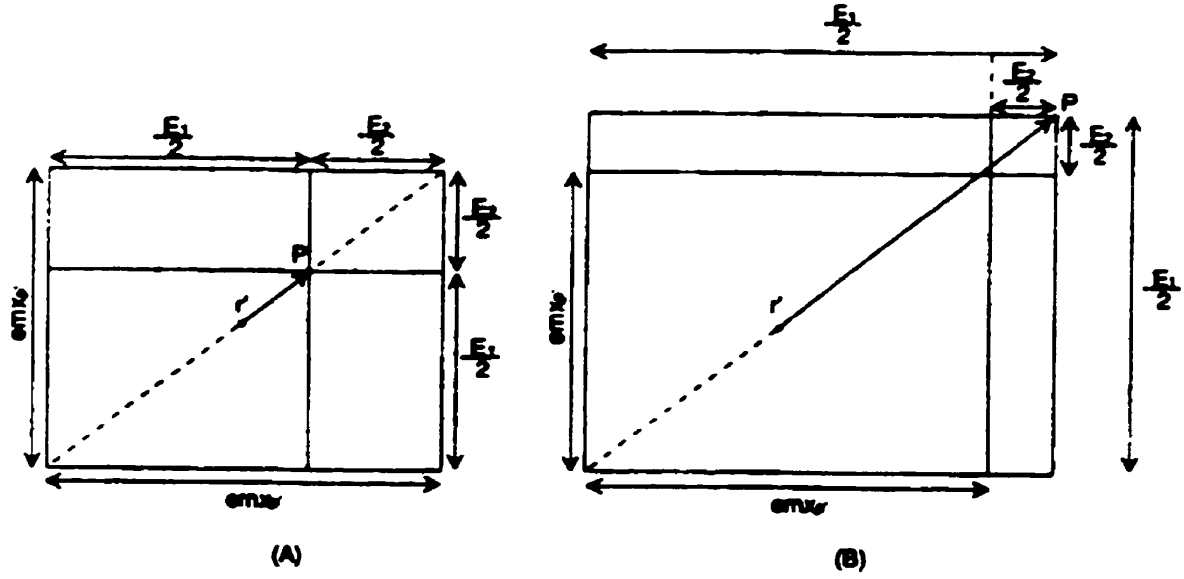

Figure 1-9 Four rectangular fields used in Days's rule – (A) illustrates the fields formed when the point of calculation, P, lies within the field, and (B) illustrates the fields formed when P lies outside the field [CMS]

Relative Dose

The relative dose at each fanline/depthline intersection point, for relative dose beam weighting, is calculated as:

1.60 $$R_{xyz} = \frac{D_{xyz}^{\infty}}{D_{w}^{\infty}} \cdot w$$

where w is the beam weight, describing the relative dose contribution of the beam to its weight point, and D_w^{∞} is a value proportional to the dose, given by equation 1.44, at the weight point. The value of D_w^{∞}, assuming open customized port normalization and wedged normalization, is calculated by neglecting the customized port, ie.

1.61 $$D_{w}^{\infty} = \left(\frac{1}{s_w}\right)^2 \cdot \{INT(l_w;;r_w) \cdot WEGFAC(;;r_w,th_w) \cdot [TPR(l_w;0;0) \cdot PT(;fd_w,fco,0;r_w,th_w,s_w) + SPR(l_w;fd_w,fco,0;r_w,th_w)]\}$$

where l_w is the radiological depth of the weight point, r_w is the radial distance of the weight point from the central axis, s_w is the axial distance of the weight point along the central axis from the source, fd_w is the collimator setting, scaled to s_w, in open port normalization, fco is the field center off central axis distance, and th_w is the angle subtended by the radial vector, r_w, and the collimator axis along the beam width.

These relative dose values, R_{xyz}, are then interpolated onto a user-defined patient dose matrix. This patient dose matrix is either a volume, defined by NX columns, NY rows, and NZ slabs, or a set of selected planes. The precision of this grid is controlled by the user. The values stored in this patient dose matrix are then used to display isodose curves by normalizing the relative doses to the relative dose at a selected point, the normalization point, and converting to a percent dose value, ie.,

1.62 $$\%IsodoseValue_{xyz} = \frac{R_{xyz}}{R_{norm}} \cdot 100\% .$$

1.2.2 Monitor Unit Calculations

The monitor units required for a given beam are determined by:

1.63 $$MU = \frac{Dose\_Delivered\_to\_the\_Weight\_Point}{Dose\_Output\_at\_the\_Weight\_Point} .$$

The dose delivered to the weight point is equal to

1.64 $$\frac{\frac{D_{pres}}{\#fractions}}{IsocurveValue} \cdot w$$

where D_{pres} is the dose prescribed to the normalization point, and IsocurveValue is the sum of relative doses at the plan normalization point. The dose output at the weight point is given by

1.65 $$\frac{D(dw, lw; fdw, fco, 0; rw, th_w, sw)}{MU} = D_w^{\infty} \cdot \frac{\frac{Dc(dc; ec; 0, sc)}{MU}}{TPR(dc; ec; 0)} \cdot \left[\frac{Sp(0)}{Sp(ec)}\right] \cdot Tray \cdot sc^2 .$$

2 Methods and Materials

The models of radiation dose calculation, discussed in the previous chapter for the two treatment planning systems, require measurement of some basic data including output factors, head scatter factors, percentage depth doses, diagonal star profiles and transmission through beam modifying devices. These measurements are only needed for a set of square field sizes. In order to test the ability of models to predict doses for asymmetric fields, MLC fields, blocked fields and treatments delivered using dynamic collimation, another set of measurements are needed. This chapter provides a comprehensive list of such measurements including the equipment and experimental set-up. This chapter also briefly outlines the calculation procedure of measured parameters by the two treatment planning systems.

2.1 Measurements and Calculations

All measurements were performed on the Siemens dual energy (6MV and 23MV) linac (KD2B), equipped with a MLC and a virtual wedge^{TM}. The inner 27 pairs of leaves of the MLC project to 1cm width, and the outer two pairs of leaves project to 6.5cm width at the isocenter. Each leaf is capable of travelling from a maximum opening of 20 cm on one side to an overtravel of 10 cm on the opposite side of the central axis. When the collimator is at zero degrees, the leaf travel is in the cross plane direction. At CCMB, comprehensive daily and monthly QA programs have been instituted to ensure the geometric as well as radiographic accuracy of leaf positions [Lew 96].

The virtual wedge^{TM} system works as follows. The field size in the wedge gradient direction is defined by independent collimator jaws. Specifically, the jaw on the

toe side of the wedge (corresponding to the thin side of the wedge) stays stationary during a treatment while the jaw on the heel side of the wedge travels during the beam delivery. Initially the moving jaw is close to the stationary jaw (1cm gap) and then it is moved to its final position at a constant speed while the dose rate is varied to produce a wedge like gradient in the delivered dose.

It should be noted that CMS-focus dose not account for hardening of the beam due to physical wedges and results in significant errors for thick wedges. However, since physical wedges are not used for this treatment unit, this shortcoming of CMS-focus will not be evaluated in this study.

2.1.1 Head Scatter Factors

Head scatter factor is defined as the relative change in treatment unit output in air, excluding the dose due to contaminant charged particles, with respect to a standard field size. Head Scatter Factors were determined from in air measurements at the source to axis distance (SAD=100cm), normalized to a reference field (10cm x 10cm field at SAD).

2.1.1.1 Equipment and Set-up

Measurements were taken using an electrometer (Keithley Instruments, ser 15188, mod 35614), coaxial cable, a thimble ion chamber (PTW Freiburg, Germany, N 233643 – 289(90), TYP 9732-2), and brass build-up caps of thickness 0.21 cm for 6MV and 0.81 cm for 23MV beams. The thickness of the brass build-up cap was chosen to exclude the detection of charge particle contamination from the treatment head [AA 89]. The electrometer was set at 10^{-8} C, -100% bias, and range 2. The following is a diagram

(Figure 2-1) of the beam axis and the position of the collimator jaws with respect to the gantry as seen in the beams eye view.

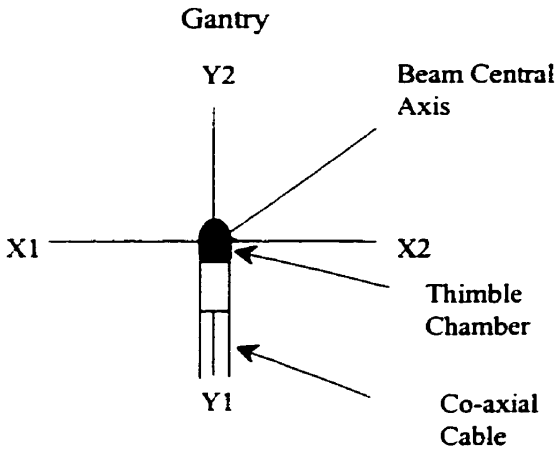

Figure 2-1 Beam axes and collimator jaw positions with respect to the gantry as seen in the beam's eye view.

A set of 7.5 cm thick diverging edge blocks were used in this study.

2.1.1.2 In-air Measurements

Measurements for the fields listed in Table 2-1 were performed for two beam energies (6MV and 23MV) and the head scatter factors determined by normalizing the chamber reading for a given field by the chamber reading for the reference field. No corrections for temperature and pressure were made since frequent measurements of the reference field were taken. All fields were measured twice for a beam setting of 100 monitor units (MU). For the square and asymmetric fields, measurements were taken at the middle of the field with the collimator and gantry both at 0°. For MLC and blocked fields, measurements were taken on the beam central axis. Diagrams of patterns 3 through 10 are illustrated in Figure 2-2 through Figure 2-9.

Table 2-1: In-Air Fields Measured (collimator jaw positions given in cm)

Square Fields (X:Y), $\theta_{col} = 0°$, $\theta_{gan} = 0°$
15 x 15, 20 x 20, and 40 x 40*

Asymmetric Fields (X1:X2 x Y1:Y2), $\theta_{col} = 0°$, $\theta_{gan} = 0°$
Right Quadrant- 0:5 x 0:5, 0:10 x 0:10, 0:15 x 0:15, 0:20 x 0:20
Right Half - 0:5 x 5:5, 0:10 x 10:10, 0:15 x 15:15, 0:20 x 20:20*
Top Half - 5:5 x 0:5, 10:10 x 0:10, 15:15 x 0:15, 20:20 x 0:20*

MLC fields (Y1:Y2, θ_{coll},θ_{gantry})
Pattern 3 - (7.5:7.5, 0°, 0°)
Pattern 4 - (2.8:3.0, 0°, 0°)
Pattern 5 - (5.5:5.5, 0°, 0°)
Pattern 6 - (9.5:9.5, 0°, 0°)
Pattern 7 - (9.5:9.5, 88°, 0°)
Pattern 8 - (13.5:13.5, 90°, 0°)
Pattern 9* - (13.5:13.5, 270°, 0°)*
Pattern 10 - (5.0:5.0, 0°, 0°)

Blocked Fields (X x Y, θ_{coll},θ_{gantry})
Pattern 3 - (15 x 15, 0°, 0°)
Pattern 4 - (5.4 x 2.8:3.0, 0°, 0°)
Pattern 5 - (28.4 x 11, 0°, 0°)
Pattern 6 - (20 x 20, 0°, 0°)
Pattern 7 - (26.4 x 19, 88, 0°)
Pattern 8 - (5.2:3.9 x 27, 90°, 0°)
Pattern 9* - (39 x 27, 270°, 0°)*
Pattern 10 - (10 x10, 0°, 0°)

**fields not supported by CMS*

Square fields were measured and compared to previous measurements. The reproducibility of experimental set-up was within ±0.5%. In addition, measurements of fields defined by the collimator settings for the blocked fields, but with the blocks removed, were measured to determine the modulation in the flattening filter scatter, if any, produced by the blocks.

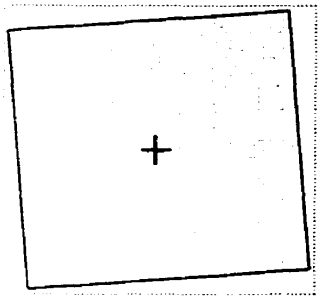

Figure 2-2 Pattern 3 (15 x 15) – The dashed lines indicate the jaw positions for the blocked field, and the shape formed by the solid lines indicates the block and MLC shape. The cross hairs denote the location of the beam central axis.

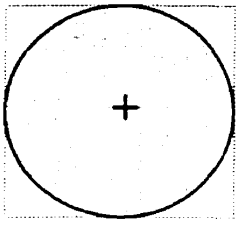

Figure 2-3 Pattern 4 (5.4 x 2.8:3.0) – The dashed lines indicate the jaw positions for the blocked field, and the shape formed by the solid lines indicates the block and MLC shape. The cross hairs denote the location of the beam central axis.

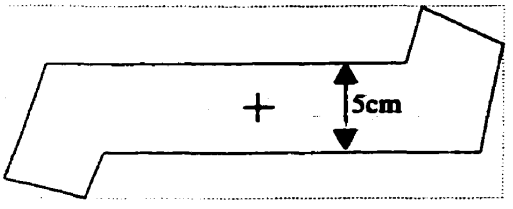

Figure 2-4 Pattern 5 (28.4 x 11) – The dashed lines indicate the jaw positions for the blocked field, and the shape formed by the solid lines indicates the block and MLC shape. The cross hairs denote the location of the beam central axis.

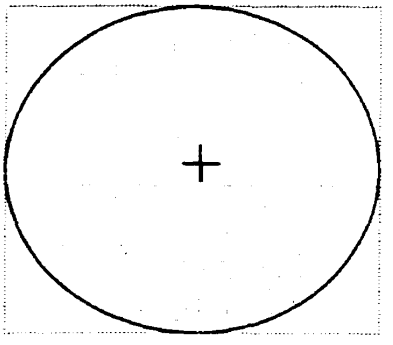

Figure 2-5 Pattern 6 (20 x 20) – The dashed lines indicate the jaw positions for the blocked field, and the shape formed by the solid lines indicates the block and MLC shape. The cross hairs denote the location of the beam central axis.

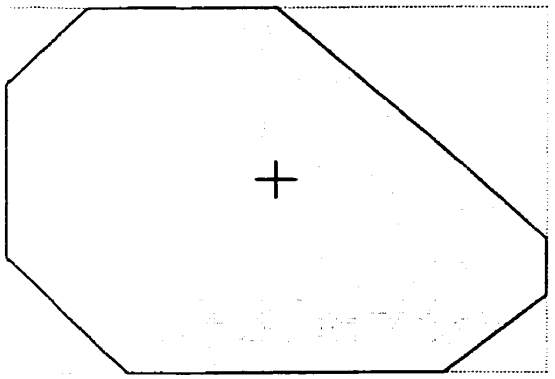

Figure 2-6 Pattern 7 (26.4 x 19) – The dashed lines indicate the jaw positions for the blocked field, and the shape formed by the solid lines indicates the block and MLC shape. The cross hairs denote the location of the beam central axis. The pattern is displayed with the collimator angle at 0°, but was measured at 88°.

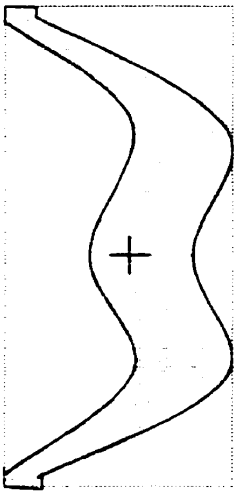

Figure 2-7 *Pattern 8 (5.2:3.9 x 27) – The dashed lines indicate the jaw positions for the blocked field, and the shape formed by the solid lines indicates the block and MLC shape. The cross hairs denote the location of the beam central axis. The pattern is displayed with the collimator angle at 0°, but was measured at 90°.*

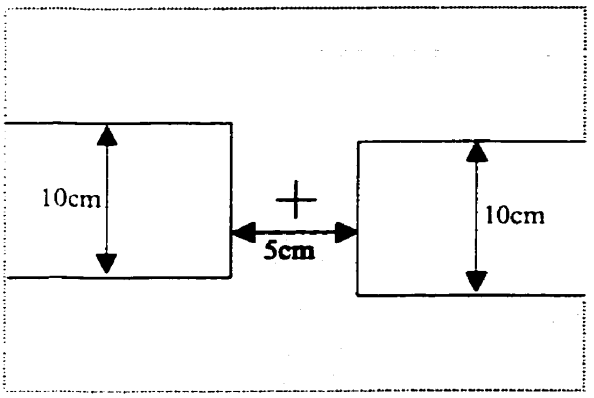

***Figure 2-9** Pattern 9 (39 x 27) – The dashed lines indicate the jaw positions for the blocked field, and the shape formed by the solid lines indicates the block and MLC shape. The cross hairs denote the location of the beam central axis. The pattern is displayed with the collimator angle at 0°, but was measured at 270°.*

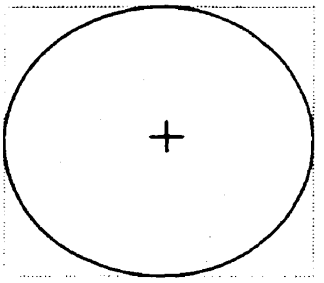

***Figure 2-8** Pattern 10 (10 x 10) – The dashed lines indicate the jaw positions for the blocked field, and the shape formed by the solid lines indicates the block and MLC shape. The cross hairs denote the location of the beam central axis.*

2.1.1.2.1 Uncertainty Measurements

There are essentially three sources of uncertainty in the above measurements: (1) set-up uncertainty (independent of the measured reading); (2) variation in the beam (independent of the measured reading); and (3) variation in the electrometer (dependent on the measured reading). These uncertainties were estimated from two sets of measurements: (1) 15 consecutive readings on the central axis for a 10x10 field, 6MV beam, 100 MU, and the set-up described above for in-air measurements (recording temperature and pressure) ; and (2) measurements for a 10x10 field on the central axis, and an asymmetric field (0:10 x 0:10) at the center of the field, for a 6MV beam and 100 MU. The experimental set-up was repeated 9 times for the second set of measurements. Each set-up involved moving the chamber and repositioning it at the center of the field. Temperature and pressure were recorded for each set-up.

2.1.1.3 Calculations

For each field and energy, two chamber readings were recorded and averaged. Head scatter factors were calculated by dividing the average chamber reading for the given field by the mean of the reference field chamber reading. The mean reference field chamber reading is the mean of the two nearest average reference field readings taken before and after the measurement of the given field.

2.1.1.3.1 Uncertainty Calculations

The standard deviation of the set of 15 consecutive measurements described in section 2.1.1.2.1 was determined. This represented the uncertainty in the measurements due to variations in the beam and electrometer, $\sigma^{air}_{B,E}$. Furthermore, the total uncertainty

in the measurements due to set-up, electrometer and beam variations, σ_T^{air}, was determined from the second set of measurements described in section 2.1.1.2.1. Each reading, M, was corrected for the temperature, T, and pressure, P, recorded at the time of completion of the set-up, as follows

$$M' = M\left(\frac{760}{P}\cdot\frac{273+T}{295}\right)$$

where M' is the corrected chamber reading. The standard deviations were then calculated for the set of on-axis (10x10) corrected chamber readings, and the set of off-axis (0:10 x 0:10) corrected chamber readings, yielding $\sigma_{T\_on}^{air}$, and $\sigma_{T\_off}^{air}$, respectively. For interest sake the uncertainty due to the set up could then be determined from the difference between the total uncertainty and the beam and electrometer variation, ie. $\sigma_{S\_on/off}^{air} = \sqrt{(\sigma_{T\_on/off}^{air})^2 - (\sigma_{B/E}^{air})^2}$.

The uncertainty in a single, in-air, on/off-axis, chamber measurement was determined from the total uncertainty $\sigma_{T\_on/off}^{air}$. Furthermore, the total uncertainty was assumed to be independent of the measured reading. This is justified since the variation in the electrometer is a result of photon statistics and is therefore proportional to $1/\sqrt{N}$, where N is the number of detected photons. Due to the large magnitude of N, variation in the electrometer is assumed to be negligible, and therefore the total uncertainty in the measurement is assumed to be independent of the chamber reading. Finally the uncertainty in the head scatter factors were determined using standard rules for the propagation of errors.

2.1.2 Output Factors

The output factor for a given field is defined as the relative change in absorbed dose in water with respect to a standard field size and depth. Output Factors for various fields were determined at three different depths (dmax, 5cm, and 10cm) for a source to surface distance of (SSD=100-dmax), and normalized to the reference field measured at dmax. All measurements were carried out in a water phantom.

2.1.2.1 Equipment and Set-up

Measurements were taken using the same electrometer, cable, and ion chamber as used in the in-air measurements. A PTW scanning water tank (PTW Frieburg MP3-S, model no. 41002-0037) was used in all measurements. The electrometer settings were the same as for the in-air measurements, ie. 10^{-8} C, -100% bias, and range 2. The PTW scanning water tank is a perspex tank with dimensions 50cm x 59.4cm x 50cm (WxLxH).

2.1.2.2 Phantom Measurements

Measurements for the fields listed in Table 2-1 were performed at three different depths (dmax, 5cm, and 10cm) and two beam energies (6MV and 23MV). Square fields were measured and compared to previous measurements. The measured output factors for square fields were within ±1.0% of the previous measurements. Output factors were determined by normalizing the chamber reading for a given field by the chamber reading for the reference field at dmax. No corrections for temperature and pressure were made since frequent measurements of the reference field were taken. All fields were measured twice, each for a setting of 100 MU. For the square and asymmetric fields, measurements were taken at the centre of the field with the collimator and gantry both at 0°. For MLC

and blocked fields, measurements were taken on the beam central axis. As for the determination of head scatter factors, measurements of fields defined by the collimator settings for the blocked fields, but with the blocks removed, were measured to determine the modulation in the flattening filter scatter, if any, produced by the blocks.

In addition to the fields listed in Table 2-1, output factor measurements were performed for virtual wedges in asymmetric fields. These measurements, listed in Table 2-2, were performed at the centre of each field instead of at the beam central axis. Measurements for these fields were performed with the 15°, 30°, 45°, and 60° virtual wedge™, each for two beam energies (6MV and 23MV) and at three different depths (dmax, 5cm, and 10cm). The wedge gradient is along the Y1-Y2 jaws, and was created with Y2 as the moving jaw, and Y1 the stationary jaw. Figures 2-10, 2-11, and 2-12 demonstrate the collimator jaw positions, and the positioning of the wedge for the right quadrant, top half, and right half fields, respectively.

Table 2-2 In-Phantom Virtual Wedge™ Fields (collimator jaw positions given in cm)

Asymmetric Fields (X1:X2 x Y1:Y2)

Right Quadrant- 0:5 x 0:5, 0:10 x 0:10, 0:15 x 0:15*, 0:20 x 0:20*
Right Half - 0:5 x 5:5, 0:10 x 10:10
Top Half - 5:5 x 0:5, 10:10 x 0:10, 15:15 x 0:15*, 20:20 x 0:20*

*fields not supported by CMS

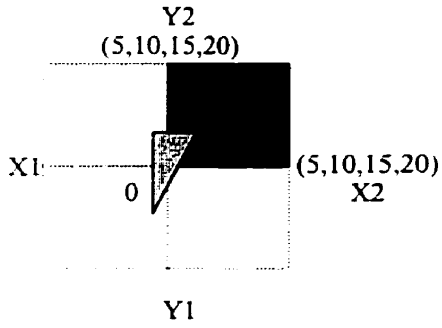

Figure 2-11: Jaw and wedge positions for the right quadrant of the field.

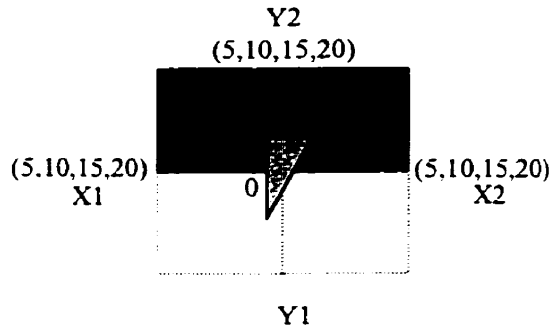

Figure 2-10: Jaw and wedge positions for the top half of the field.

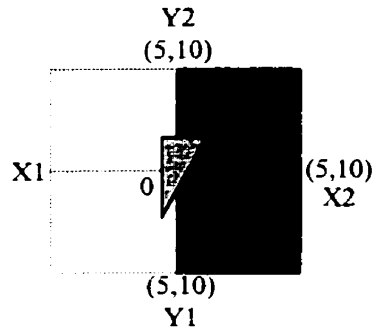

Figure 2-12: Jaw and wedge positions for right half of field.

2.1.2.2.1 Uncertainty Measurements

The sources of uncertainty discussed for the in-air measurements are also applicable to the in-phantom measurements. These uncertainties were determined from two sets of measurements: (1) 15 consecutive chamber readings on the central axis for a 10x10 field, 6MV beam, 100 MU, at a depth of 1.5cm and SSD of 98.5cm (recording temperature and pressure) ; and (2) measurements for a 10x10 field on the central axis, and an asymmetric field (0:10 x 0:10) at the center of the field, for a 6MV beam, 100 MU, at 1.5cm, with a SSD of 98.5cm, each performed for 6 different set-ups. Each set-up

involved moving the water tank, re-aligning and leveling the tank, centering the chamber in the field, and adjusting the water level to an SSD of 98.5 cm. Temperature and pressure were recorded for each set-up.

2.1.2.3 Calculations

For each field, energy and depth, two chamber readings were recorded and averaged. Output factors were calculated by dividing the average chamber reading for the given field by the mean reference field chamber reading. The mean reference field chamber reading is the mean of the nearest average reference readings before and after the measurement of the given field.

2.1.2.3.1 Uncertainty Calculations

The method for determination of $\sigma^{air}_{B/E}$, $\sigma^{air}_{S\_on/off}$, $\sigma^{air}_{T\_on/off}$ described in section 2.1.1.3.1 was used in the determination of $\sigma^{ph}_{B/E}$, $\sigma^{ph}_{S\_on/off}$, $\sigma^{ph}_{T\_on/off}$ from the phantom uncertainty measurements, discussed in section 2.1.2.2.1. The uncertainty in a single, in-phantom, on/off-axis, chamber measurement was determined from the total uncertainty $\sigma_{T\_on/off}$, and was assumed to independent of the measured reading. The uncertainty in the output factors were determined using standard rules for the propagation of errors.

2.1.3 Isodose Distributions

For each field listed in Table 2-3, isodose distributions were measured in both the cross plane and in-plane passing through the centre of the field.

2.1.3.1 Equipment and Set-up

Isodose distributions were determined from measured depth doses, in-plane (y) and cross-plane (x) profiles, by using MEPHYSTO software (Version 6.3). These measurements were performed using the PTW scanning tank (MP3-S), interfaced with a PC running MEPHYSTO, an electrometer (PTW Freiburg model no. 41004-0038) and two ion chambers (PTW Freiburg, M-31002-0423(4)), used as data and reference chambers.

2.1.3.2 Beam Scanning Measurements

For each field listed in Table 2-3, a depth dose curve, in-plane profiles and cross plane profiles were measured. The depth dose measurements were performed at the center of the fields. For 6MV beams, in-plane and cross plane profiles were measured at depths of 1.5cm (dmax), 2.5cm, 3.5cm, 5cm, and 10cm. For 23MV beams, in-plane and cross plane profiles were measured at depths of 3.5cm(dmax), 4.5cm, 5cm, 7.5cm, and 10cm. The depth dose measurements were made with 1mm steps from 0 to 5cm and 2mm steps from 5cm to 15cm, and 3mm beyond 15cm. Majority of the profiles were measured with 2mm steps in the center of the field and 1mm steps in the penumbra region. The exceptions are the profiles measured for block patterns 3 and 6, for both 6VM and 23MV, where the profile steps were 2mm across the entire field.

Table 2-3 Isodose Distributions (collimator jaw positions given in cm)

Asymmetric Fields (X1:X2 x Y1:Y2)
- 5:15 x 10:10
- 15:5 x 10:10
- 0:10 x 10:10
- 10:0 x 10:10

Blocked Fields (X x Y, θ_{coll},θ_{gantry})
- Pattern 3 - (15 x 15, 0°, 0°)
- Pattern 6 - (20 x 20, 0°, 0°)

MLC fields (Y1:Y2, θ_{coll},θ_{gantry})
- Pattern 3 - (7.5:7.5, 0°, 0°)
- Pattern 6 - (9.5:9.5, 0°, 0°)

2.1.3.3 Isodose Display

Isodose distributions were calculated from the above measurements by MEPHYSTO, which interpolates between the measured PDD and profiles to produce the isodose curves. Each isodose distribution was normalized to 10cm depth at the center of the field. The isodose lines displayed in the distributions were 20%, 40%, 50%, 60%, 80%, 100%, 120% and 140% (for 6MV only).

2.2 Treatment Planning Output

2.2.1 TMS Calculations

Calculations in TMS were performed using either a 60cm x 60cm x 60cm water phantom or a 30cm x 30cm x 30cm water phantom, depending on the field size of the beam under investigation. The calculated head scatter factors were generated in TMS by using the *Protocol and Export* tool in the *Evaluation* work module. The reference dose point for each field was placed at the chamber location in the measurement procedure.

The MLC and block patterns were modeled by scanning the printouts of the patterns from the record and verify system (Lantis – Siemens Medical Systems) and storing them as an image in the *Film Scanning* module. The image is then introduced into the study and referenced in the beams eye view (BEV) of the *Beam Modeling* work module where the MLC and block contours are drawn to match the image.

The output factors were generated, in general, using the *Line Dose* function in the *Beam Modeling* work module, which produces a file containing the normalized dose along the desired line, as described in section 1.1.4.2. The output factor normalization was selected while the evaluation calculation algorithm was not implemented. The *Line Dose* function for virtual wedged fields automatically normalizes to the toe of the wedge. Thus, it was not possible to use this for determination of the output factors for some of the virtual wedge measurements, namely the asymmetric fields 0:5 x 5:5 and 0:10 x 10:10. The output factors for these two fields, for all of the virtual wedge angles, were calculated using the MU, by the method described in section 2.2.2. The MU were obtained from the dose plan protocol, which assumes a prescribed dose of 100cGy, unless otherwise specified.

The isodose distributions were generated from the *Display Doses* tool in the *Beam Modeling* work module, with the normalization point positioned at a depth of 10cm, at the center of the field. Distributions were generated for both the in-plane and cross-plane located at the center of each field listed in Table 2-3, with a calculation grid size of less than 0.5 cm. The isodose lines displayed in the distributions were 20%, 40%, 50%, 60%, 80%, 100%, 120% and 140% (for 6MV only).

2.2.2 CMS Calculations

CMS-focus does not provide head scatter factors for arbitrary fields since it does not explicitly model the head scatter. The best approximation to the head scatter would be obtained by interpolation from measured head scatter factors for square open fields.

Output factors were determined from MU calculations in CMS as follows:

2.1 $$OF = \frac{D_{test} / MU}{D_{10x10}^{d_{max}} / MU}$$

where D_{test} is the point of calculation in each of the fields. The MU necessary to deliver 100 cGy to dmax in a 10x10 field is 100 MU, since this is the beam calibration point. Thus $D_{10x10}^{d_{max}} / MU = 1$, and the output factor becomes OF = 100/MU, where MU is the number of monitor units necessary to deliver 100 cGy to the calculation/measurement point. MU calculations in CMS were performed on a 30x30 phantom in *Isodose Plan*, using selected planes for the calculation mode and relative dose normalization.

The maximum field size supported by CMS is 35cm x 35cm, thus the fields superscripted with a * in Table 2-1 were not calculated with CMS. The blocks and MLC patterns were digitized using the tablet. Since the MLC is not explicitly modeled by CMS, output factors generated for blocks were also used for the MLC patterns. In addition virtual wedges are not explicitly modeled by CMS, thus output factors for physical wedges, designed to replicate the virtual wedge, were calculated and compared with measured virtual wedge output factors for the fields listed in Table 2-3. Fields superscripted with a * in Table 2-2 were not supported by CMS.

Isodose distributions were generated in *Isodose Plan* using selected planes for the calculation mode, and relative dose normalization. The spacing of points in the rectilinear

dose matrix was a maximum of 0.2 cm. Since the MLC is not explicitly modeled by CMS, isodose distributions generated for blocks were also used for the MLC patterns. The isodose distributions were normalized to a 10cm depth at the center of each field. The isodose lines displayed in the distributions were 20%, 40%, 50%, 60%, 80%, 100%, 120% and 140% (for 6MV only).

2.3 Verification of TPS

2.3.1 Head Scatter Factors and Output Factors

Comparisons between measured and TPS calculated values were made by calculating the local percent of the measured output or head scatter factors as follows

2.2 $$\Delta OF = \frac{OF_{calc} - OF_{meas}}{OF_{meas}} \cdot 100\%$$

where OF is replaced by HSF for head scatter factor [Helax].

2.3.2 Isodose Distributions

Isodose distributions created by TMS and CMS were evaluated by comparing them with measured distributions produced by MEPHYSTO. The comparison was carried out using a light box, and overlaying a measured distribution on a calculated distribution. Four different regions of each distribution were evaluated: (1) the low gradient central beam region along the central axis of the field; (2) the low gradient inner beam region (including isodose gradients less than 30%/cm and excluding the central axis); (3) the high gradient low dose region where the gradient is >30%/cm; and (4) the penumbral region.

2.3.2.1 Low Gradient Central Beam Region

The low gradient central beam region, is a low gradient region on the central axis of the field. The local percent of the maximum deviation observed between any set of measured and calculated isodose lines on the central axis of the field was recorded. This was determined by the method described in the section below. In this region, the isodose distributions were always lined up at 10cm depth at the middle of the field.

2.3.2.2 Low Gradient Inner Beam Region

A region is considered to be low gradient if the change in the isodose lines is <30%/cm [Van 93]. The inner beam region is the central high dose portion of the beam. In the low gradient inner beam region, the local percent of the maximum deviation observed between any set of measured and calculated isodose lines was recorded, excluding deviations observed at the central axis of the field. First the measured % isodose value of the calculated isodose line, L_{calc}^{meas}, was found by interpolating at the position of the calculated isodose line L_{calc}, between two measured isodose lines. The local percent of the measured isodose value was then determined by

2.3
$$\Delta L = \frac{L_{calc} - L_{calc}^{meas}}{L_{calc}^{meas}} \cdot 100\% .$$

Extrapolation was used where interpolation was not possible. In general, in the low gradient inner beam region the isodose distributions were lined up at 10cm depth at the centre of the field. Exceptions to this include points approaching the high gradient region where the difference in measured and calculated isodose lines was in the direction of the field edges. In this case, it was more appropriate to line-up the distributions at the field

edge at 10cm depth. The field edge was assumed to be the position of the 50% isodose curve at 10cm depth. This deviation, ΔL, was determined for each side of the distribution.

2.3.2.3 High Gradient Region

The high gradient region, is the region in which the isodose gradient exceeds 30%/cm. In this region the deviation observed between sets of measured and calculated isodose curves was recorded as a displacement, measured in the direction perpendicular to the beam central axis. In addition, the isodose value where this displacement was occurring was also recorded. Evaluations in the high gradient region were carried out with the distributions lined up at the field edge, at 10cm depth, on the side of the distributions being investigated. The reason for lining up the field edge is due to the uncertainty in the jaw positions (±2mm) during measurements. Maximum displacements were recorded for each side of the distributions.

2.3.2.4 Penumbral Region

In the penumbral region, the penumbra was measured as the distance between the 80% and 20% isodose lines at the normalization depth (10cm). This was measured on both sides of each distribution, and then the difference between calculated and measured penumbras was determined.

2.3.2.5 Uncertainties

The precision obtainable in the measurement technique of the isodose distributions was 0.7mm. This uncertainty was propagated through, using standard rules for propagation of errors, to give a displacement uncertainty in the high gradient and penumbra region, and a local percent uncertainty in the lower gradient regions.

3 Results and Discussion

Tabulated values of all of the results, including both measured and calculated data, are provided in Appendix A.

3.1 Head Scatter Factors

The total uncertainty in a single measured reading was determined to be $\sigma^{air}_{T\_on\cdot off} = 0.002$ (10^{-8} C).

The results for the measured and calculated head scatter factors for the fields listed in Table 2-1 are provided in the following sections.

3.1.1 Square Fields

Figure 3-1 and Figure 3-2 illustrate the results of the calculated (TMS) and measured head scatter factors for the square fields listed in Table 2-1 for 6MV and 23MV photons, respectively. As expected, the measured head scatter factors increase with increasing field size and are in good agreement with the calculated HSFs. Maximum deviation of 0.3% between measured and calculated HSFs occurs for 6MV beam for a 40x40 field size. This deviation is, however, smaller than the estimated uncertainty in the measurements.

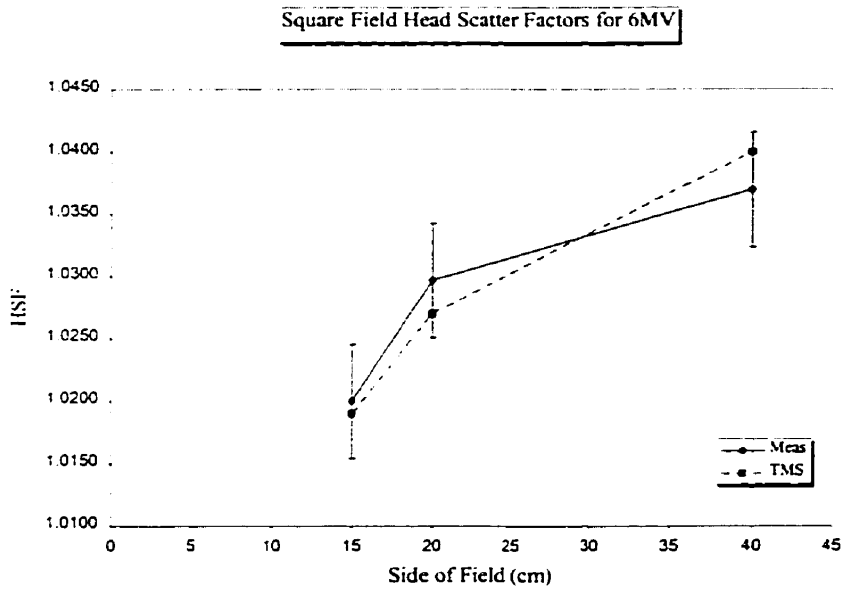

Figure 3-1: Plot of measured and calculated square field HSFs for 6MV photons. Measurements were made on Siemens dual energy linear accelerator at the centre of the field. Calculations were performed on Helax TMS treatment planning system.

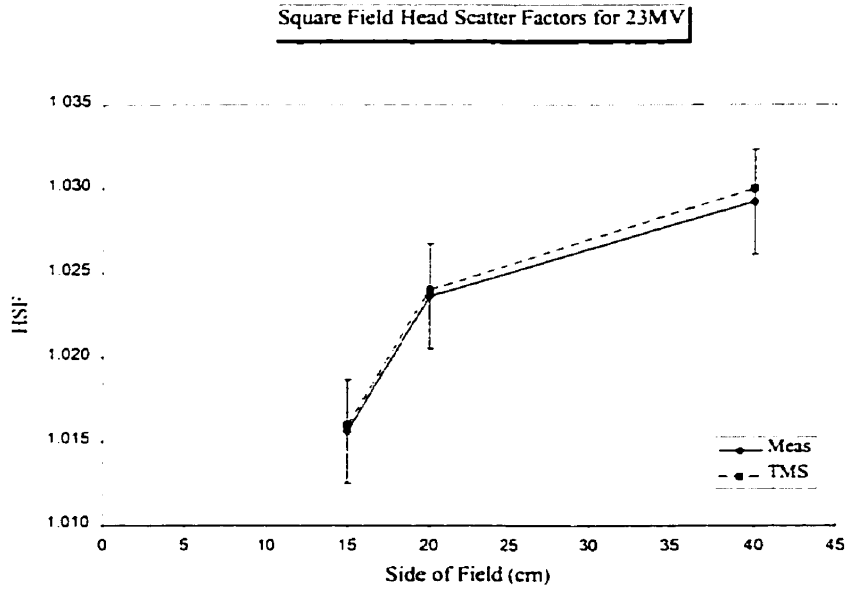

Figure 3-2: Plot of square field HSFs for 23MV photons. Measurements were made on Siemens dual energy linear accelerator at the centre of the field. Calculations were performed on Helax TMS treatment planning system.

3.1.2 Independent Jaws

A comparison of the measured and TMS calculated head scatter factors for the asymmetric fields listed in Table 2-1 is illustrated in Figure 3-3 through Figure 3-8. The head scatter factors are plotted as a function of side x of the field, where the shape of the field is given in the graph title as (X1:X2; Y1:Y2). In general, the measured and calculated head scatter factors are increasing with increasing field size, as expected due to the increased detection of scattered radiation from the flattening filter with increasing field size. The increase in HSF is larger for an increase in a smaller field size than the corresponding increase in a larger field size suggesting that the flattening filter scattered fluence distribution decreases as a function of radial distance from the central axis. The exceptions to this are the measured HSFs in Figure 3-3 and Figure 3-6 representing the measurements for the top half and right half of the field for 23MV photons, respectively. To verify these results, these measurements were taken a second time, and similar results were obtained. In each of these, TMS is strongly overestimating the HSFs at the larger field sizes. In addition Figure 3-3 through Figure 3-8 demonstrate that the deviation between the measured and calculated HSFs is more significant at 23 MV than at 6MV for all of the asymmetric fields.

Jursinic et al have shown that the HSF increases less rapidly with field size when measured with caps of high atomic number materials [JT 99]. This effect is more pronounced at higher energy photon beams than at lower energy photon beams. It is believed that since off-axis softening is much more evident at higher energies, the photon beam spectra at off-axis points becomes significantly lower in energy for a 23 MV beam.

The build-up caps suggested in the TMS-manual are designed to remove all contaminant electrons. However, it is assumed that attenuation of the photon beam per unit incident fluence by the brass cap stays the same for all field sizes. This assumption is strongly violated as the measurement point is moved off-axis and fields become larger since lower energy photons at off-axis points will have larger attenuation. This is the reason for non-physical decrease of measured HSFs for 23 MV photons.

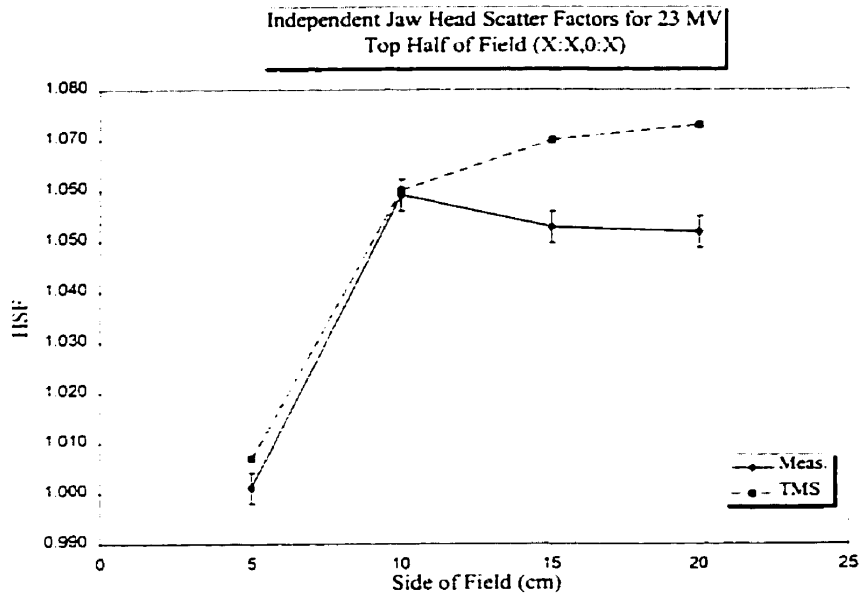

Figure 3-3: Plot of 23MV asymmetric field HSFs for the top half of the field versus the dimension of the side of the field, X. The abscissa is the value of X used in the title to define the field size. Measurements were made on Siemens dual energy linear accelerator at the centre of the field. Calculations were performed on Helax TMS treatment planning system.

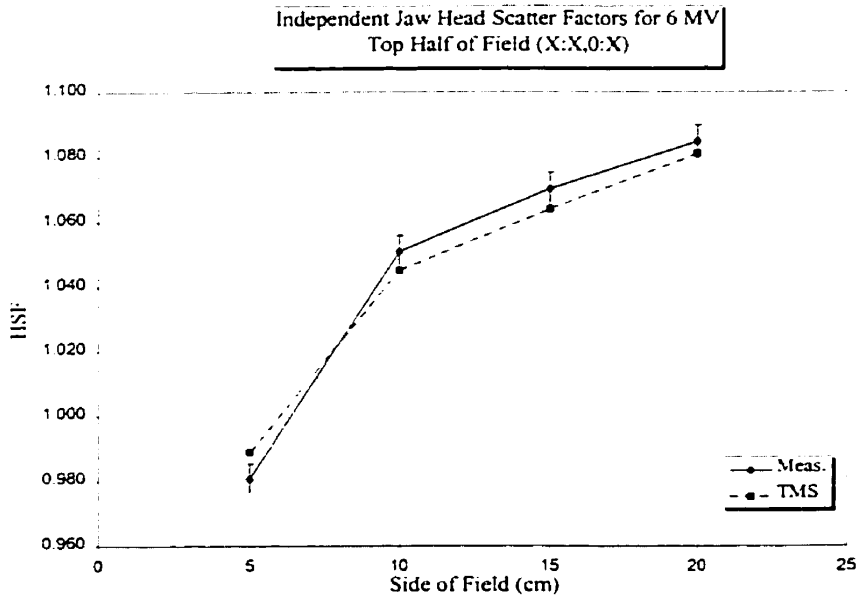

Figure 3-4: Plot of 6MV asymmetric field HSFs for the top half of the field versus the dimension of the side of the field, X. The abscissa is the value of X used in the title to define the field size. Measurements were made on Siemens dual energy linear accelerator at the centre of the field. Calculations were performed on Helax TMS treatment planning system.

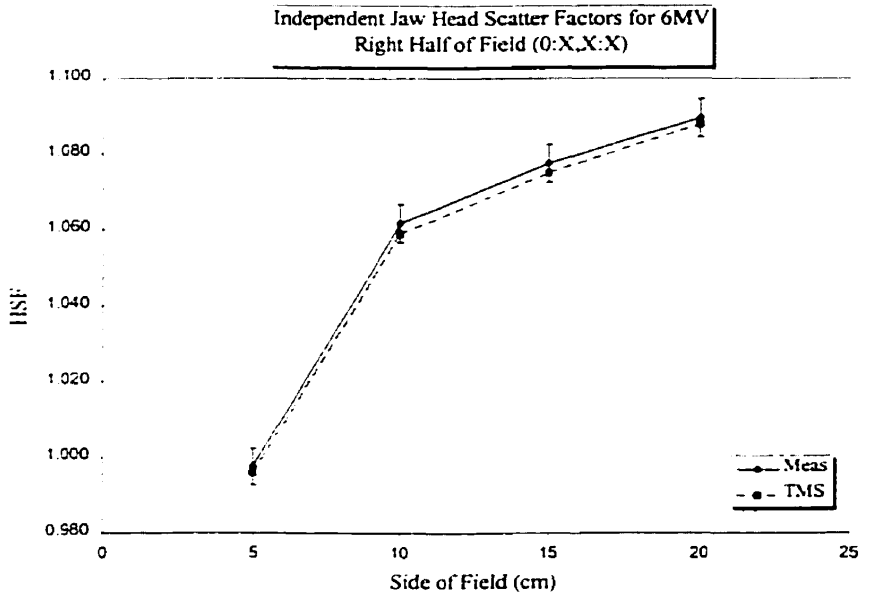

Figure 3-5: Plot of 23MV asymmetric field HSFs for the right half of the field versus the dimension of the side of the field, X. The abscissa is the value of X used in the title to define the field size. Measurements were made on Siemens dual energy linear accelerator at the centre of the field. Calculations were performed on Helax TMS treatment planning system.

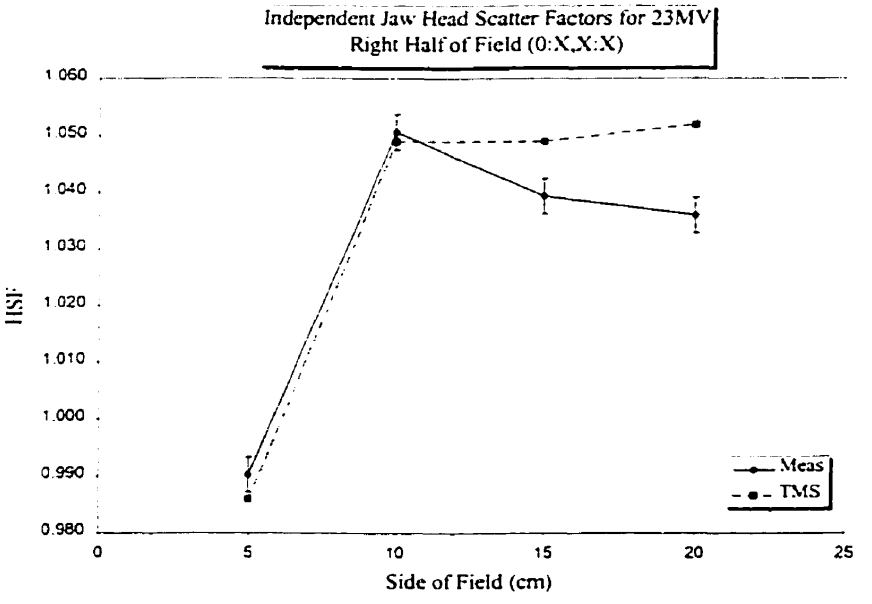

Figure 3-6: Plot of 23MV asymmetric field HSFs for the right half of the field versus the dimension of the side of the field, X. The abscissa is the value of X used in the title to define the field size. Measurements were made on Siemens dual energy linear accelerator at the centre of the field. Calculations were performed on Helax TMS treatment planning system.

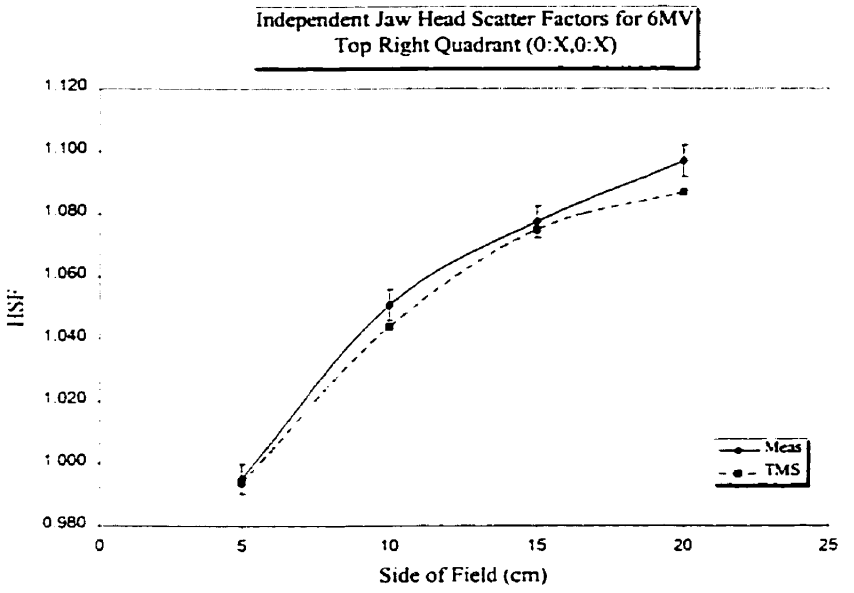

Figure 3-7: Plot of 6MV asymmetric field HSFs for the top right quadrant of the field versus the dimension of the side of the field, X. The abscissa is the value of X used in the title to define the field size. Measurements were made on Siemens dual energy linear accelerator at the centre of the field. Calculations were performed on Helax TMS treatment planning system.

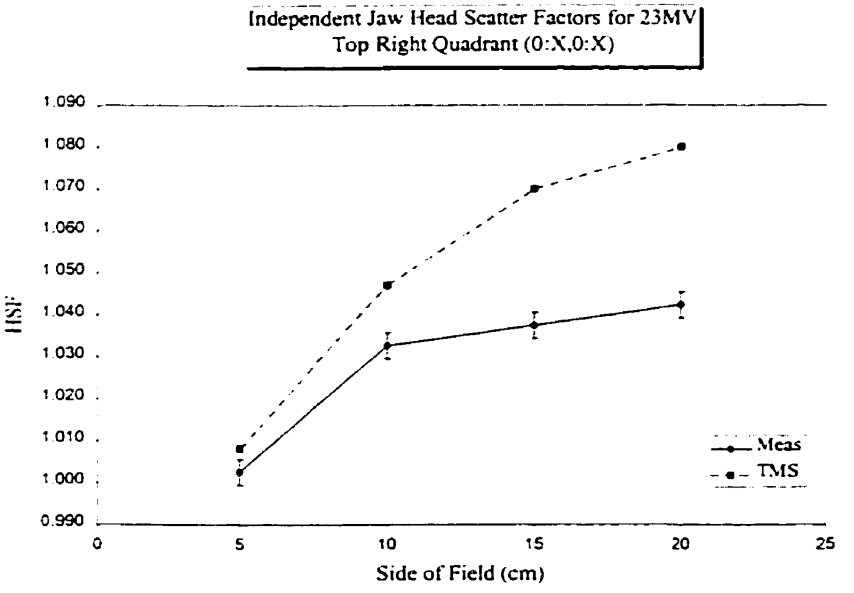

Figure 3-8: Plot of 23MV asymmetric field HSFs for the top right quadrant of the field versus the dimension of the side of the field, X. The abscissa is the value of X used in the title to define the field size. Measurements were made on Siemens dual energy linear accelerator at the centre of the field. Calculations were performed on Helax TMS treatment planning system.

3.1.3 MLC and Blocks

The results for the MLC and blocked fields are not plotted, however, they are provided in Appendix A of this report.

3.1.4 Frequency Distribution

To summarize the results, a frequency distribution of the percent deviation, ΔHSF, between the measured and calculated values for all of the measurements listed in Table 2-1 is provided in Figure 3-9. Negative values indicate that TMS has underestimated the measured values, and positive values indicate that TMS has overestimated the measured values. The distribution is clearly centered around zero, with the outliers mostly on the positive side indicating that TMS is overestimating. The uncertainties in the percent deviations ranged from 0.3% to 0.5% with an average of approximately 0.4%.

Head scatter factors are expected to agree within ±(1-2%) of measured values [Helax]. Deviations exceeding 2% are for asymmetric fields, two in the right quadrant for 23MV with 15 x 15 and 20 x 20 field sizes, and one in the top half for 23MV with a 40 x 20 field size. The latter field has a deviation of (2.0 ± 0.3)% and therefore satisfies this criteria within the limits of experimental uncertainty. The measurements and calculations for these fields were previously illustrated in Figure 3-8 and Figure 3-4, respectively. Furthermore, it is worth mentioning that all of the deviations greater than +1% are due to the asymmetric fields with 23MV photons for the reasons explained in the previous section.

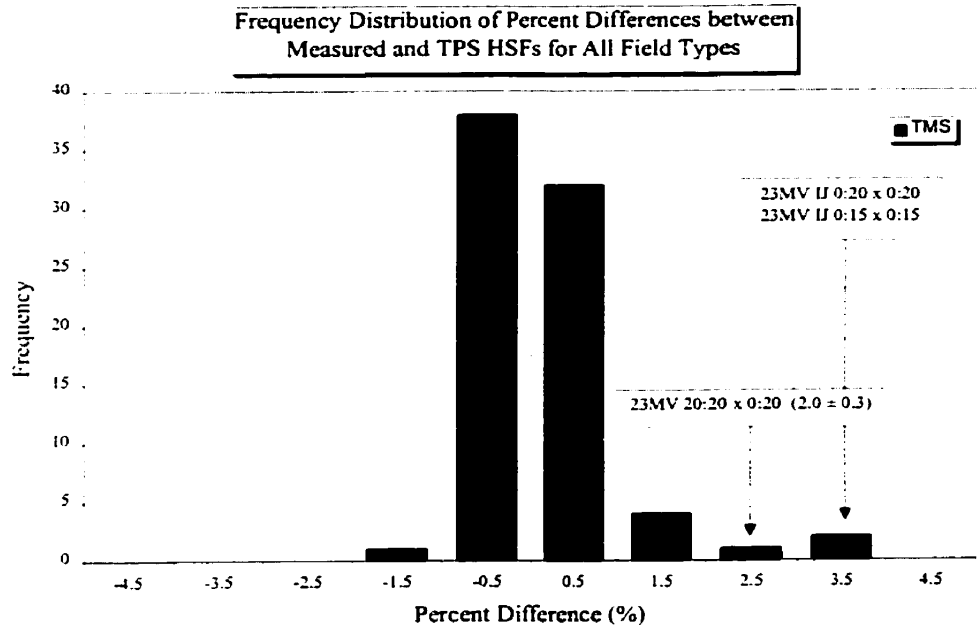

Figure 3-9: Frequency distributions of percent differences, ΔHSF, between measured and calculated (TMS) HSFs for all fields listed in Table 2-1.

3.2 Output Factors

The following values for the total experimental uncertainties were determined: $\sigma^{ph}_{T\_on} = 0.0002$ (10^{-8} C) and $\sigma^{ph}_{T\_off} = 0.0006$ (10^{-8} C). These were used as the uncertainty in a single measured reading and propagated through to provide uncertainties in the measured output factors.

The results for the measured and calculated output factors for the fields listed in Table 2-1 and Table 2-2 are provided in the following.

3.2.1 Square Fields

The measured and calculated (TMS and CMS-focus) OFs for square field sizes at 6MV are plotted in Figure 3-10 where OFs for three different depths are shown. It is seen that the output factors increase with increasing field size and decrease with increasing depth. The increase in output factors with increasing field size is due to the increases in

phantom scatter and head scatter associated with increased field size. The decrease in output factors with increasing depth is a result of the increased attenuation in water. The CMS-focus and TMS calculated output factors are in good agreement with the measured output factors. A similar plot of the 23MV square field output factors is provided in Appendix B.

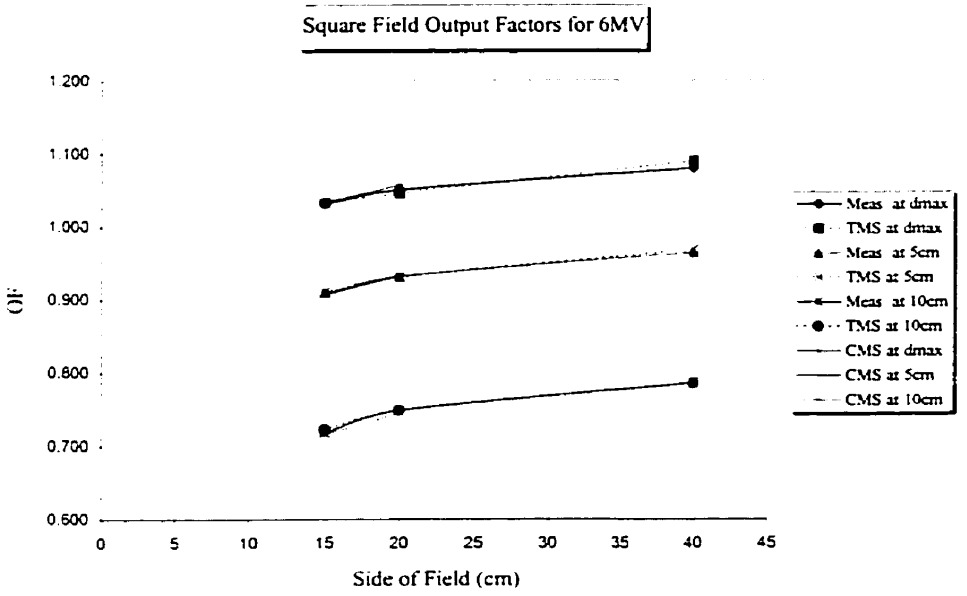

Figure 3-10: Output factors for 6MV square fields. The output is determined in-phantom relative to the output for a 10x10 field at dmax. Measurements were made on Siemens dual energy linear accelerator at the centre of the field. Calculations were performed on Helax TMS and CMS-focus.

Frequency distributions of the percent differences, ΔOFs, between the measured and calculated OFs for 6MV and 23MV are provided in Figure 3-11. These distributions include the ΔOFs for the square fields and rectangular fields defined by the collimator settings used for the blocked fields, without the blocks. Output factors for square and rectangular fields are expected to agree within ±1% and ±1.5%, respectively [Fra 98]. The distributions are slightly skewed towards the positive side indicating a tendency to

overestimate. The uncertainties in the percent deviations ranged from 0.0% to 0.1% with an average of approximately 0.0%. The performance of CMS and TMS are comparable for the square and rectangular fields on the central axis.

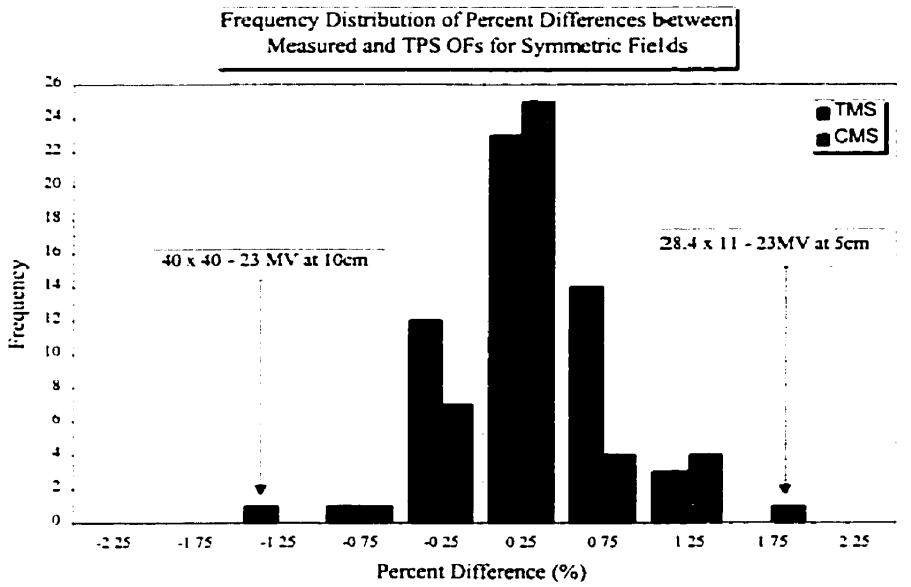

Figure 3-11: Frequency distributions of percent differences, ΔOF, between measured and calculated (TMS and CMS) OFs for the square fields and rectangular fields defined by the collimator settings used for the blocked fields, without the blocks, listed in Tables 2-1, and 2-2.

3.2.2 Independent Jaws

The results of the 6MV independent jaw output factors for the top half of the field, at three different depths, are illustrated in Figure 3-12 as a function of field size. A trend similar to square field data is observed. The output factors are increasing with increasing field size, and decreasing with increasing depth. The values calculated by both TMS and CMS-focus are in good agreement with the measured output factors. A complete set of plots of output factors at 6MV and 23MV for the field sizes listed in Table 2-1 are provided in Appendix B.

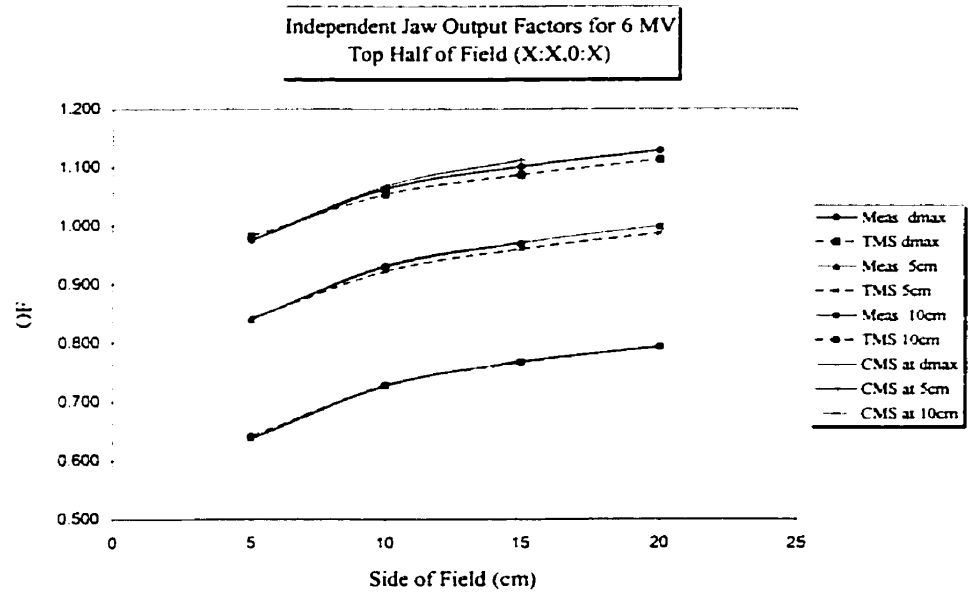

Figure 3-12. Output factors for 6MV asymmetric fields. The output is determined in-phantom relative to the output for a 10x10 field at dmax. Measurements were made on Siemens dual energy linear accelerator at the centre of the field. Calculations were performed on Helax TMS and CMS-focus.

Frequency distributions of the %deviations, ΔOFs, between measured and calculated OFs for all of the asymmetric fields listed in Table 2-1 are provided in Figure 3-13. The uncertainties in the percent deviations ranged from 0.1% to 0.2% with an average of approximately 0.1%. Both distributions are approximately symmetric around -0.75%. Thus, both of the treatment planning systems are more likely to underestimate the dose in an asymmetric field by a small amount.

Output factors for asymmetric fields are expected to agree within ±2% of measured output factors [Fra 98]. In general deviations of less than ±2% are achieved. The exceptions to this are: for TMS, the 6MV output factor for the field (0:20 x 0:20) at dmax; and for CMS, 23MV output factors for the field (0:5 x 0:5) at 5cm and 10cm. The HSF predicted by TMS for 6MV (0:5 x 0:5) was also underestimating the measured HSF by −1.5%. Thus a significant portion of the uncertainty found in the output factor is due

to an underestimation of the head scatter. The performance of CMS and TMS, as illustrated in these distributions, is comparable.

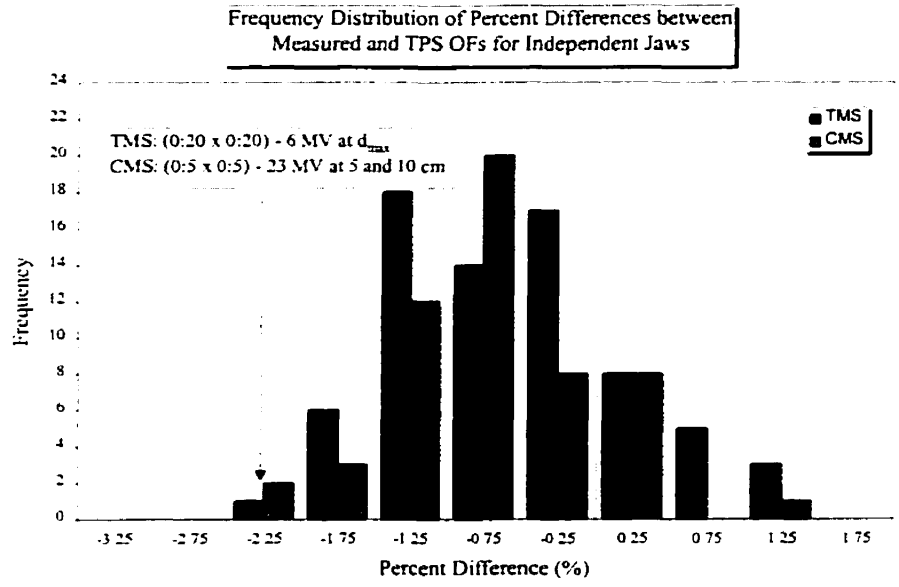

Figure 3-13: Frequency distributions of percent differences, ΔOF, between measured and calculated (TMS and CMS) OFs for the asymmetric fields listed in Table 2-1.

The output factors for 23MV photons for asymmetric fields do not decrease as a function of field size; a trend that was observed in HSF measurements. This suggests that brass build-up caps inaccurately measure HSFs for independent jaws.

3.2.3 MLC

The results of the measured and calculated (CMS and TMS) 6MV and 23MV output factors for MLC pattern 3 (figure 2-2) are illustrated in Figure 3-14 as a function of depth in water. The output factors, both calculated and measured, are decreasing with increasing depth in the water phantom as expected due to the increased attenuation with depth. Furthermore, the output factors at depths of 5 and 10cm are larger for 23MV than the 6MV beam. This is due to the increased penetration of a higher energy beam. The values calculated by both Helax-TMS and CMS-Focus are in good agreement with the

measured output factors. Similar plots for the remaining MLC patterns illustrated in figures 2-3 through 2-9 are provided in Appendix B.

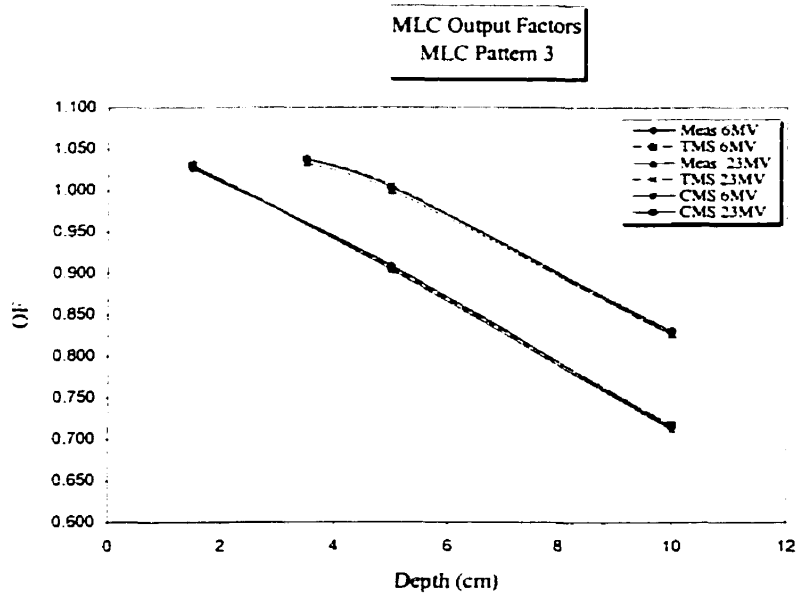

Figure 3-14: Relative output data for 6MV and 23 MV MLC field (pattern 3). The output is determined in-phantom relative to the output for a 10x10 field at dmax. Measurements were made on Siemens dual energy linear accelerator at the centre of the field. Calculations were performed on Helax TMS and CMS-focus.

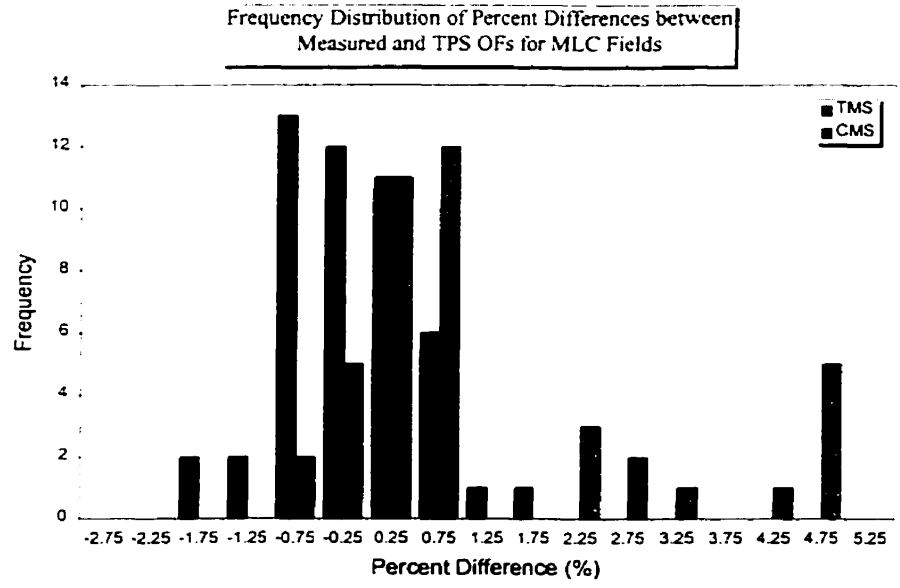

Figure 3-15: Frequency distributions of percent differences, ΔOF, between measured and calculated (TMS and CMS) OFs for all MLC fields listed in Table 2-1.

Frequency distributions of the percent deviations, ΔOFs, between measured and calculated (TMS and CMS) OFs for all of the MLC fields listed in Table 2-1 are provided in Figure 3-15. The uncertainties in the percent deviations ranged from 0.0% to 0.1%, with an average of approximately 0.1%. Output factors for MLC fields are expected to agree within ±2% of measured output factors [Fra 98]. The TMS distribution is roughly centered about zero with a maximum deviation of ±2%.

The CMS distribution exhibits several outliers in the range of +2% to +5%, listed in Table 3-1. Since the Siemens MLC replaces the lower jaw of the linac, blocking patterns designed using MLC reduce the head scatter fluence. This reduction is not accounted by CMS since it does not model head scatter. A head scatter factor for the corresponding rectangular field is used thereby overestimating the output factor. The amount by which CMS overestimates the OF depends upon the degree of obstruction of calculation point's eye view of the flattening filter. Therefore, these outliers are a result of a change in head scatter between the blocks and MLC, not modeled in CMS. Specifically, all of the outliers are due to 6MV and 23MV output factors for patterns 5 and 8. Patterns 5 and 8 are illustrated in figures 2-4 and 2-6, respectively.

Table 3-1: ΔOFs for the outliers (ΔOF>2%) in the CMS distribution of MLC fields

Energy (MV)	Pattern	Depth (cm)	*ΔOF*	±
6	8	5	2.2	0.1
6	**8**	**10**	**2.3**	**0.1**
6	8	1.5	2.5	0.0
6	**5**	**10**	**2.6**	**0.1**
6	5	5	2.6	0.1
6	**5**	**1.5**	**3.1**	**0.0**
23	8	3.5	4.4	0.1
23	**8**	**5**	**4.6**	**0.1**
23	8	10	4.9	0.1
23	**5**	**10**	**4.9**	**0.1**
23	5	3.5	4.9	0.0
23	**5**	**5**	**4.9**	**0.0**

Since the same field shape would produce the same phantom scatter, the difference in output factors between the MLC and blocked fields is due to the change in head scatter, on a first order approximation, and the presence of the tray. Output factors for the blocked fields were corrected for the attenuation in the tray as follows,

3.1 $$OF_{No\_tray} = \frac{OF_{tray}}{TF}$$

where OF_{tray} is the measured output factor with the tray in place, OF_{No_tray} is the output factor corrected for the attenuation in the tray, and TF is the tray factor, equal to 0.98 for 23MV photons and 0.968 for 6MV photons. Comparisons of the measured output factors for the same MLC and blocked fields (without the tray) were made and the results are given in Table 3-2 and Table 3-3 for 23MV and 6MV, respectively. The results are expressed as a local percent of the MLC output factors OF_{MLC}, ie.

3.2 $$\Delta OF_{MLC}^{BLK} = \frac{OF_{No\_tray}^{BLK} - OF_{MLC}}{OF_{MLC}} \cdot 100\%$$

where a negative value indicates that the output for the MLC field is greater than for the blocked field, and vice versa.

Table 3-2: ΔOF_{MLC}^{BLK} for 23MV MLC and Blocked Field OFs

Depth (cm)	Pattern	ΔOF_{MLC}^{BLK}	
10.0	Pat 3	0.2	0.1
5.0	Pat 3	0.5	0.1
3.5	Pat 3	1.1	0.1
10.0	**Pat 4**	**0.5**	**0.1**
5.0	**Pat 4**	**0.6**	**0.1**
3.5	**Pat 4**	**1.0**	**0.1**
10.0	Pat 5	1.9	0.1
5.0	Pat 5	2.2	0.1
3.5	Pat 5	2.8	0.1
10.0	**Pat 6**	**0.5**	**0.1**
5.0	**Pat 6**	**0.8**	**0.1**
3.5	**Pat 6**	**1.3**	**0.1**
10.0	Pat 7	0.5	0.1
5.0	Pat 7	0.7	0.1
3.5	Pat 7	1.4	0.1
10.0	**Pat 8**	**3.3**	**0.1**
5.0	**Pat 8**	**3.2**	**0.1**
3.5	**Pat 8**	**3.6**	**0.1**
10.0	Pat 9	2.4	0.1
5.0	Pat 9	2.7	0.1
3.5	Pat 9	3.0	0.1
10.0	**Pat 10**	**0.2**	**0.1**
5.0	**Pat 10**	**0.5**	**0.1**
3.5	Pat 10	1.1	0.1

Table 3-3: ΔOF_{MLC}^{BLK} for 6MV MLC and Blocked Field OFs

10.0	Pat 3	0.0	0.1
5.0	Pat 3	-0.1	0.1
1.5	Pat 3	0.7	0.1
10.0	**Pat 4**	**0.1**	**0.1**
5.0	**Pat 4**	**0.1**	**0.1**
1.5	**Pat 4**	**0.3**	**0.1**
10.0	Pat 5	1.4	0.1
5.0	Pat 5	1.3	0.1
1.5	Pat 5	2.2	0.1
10.0	**Pat 6**	**0.0**	**0.1**
5.0	**Pat 6**	**0.0**	**0.0**
1.5	**Pat 6**	**1.0**	**0.1**
10.0	Pat 7	0.2	0.1
5.0	Pat 7	0.1	0.0
1.5	Pat 7	1.5	0.1
10.0	**Pat 8**	**2.0**	**0.1**
5.0	**Pat 8**	**1.9**	**0.1**
1.5	**Pat 8**	**2.8**	**0.1**
10.0	Pat 9	1.7	0.1
5.0	Pat 9	2.0	0.1
1.5	Pat 9	3.2	0.1
10.0	**Pat 10**	**-0.1**	**0.1**
5.0	**Pat 10**	**-0.3**	**0.1**
1.5	**Pat 10**	**0.5**	**0.1**

Majority of the values of ΔOF_{MLC}^{BLK} are positive indicating that the output of MLC fields is smaller than the corresponding blocked fields due to reduced head scatter fluence. This coincides with the overestimation of the measured output factors observed in Figure 3-15 for MLC fields in CMS. From the values listed in Table 3-2 and Table 3-3, it is seen that the differences in head scatter for the blocked and MLC fields are most significant for patterns 5, 8 and 9. These results, except for pattern 9, support the idea that the outliers are due to changes in head scatter with the MLC versus blocked fields for the same patterns, which is not explicitly modeled in CMS. Since the field size in pattern 9

exceeds the maximum allowable field size in CMS, the MLC and blocked output factors for these fields were not calculated in CMS. To confirm that the differences in MLC and blocked output factors are a result of changes in head scatter, comparisons of MLC and blocked HSFs were made. These are provided in Table 3-4 and Table 3-5 for 23MV and 6MV, respectively. ΔHSF_{MLC}^{BLK} was determined by the same method as used for output factors.

Table 3-4: ΔHSF_{MLC}^{BLK} for 23MV MLC and Blocked Field HSFs

Pattern	ΔHSF	
Pat 3	0.9	0.5
Pat 4	**0.2**	**0.5**
Pat 5	2.2	0.5
Pat 6	**1.2**	**0.5**
Pat 7	0.9	0.5
Pat 8	**2.3**	**0.5**
Pat 9	2.7	0.5
Pat 10	**0.2**	**0.5**

Table 3-5: ΔHSF_{MLC}^{BLK} for 6MV MLC and Blocked Field HSFs

	ΔHSF	
Pat 3	0.8	0.7
Pat 4	**0.8**	**0.7**
Pat 5	2.2	0.7
Pat 6	**0.9**	**0.7**
Pat 7	1.2	0.6
Pat 8	**2.6**	**0.6**
Pat 9	2.4	0.7
Pat 10	**0.6**	**0.6**

Similar results to ΔOF_{MLC}^{BLK} are observed; the values of ΔHSF_{MLC}^{BLK} are all positive and larger in magnitude for patterns 5, 8, and 9. Therefore the outliers in Figure 3-15 for CMS are caused by a reduction in head scatter fluence in MLC field which is not modeled in CMS.

3.2.4 Blocks

Results of the measured and calculated (TMS and CMS) output factors for block field pattern 3 are illustrated in Figure 3-16 as a function of depth in water. The trend in output factors with depth and energy is similar to that observed for MLC output factors in Figure 3-14. The output factors calculated by CMS and TMS are in good agreement with

the measured output factors. Similar plots of the measured and calculated blocked field output factors for patterns 4 through 10 are provided in Appendix B.

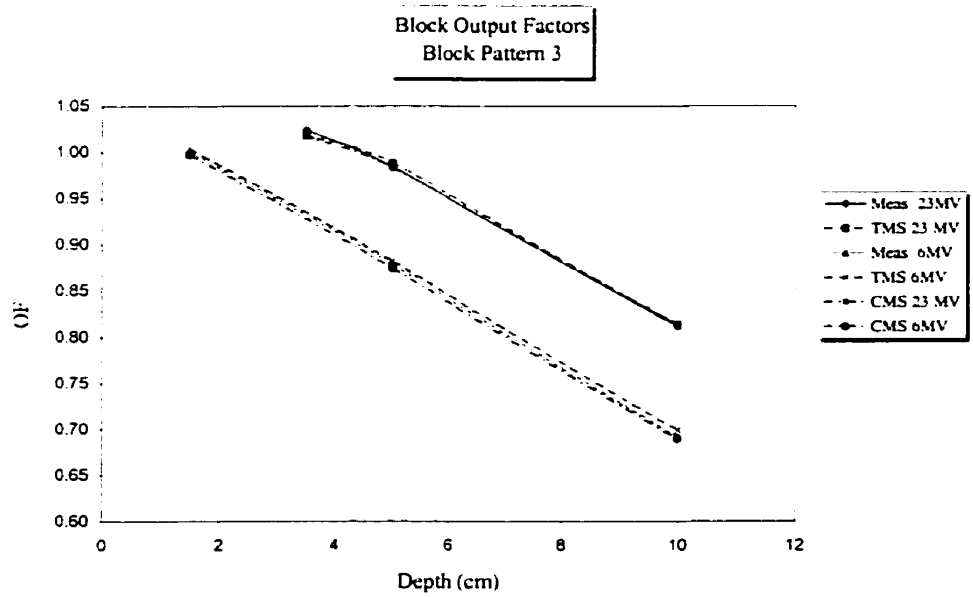

Figure 3-16: Output factors for 6MV and 23 MV blocked field pattern 3. The output is determined in-phantom relative to the output for a 10x10 field at dmax. Measurements were made on Siemens dual energy linear accelerator at the centre of the field. Calculations were performed on Helax TMS and CMS-focus.

Figure 3-17 is a frequency distribution of the percent differences, ΔOFs, between the measured and calculated output factors for the blocked fields listed in Table 2-1. The uncertainties in ΔOF range from 0.0% to 0.1% with an average uncertainty of 0.1%. Both the TMS and CMS distributions are approximately centered about zero. TPS calculated OFs for blocked fields are expected to agree within ±2% of measured OFs [Fra 98]. The exceptions to this are: for CMS, the 23MV blocked field output for pattern 5 at all three depths; and for TMS, the 23MV blocked field output for pattern 8 at dmax.

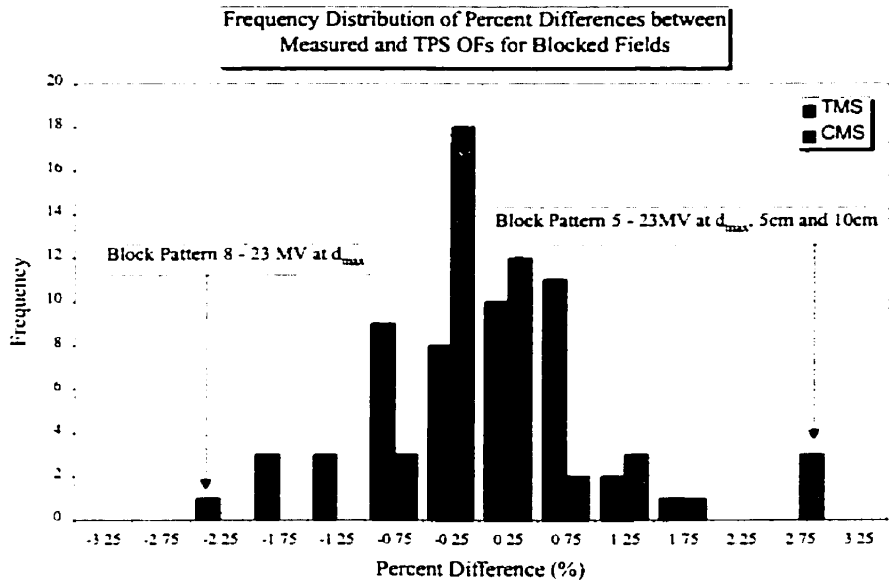

Figure 3-17: Frequency distributions of percent differences, ΔOF, between measured and calculated (TMS and CMS) OFs for all blocked fields listed in Table 2-1.

Although it is not clear why CMS overestimates block pattern 5, a few possible reasons are noted below. Firstly, the important feature of patterns 5, 8 and 9, is that the blocks may hide the flattening filter, even further than the corresponding collimator jaws, from the view of the calculation point. This would result in a reduction in the head scattered dose. Secondly, the blocks may cause increased scatter back into the monitor chamber thereby increasing the chamber reading. The result is less dose is delivered than expected. Thirdly, CMS does not account for the negligible scatter produced in the blocks. Since the blocks increase the head scatter and therefore the measured output, it is expected that CMS will underestimate the dose. Therefore, various competing, yet small, changes in head scatter are occurring due to the blocks. It is difficult to assess these factors without further experimentation or Monte Carlo calculations.

By comparing the measured in-air output for the blocked fields to that for the fields defined by the corresponding collimator settings used in the blocked fields, but with the blocks removed, change in head scatter due to the presence of the block can be determined. The blocked field head scatter factors are corrected for attenuation in the tray as discussed in the section above, equation 3.1 for output factors. These corrected blocked head scatter factors, $HSF^{BLK}_{No\_tray}$, are then compared with the collimated field head scatter factors, HSF_{Col}, by calculating a local percent of the collimated HSFs, ie.

$$\Delta HSF^{BLK}_{Col} = \frac{HSF^{BLK}_{No\_tray} - HSF_{Col}}{HSF_{Col}} \cdot 100\%. \qquad 3.3$$

The results of this comparison are given in Table 3-6 and Table 3-7 for 23MV and 6MV, respectively.

Table 3-6: ΔHSF^{BLK}_{Col} for 23MV blocked and collimated HSFs

Pattern	(X x Y)	ΔHSF^{BLK}_{Col}	
Pat 3	15 x 15	0.6	0.5
Pat 4	**5.4x2.8:3.0**	**0.1**	**0.5**
Pat 5	28.4 x 11	0.4	0.5
Pat 6	**20x20**	**0.7**	**0.5**
Pat 7	26.4 x 19	0.7	0.4
Pat 8	**5.2:3.9 x 27**	**0.4**	**0.4**
Pat 9	39 x 27	-0.2	0.4
Pat 10	**10x10**	**0.1**	**0.3**

Table 3-7: ΔHSF^{BLK}_{Col} for 6MV blocked and collimated HSFs

Pattern	(X x Y)	ΔHSF^{BLK}_{Col}	
Pat 3	15 x 15	0.5	0.6
Pat 4	**5.4x2.8:3.0**	**0.1**	**0.6**
Pat 5	28.4 x 11	0.2	0.6
Pat 6	**20x20**	**0.6**	**0.6**
Pat 7	26.4 x 19	0.8	0.6
Pat 8	**5.2:3.9 x 27**	**0.3**	**0.6**
Pat 9	39 x 27	-0.5	0.6
Pat 10	**10x10**	**0.3**	**0.4**

Positive ΔHSF^{BLK}_{Col} values imply that the blocked field output in-air is greater than that for the collimated, unblocked field, and vice versa for the negative values. These values indicate that only pattern 9 intrudes into the view of the flattening filter thereby reducing the head scatter by an amount which is concealed by the experimental uncertainty. The remaining values are slightly greater than zero indicating the blocks do

not intrude into the view of the flattening filter but increase the head scatter due to the scatter produced in the blocks. Although, none of these results are larger than the experimental error reported. The difficulty observed with CMS for pattern 5 may be a result of performing the scatter integral for a narrow field. Similar errors are also observed, although up to a lesser extent, for the narrow field in pattern 8.

3.2.4.1 Comparison of Measured Blocks and Collimator OFs

A comparison of the blocked and unblocked output factors was made by the same method described for HSFs. The results are provided in Table 3-8 and Table 3-9 for 23MV and 6MV, respectively.

Table 3-8: ΔOF_{Col}^{BLK} for 23MV blocked and collimated field OFs

Pattern	Depth (cm)	(X x Y)	ΔOF_{Col}^{BLK}	
Pat 3	10	15 x 15	-0.1	0.1
Pat 3	5	15 x 15	0.2	0.1
Pat 3	3.5	15 x 15	0.6	0.1
Pat 4	**10**	**5.4x2.8:3.0**	**-0.8**	**0.1**
Pat 4	**5**	**5.4x2.8:3.0**	**-0.5**	**0.1**
Pat 4	**3.5**	**5.4x2.8:3.0**	**-0.4**	**0.1**
Pat 5	10	28.4 x 11	-3.1	0.1
Pat 5	5	28.4 x 11	-1.7	0.1
Pat 5	3.5	28.4 x 11	-1.8	0.1
Pat 6	**10**	**20x20**	**-0.1**	**0.1**
Pat 6	**5**	**20x20**	**0.4**	**0.1**
Pat 6	**3.5**	**20x20**	**0.6**	**0.1**
Pat 7	10	26.4 x 19	-0.4	0.1
Pat 7	5	26.4 x 19	0.0	0.1
Pat 7	3.5	26.4 x 19	0.4	0.1
Pat 8	**10**	**5.2:3.9 x 27**	**-2.8**	**0.1**
Pat 8	**5**	**5.2:3.9 x 27**	**-1.7**	**0.1**
Pat 8	**3.5**	**5.2:3.9 x 27**	**-1.7**	**0.1**
Pat 9	10	39 x 27	-4.5	0.1
Pat 9	5	39 x 27	-2.8	0.1
Pat 9	3.5	39 x 27	-3.3	0.1
Pat 10	**10**	**10x10**	**-0.4**	**0.1**
Pat 10	**5**	**10x10**	**0.0**	**0.1**
Pat 10	**3.5**	**10x10**	**0.2**	**0.0**

Table 3-9: ΔOF_{Col}^{BLK} for 6MV blocked and collimated OFs

			ΔOF_{Col}^{BLK}	
Pat 3	10	15 x 15	-0.4	0.1
Pat 3	5	15 x 15	-0.1	0.1
Pat 3	1.5	15 x 15	0.2	0.1
Pat 4	**10**	**5.4x2.8:3.0**	**-0.9**	**0.1**
Pat 4	**5**	**5.4x2.8:3.0**	**-0.7**	**0.1**
Pat 4	**1.5**	**5.4x2.8:3.0**	**-0.3**	**0.1**
Pat 5	10	28.4 x 11	-5.9	0.1
Pat 5	5	28.4 x 11	-3.1	0.0
Pat 5	1.5	28.4 x 11	-1.5	0.1
Pat 6	**10**	**20x20**	**-0.5**	**0.1**
Pat 6	**5**	**20x20**	**-0.2**	**0.0**
Pat 6	**1.5**	**20x20**	**0.4**	**0.1**
Pat 7	10	26.4 x 19	-1.4	0.1
Pat 7	5	26.4 x 19	-0.5	0.0
Pat 7	1.5	26.4 x 19	0.2	0.1
Pat 8	**10**	**5.2:3.9 x 27**	**-5.0**	**0.1**
Pat 8	**5**	**5.2:3.9 x 27**	**-2.7**	**0.1**
Pat 8	**1.5**	**5.2:3.9 x 27**	**-1.4**	**0.1**
Pat 9	10	39 x 27	-8.1	0.1
Pat 9	5	39 x 27	-4.8	0.0
Pat 9	1.5	39 x 27	-2.7	0.1
Pat 10	**10**	**10x10**	**-1.0**	**0.1**
Pat 10	**5**	**10x10**	**-0.6**	**0.1**
Pat 10	**1.5**	**10x10**	**0.0**	**0.0**

The values of ΔOF_{Col}^{BLK} are representative of the changes in head scatter (shown to be insignificant above) and phantom scatter. In particular, patterns 5, 8 and 9 demonstrate

the largest changes in phantom scatter due to the presence of the blocks. Recall that pattern 9 was not calculated in CMS due to the large collimator field size. The values of ΔOF_{Col}^{BLK}, are in general greater in magnitude for the 6MV output factors than for the 23MV output factors. This is due to increased scattering associated with lower energy photons.

3.2.5 Virtual Wedges

Tables of the measured and calculated virtual wedge output factors for fields listed in Table 2-2, are provided in Appendix A. The results of the comparisons between the measured and calculated (TMS and CMS) output factors are illustrated in frequency distributions. Figure 3-18, Figure 3-19, Figure 3-20, and Figure 3-21 are frequency distributions of ΔOF for virtual wedge angles of 15°, 30°, 45°, and 60°, respectively. There is no reported criteria for external beam dose calculations with virtual wedges as found for the MLC, blocks, and asymmetric fields. However, since these output factors are measured with virtual wedges in asymmetric fields, for which the expected agreement is ±2%, the same criteria was assumed for the virtual wedge data.

For the 15° virtual wedge OFs, Figure 3-18, the TMS distribution is essentially centred about zero, with few points outside the ±2% region. In particular, the points lying outside ±2% are listed in Table 3-10.

Table 3-10: ΔOF values (> ±2%) of measured and TMS OFs for 15° Virtual Wedge

6	1.5	0:20 x 0:20	-2.9	0.1
6	**10**	**5:5 x 0:5**	**2.2**	**0.2**

The larger deviation of –2.9% observed for the larger field size at dmax, is similar to the deviation of –2.4% observed for the exact same field in the absence of the virtual wedge.

The CMS distribution, Figure 3-18, indicates that the calculations are, in general, underestimating the measured output for these fields. CMS does not explicitly account for head scatter and its modulation due to the virtual wedge. The ΔOF values lying outside ±2% are listed in Table 3-11.

Table 3-11: ΔOF values (> ±2%) of measured and CMS OFs for 15° Virtual Wedge

Energy (MV)	*Depth (cm)*	*Field*	*ΔOF*	±
23	3.5	0:5 x 0:5	-3.3	0.1
23	**5**	**0:5 x 0:5**	**-3.4**	**0.1**
23	10	0:5 x 0:5	-3.4	0.1
23	**3.5**	**0:10 x 0:10**	**-3.4**	**0.1**
23	5	0:10 x 0:10	-3.3	0.1
23	**10**	**0:10 x 0:10**	**-2.9**	**0.1**
23	3.5	10:10 x 0:10	-2.2	0.1
23	**5**	**10:10 x 0:10**	**-2.6**	**0.1**
23	10	10:10 x 0:10	-2.4	0.1
23	**3.5**	**5:5 x 0:5**	**-2.3**	**0.1**
23	5	5:5 x 0:5	-2.0	0.1
23	**10**	**5:5 x 0:5**	**-2.0**	**0.1**
6	1.5	0:5 x 0:5	-2.3	0.1
6	**5**	**0:5 x 0:5**	**-2.0**	**0.1**
6	10	0:5 x 0:5	-2.0	0.2

All of the values listed in Table 3-11 are for the right quadrant or the top half of the field. In addition, the more significant values are all for 23MV photons. The ΔOF values observed for the open asymmetric fields alone were, in general, less than 2% in magnitude (no virtual wedge), with the exception of the second and third entries. This indicates that a significant portion of the uncertainty is due to the virtual wedge.

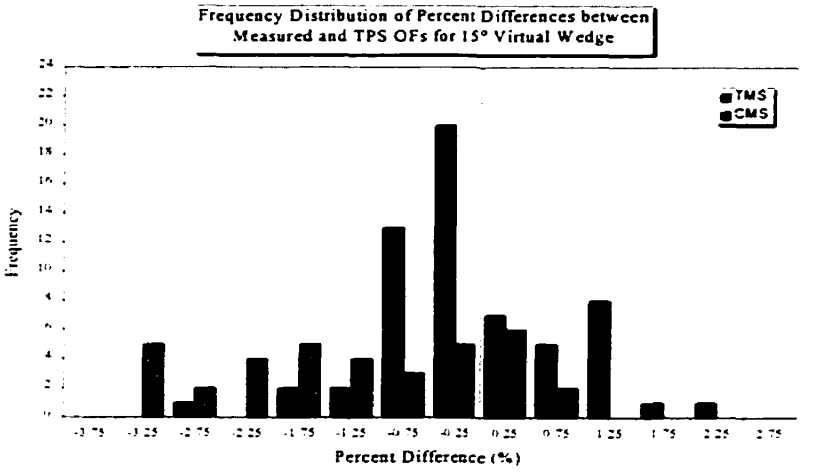

Figure 3-18: Frequency distributions of percent differences, ΔOF, between measured and calculated (TMS and CMS) 15° virtual wedge OFs for fields listed in Table 2-2.

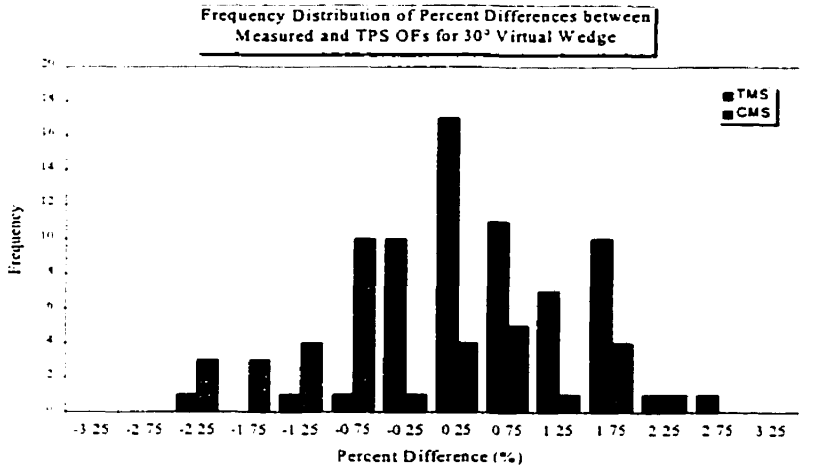

Figure 3-19: Frequency distributions of percent differences, ΔOF, between measured and calculated (TMS and CMS) 30° virtual wedge OFs for fields listed in Table 2-2.

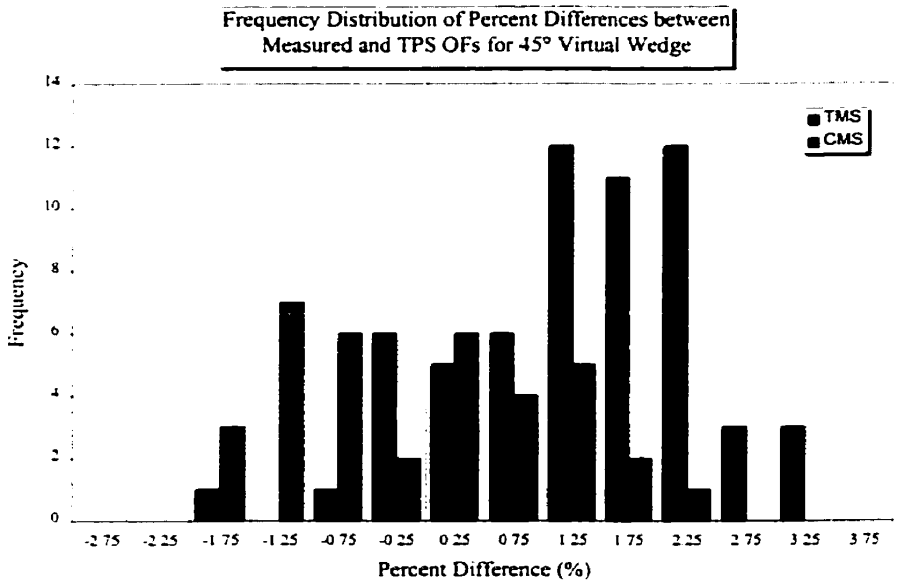

Figure 3-20: Frequency distributions of percent differences, ΔOF, between measured and calculated (TMS and CMS) 45° virtual wedge OFs for fields listed in Table 2-2.

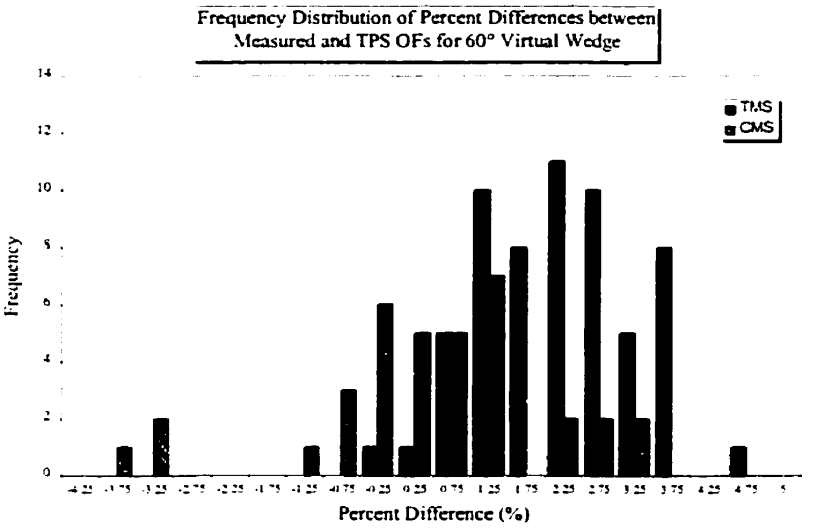

Figure 3-21: Frequency distributions of percent differences, ΔOF, between measured and calculated (TMS and CMS) 60° virtual wedge OFs for fields listed in Table 2-2.

The TMS ΔOF values for the 30° VW, illustrated in Figure 3-19, greater than ±2% are listed in Table 3-12. These fields are the same ones which produced ΔOF values >±2% for the 15° VW. Note the change in sign for the 6MV 0:20 x 0:20 field observed at dmax and 10cm. This is a result of off-axis softening. There is an underprediction near dmax due to the increased scatter produced by the softer beam, which is not accounted for in TMS. In addition, the softer beam produces a steeper depth dose curve thereby resulting in an overestimation of the dose at larger depths.

Table 3-12: ΔOF values (> ±2%) of measured and TMS OFs for 30° Virtual Wedge

Energy (MV)	Depth (cm)			
6	1.5	0:20 x 0:20	-2.1	0.1
6	**10**	**0:20 x 0:20**	**2.3**	**0.2**
6	10	5:5 x 0:5	2.6	0.2

The 30° VW CMS distribution in Figure 3-19 is more centered about zero, in comparison with the 15° VW distribution, with few values lying outside ±2%, see Table 3-13.

Table 3-13: ΔOF values (> ±2%) of measured and CMS OFs for 30° Virtual Wedge

Energy (MV)	Depth (cm)			
23	3.5	0:10 x 0:10	-2.1	0.1
23	**5**	**0:10 x 0:10**	**-2.1**	**0.1**
23	5	0:5 x 0:5	-2.0	0.1
23	**10**	**0:5 x 0:5**	**-2.0**	**0.2**
6	10	10:10 x 0:10	2.1	0.2

None of these values are significantly greater in magnitude than 2%.

For the 45° ΔOF values, illustrated in Figure 3-20, the TMS distribution is slightly overestimating the measured output, similar to the observation made for the 30° virtual wedge results. The ΔOF values greater than ±2% are listed in Table 3-14.

Table 3-14: ΔOF values (> ±2%) of measured and TMS OFs for 45° Virtual Wedge

Energy (MV)	*Depth (cm)*	*Field*	*ΔOF*	±
23	5	15:15 x 0:15	2.0	0.1
23	**10**	**5:5 x 0:5**	**2.0**	**0.2**
23	5	0:10 x 10:10	2.1	0.1
23	**10**	**0:10 x 10:10**	**2.1**	**0.1**
23	5	20:20 x 0:20	2.2	0.2
6	**10**	**20:20 x 0:20**	**2.1**	**0.2**
6	10	10:10 x 0:10	2.1	0.2
6	**10**	**15:15 x 0:15**	**2.1**	**0.2**
6	10	0:10 x 0:10	2.2	0.2
6	**1.5**	**5:5 x 0:5**	**2.2**	**0.1**
6	5	5:5 x 0:5	2.3	0.2
6	**10**	**5:5 x 0:5**	**3.0**	**0.2**
6	10	0:15 x 0:15	2.4	0.2
6	**10**	**0:20 x 0:20**	**2.8**	**0.2**
23	5	0:15 x 0:15	2.7	0.2
23	**10**	**0:15 x 0:15**	**3.1**	**0.2**
23	5	0:20 x 0:20	2.7	0.2
23	**10**	**0:20 x 0:20**	**3.1**	**0.2**

The 45° VW CMS distribution in Figure 3-20 is essentially distributed about zero with significantly fewer points outside ±2%, see Table 3-15, then observed in the 45° VW TMS distribution.

Table 3-15: ΔOF values (> ±2%) of measured and CMS OFs for 45° Virtual Wedge

Energy (MV)	*Depth (cm)*	*Field*	*% Deviation*	±
6	5	5:5 x 0:5	2.1	0.2

The ΔOF values for the 60° VW distribution, illustrated in Figure 3-21, indicate that both CMS and TMS are, in general, overestimating the measured output. The values of ΔOF exceeding ±2% are listed in Table 3-16 and Table 3-17 for TMS and CMS respectively.

Table 3-16: ΔOF values (> ±2%) of measured and TMS OFs for 60° Virtual Wedge

Energy (MV)	*Depth (cm)*	*Field*	*ΔOF*	*σ*
23	5	0:10 x 0:10	2.0	0.2
23	**10**	**0:10 x 0:10**	**2.2**	**0.2**
23	10	0:5 x 5:5	2.1	0.1
23	**3.5**	**0:5 x 5:5**	**2.1**	**0.1**
23	5	10:10 x 0:10	2.5	0.2
23	**10**	**10:10 x 0:10**	**2.2**	**0.2**
23	3.5	15:15 x 0:15	2.2	0.2
23	**5**	**15:15 x 0:15**	**2.9**	**0.2**
23	10	15:15 x 0:15	3.0	0.2
23	**3.5**	**20:20 x 0:20**	**2.3**	**0.2**
23	5	20:20 x 0:20	3.2	0.2
23	**10**	**20:20 x 0:20**	**2.5**	**0.3**
23	3.5	5:5 x 0:5	2.2	0.1
23	**5**	**5:5 x 0:5**	**2.3**	**0.1**
23	10	5:5 x 0:5	2.3	0.1
23	**3.5**	**0:20 x 0:20**	**2.5**	**0.2**
23	5	0:20 x 0:20	3.6	0.2
23	**10**	**0:20 x 0:20**	**4.6**	**0.3**
23	3.5	0:10 x 10:10	3.4	0.1
23	**5**	**0:10 x 10:10**	**3.5**	**0.1**
23	10	0:10 x 10:10	3.7	0.1
23	**3.5**	**0:15 x 0:15**	**2.6**	**0.2**
23	5	0:15 x 0:15	3.5	0.2
23	**10**	**0:15 x 0:15**	**3.9**	**0.2**
6	10	0:10 x 10:10	2.6	0.2
6	**5**	**20:20 x 0:20**	**2.5**	**0.3**
6	10	20:20 x 0:20	3.6	0.4
6	**10**	**0:10 x 0:10**	**2.6**	**0.3**
6	10	10:10 x 0:10	2.9	0.3
6	**1.5**	**5:5 x 0:5**	**3.0**	**0.2**
6	5	5:5 x 0:5	3.1	0.2
6	**10**	**5:5 x 0:5**	**3.8**	**0.2**
6	10	0:15 x 0:15	3.1	0.3
6	**10**	**15:15 x 0:15**	**3.1**	**0.3**
6	10	0:20 x 0:20	3.6	0.4

Table 3-17: ΔOF values (> ±2%) of measured and CMS OFs for 60° Virtual Wedge

Energy (MV)	*Depth (cm)*	*Field*	*ΔOF*	*σ*
6	10	0:10 x 10:10	-3.6	0.1
6	**5**	**0:10 x 10:10**	**-3.4**	**0.1**
6	1.5	0:10 x 10:10	-3.4	0.1
6	**1.5**	**10:10 x 0:10**	**2.1**	**0.2**
6	5	10:10 x 0:10	2.4	0.2
6	**10**	**10:10 x 0:10**	**2.6**	**0.3**
6	1.5	5:5 x 0:5	2.5	0.2
6	**5**	**5:5 x 0:5**	**3.2**	**0.2**
6	10	5:5 x 0:5	3.1	0.2

There are several explanations for the deviations observed for TMS calculated virtual wedge output factors. Two of these reasons are the lateral phantom scatter

gradient, and off-axis softening. It has been previously shown that TMS overestimates the central axis wedge factor data by > 2% for large angle wedges. The only explanations of this are that the lateral phantom scattered gradient is not accurately accounted for by TMS or improper modeling of the dynamic modulation. For off-axis measurements, there are additional uncertainties due to off axis softening. TMS uses the PDDs for the central axis, while the measurements are taken at the middle of the field. In general, it is seen for TMS that the deviation between the measured and calculated values increases with increasing wedge angle.

CMS data is force fitted by using a physical wedge of arbitrary thickness variation and attenuation coefficients for a few fields. This is an empirical fit and there is no certainty as to whether or not it will work for all field sizes.

3.3 Isodose Distribution

Detailed results of the evaluation of the isodose distributions described in section 2.1.3, are provided in Appendix B.

3.3.1 Low gradient Central Beam Region

The maximum deviations observed between any set of measured and calculated isodose lines on the centre of the field were recorded and expressed as a local percent, ΔL, of the measured % isodose value. The results, provided in Appendix A, are displayed in a frequency distribution in Figure 3-22. External beam dose calculations are expected to agree within ±2% of the measured dose at the centre of the field [Fra 98]. This criteria is clearly satisfied by both TMS and CMS. In addition, both the TMS and CMS frequency distributions are centered about zero.

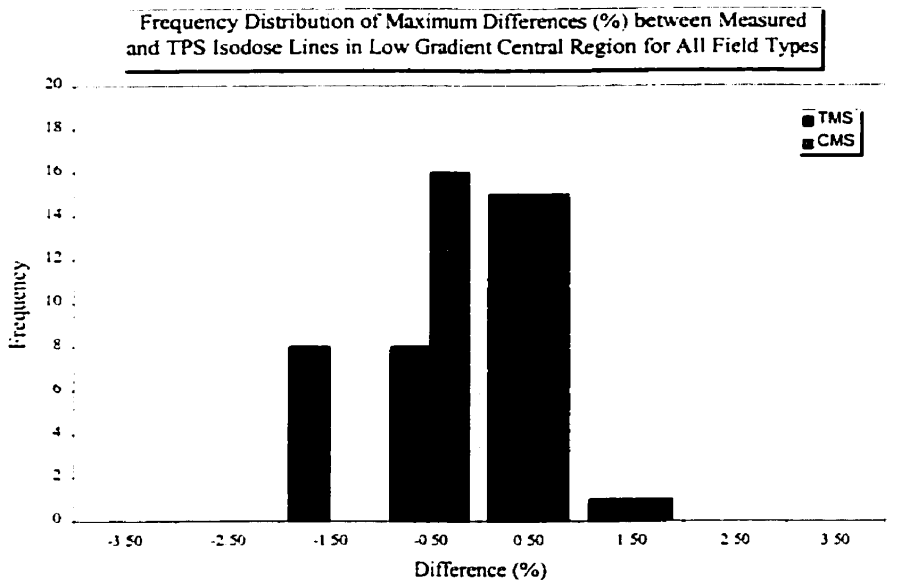

Figure 3-22: Frequency distributions of local percent ΔL of the maximum deviation observed between any set of measured and calculated (CMS and TMS) isodose lines in the low gradient central beam region for isodose distributions of the fields listed in Table 2-3 for 23MV and 6MV.

3.3.2 Low Gradient Inner beam Region

The maximum deviations observed, expressed as a local percent of the measured % isodose value, in the low gradient inner beam region of the isodose distributions for the fields listed in Table 2-3 are illustrated in a frequency distribution, Figure 3-23. This graph includes measurements from both sides of the field central axis. These distributions indicate that TMS is underestimating the measured dose in most cases while, CMS is overestimating in most. External photon beam dose calculations are expected to agree within ±3% of the measured dose in the low gradient inner beam region [Fra 98]. This criteria is satisfied by the CMS distribution, and almost entirely satisfied for the TMS distribution, with a few exceptions.

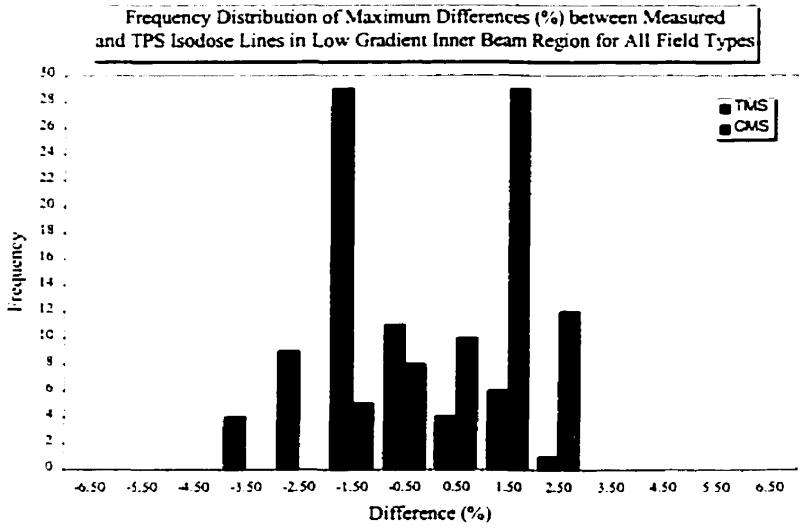

Figure 3-23: Frequency distributions of local percent ΔL of the maximum deviation observed between any set of measured and calculated (CMS and TMS) isodose lines in the low gradient inner beam region for isodose distributions of the fields listed in Table 2-3 for 23MV and 6MV.

Looking more closely, the values of $\Delta L > \pm 2\%$ are listed in Table 3-18 and Table 3-19 for TMS and CMS respectively. For TMS, majority of these deviations are

occurring at the 140% and 120% isodose lines which is nearing the build-up region and of little clinical significance. To evaluate the clinical significance of these errors, the next largest ΔL values were investigated, and it was found that they were all less than ±2%. The ΔL value of –3.0% at the 80% isodose line is particularly important from a clinical point of view since this is close to the 100% isodose line, to which the dose is normally prescribed. This value was in fact measured near the edge of the inner beam, approaching the higher gradient region. The value of this ΔL is strongly dependent on the analysts discretion, depending on where the distinction between high and low gradient is made. In addition to this, profiles were not measured beyond 10cm and this measurement is occurring below this. The next largest deviation is –1.6% at the 140% isodose line. Thus, the only value of clinical significance in Table 3-18 is (2.1 ± 0.3)%, occurring at the 100% isodose line for a 23MV beam with a blocked field, pattern 3.

Table 3-18: TMS ΔL values for the low gradient inner beam region

Energy	Field	Plane	Position	Isodose Line %	ΔL (%)	± (%)
6	15:5 x 10:10	cross	L	140	-3.9	0.3
6	5:15 x 10:10	in	R	140	-3.4	0.3
6	0:10 x 10:10	in	R	140	-3.1	0.3
6	0:10 x 10:10	[illegible]	[illegible]	[illegible]	[illegible]	[illegible]
6	5:15 x 10:10	cross	R	140	-3.0	0.3
6	5:15 x 10:10	in	L	140	-2.8	0.3
6	15:5 x 10:10	in	R	140	-2.8	0.3
6	10:0 x 10:10	in	R	140	-2.6	0.3
6	10:0 x 10:10	in	L	140	-2.5	0.3
6	15:5 x 10:10	in	L	140	-2.5	0.3
23	Block6	cross	L	120	-2.0	0.2
6	0:10 x 10:10	cross	L	140	-2.0	0.3
6	MLC6	cross	L	140	-2.0	0.3
23	Block6	[illegible]	[illegible]	[illegible]	[illegible]	[illegible]

A similar investigation was performed for the CMS ΔL values listed in Table 3-19. As for the TMS values, many of them are occurring at the 140% and 120% isodose lines. Some of these distributions, as identified by an asterisk * in Table 3-19, exhibited ΔL values greater than or equal to 2% at the 100% isodose lines in addition to the ΔL values at other isodose lines reported in Table 3-19. Thus the deviations in CMS, although appearing smaller in magnitude compared with those for TMS in the frequency distribution, are more significant than those observed with TMS at positions of greater clinical importance. Thus TMS performs better near the clinically significant isodose lines for the low gradient inner beam region of the isodose distributions of the fields listed in Table 2-3.

Table 3-19: CMS ΔL values for the low gradient inner beam region

Energy	Field	Plane	Position	Isodose Line %	ΔL (%)	± (%)
6	15:5 x 10:10	cross	R	100	2.0	0.4
6	0:10 x 10:10	in	L	140*	2.0	0.4
6	15:5 x 10:10	in	L	140	2.1	0.3
6	Block6	in	L	140	2.1	0.3
23	5:15 x 10:10	cross	L	100	2.1	0.2
6	5:15 x 10:10	in	L	140	2.3	0.3
23	10:0 x 10:10	cross	R	100	2.4	0.3
6	5:15 x 10:10	cross	L	120*	2.5	0.4
6	10:0 x 10:10	cross	R	120*	2.6	0.4
23	Block6	cross	R	120*	2.6	0.3
23	Block6	in	L	120*	2.8	0.3
23	15:5 x 10:10	cross	R	100	3.0	0.3

3.3.3 High Gradient Region

The maximum displacements in the high gradient (>30%/cm) region observed between sets of measured and calculated isodose curves are provided in Appendix A. In

addition, they are displayed in a frequency distribution in Figure 3-24. Negative values indicate the TPS has underestimated the dose in comparison to the measured dose, and positive values indicate an overestimation.

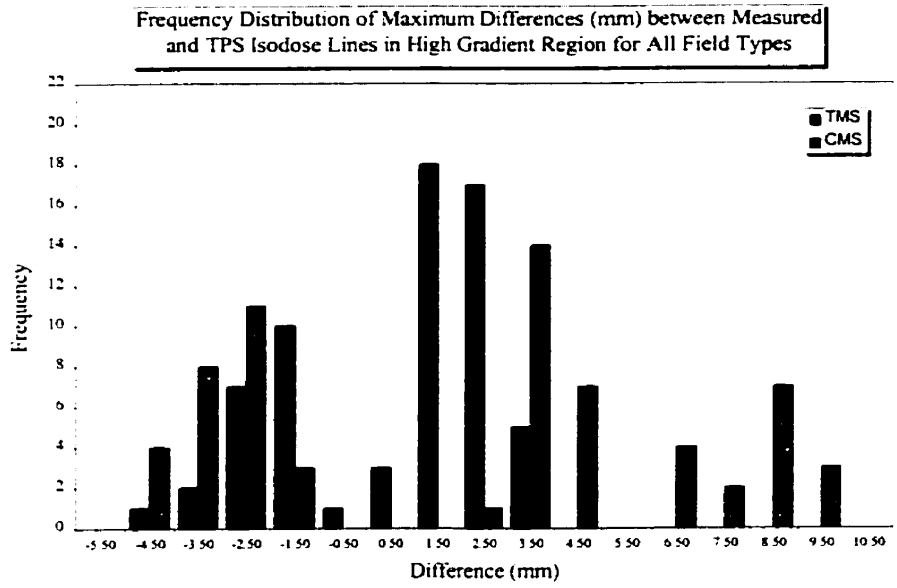

Figure 3-24: Frequency distributions of the maximum deviation observed between any set of measured and calculated (CMS and TMS) isodose lines in the high gradient (>30%/cm) region for isodose distributions of the fields listed in Table 2-3.

In 3D conformal therapy, treatment ports are designed with very tight margins to reduce the dose to nearby critical structures around the planning target volume. The prediction of dose in high gradient region is thus of utmost importance in gaining confidence in displayed doses by the TPS and designing suitable beam blocking and angular arrangements.

External photon beam dose calculations are expected to agree within ±4mm of the measured dose in the high gradient region [Van 93]. The values in the TMS distribution greater than 3mm are provided in Table 3-20. The maximum deviations for the MLC fields are all occurring for the 20% isodose curve, while for the blocks and asymmetric

fields, the deviations are occurring near the high dose regions, 100% to 140%. The deviations occurring for the 20% isodose curves are a result of errors in the transmission through the MLCs.

Table 3-20: Maximum Lateral Deviations (>3mm) determined from TMS calculated and measured isodose distributions.

Energy (MV)	Field	Plane	Position	Isodose Line %	Lateral Deviation (mm)	± (mm)
6	Block6	in	R	140	-4.3	0.7
23	**Block6**	**cross**	**R**	**120**	**-3.6**	**0.7**
6	5:15 x 10:10	cross	R	140	-3.4	0.7
6	**Block6**	**in**	**L**	**100**	**3.0**	**0.7**
6	Block6	cross	L	100	3.1	0.7
6	**MLC3**	**in**	**R**	**20**	**3.1**	**0.7**
6	MLC6	in	R	20	3.3	0.7
6	**15:5 x 10:10**	**cross**	**L**	**100**	**3.6**	**0.7**
23	MLC6	in	R	20	3.6	0.7

Similarly, the values in the CMS distribution greater than 3mm are provided in Table 3-21. The extreme outliers (>6,mm) seen in the CMS distribution are in the blocked and MLC shaped fields. In the current CMS database, MLC has not been commissioned. Therefore, the calculation of penumbra for MLC field is the same as that of blocks. It is clear that CMS is unable to reproduce low isodose lines outside the field edge. These are determined by the block transmission factors and the penumbra functions as described in section 1.2.1.1.2. In the current CMS implementation, only the collimator jaw transmission and penumbra functions have been implemented. The same procedure must be carried out for the MLC and blocks. This may reduce the observed deviations in the 20% isodose line of the blocks and MLC fields.

Table 3-21: Maximum Lateral Deviations (>3mm) determined from CMS calculated and measured isodose distributions.

Energy (MV)	Field	Plane	Position	Isodose Line %	Lateral Deviation (mm)	± (mm)
23	5:15 x 10:10	cross	R	20	3.4	0.7
23	5:15 x 10:10	cross	L	20	4.3	0.7
23	5:15 x 10:10	in	R	20	3.6	0.7
23	5:15 x 10:10	in	L	20	3.4	0.7
23	**0:10 x 10:10**	**cross**	**R**	**120**	**-3.6**	**0.7**
23	**0:10 x 10:10**	**cross**	**L**	**20**	**5.0**	**0.7**
23	**0:10 x 10:10**	**in**	**R**	**20**	**4.3**	**0.7**
23	**0:10 x 10:10**	**in**	**L**	**20**	**4.0**	**0.7**
23	10:0 x 10:10	cross	R	20	4.1	0.7
23	10:0 x 10:10	cross	L	100	-4.3	0.7
23	10:0 x 10:10	in	R	20	4.3	0.7
23	10:0 x 10:10	in	L	20	3.6	0.7
23	**15:5 x 10:10**	**cross**	**R**	**20**	**4.3**	**0.7**
23	**15:5 x 10:10**	**cross**	**L**	**100**	**-3.0**	**0.7**
23	**15:5 x 10:10**	**in**	**R**	**20**	**4.3**	**0.7**
23	**15:5 x 10:10**	**in**	**L**	**20**	**-3.1**	**0.7**
6	5:15 x 10:10	cross	L	20	3.6	0.7
6	5:15 x 10:10	in	R	20	3.1	0.7
6	**0:10 x 10:10**	**cross**	**R**	**140**	**-4.0**	**0.7**
6	**0:10 x 10:10**	**cross**	**L**	**20**	**3.6**	**0.7**
6	**0:10 x 10:10**	**in**	**R**	**20**	**3.5**	**0.7**
6	10:0 x 10:10	cross	R	20	3.3	0.7
6	10:0 x 10:10	cross	L	120	-3.1	0.7
6	10:0 x 10:10	in	R	20	3.4	0.7
6	**15:5 x 10:10**	**cross**	**R**	**20**	**3.9**	**0.7**
6	**15:5 x 10:10**	**in**	**R**	**20**	**3.1**	**0.7**
23	Block3	cross	R	20	10.0	0.7
23	Block3	cross	L	20	10.0	0.7
23	Block3	in	R	20	8.9	0.7
23	Block3	in	L	20	8.6	0.7
6	**Block6**	**cross**	**R**	**140**	**-4.3**	**0.7**
6	**Block6**	**cross**	**L**	**20**	**3.6**	**0.7**
6	**Block6**	**in**	**L**	**20**	**-3.6**	**0.7**
6	Block3	cross	R	20	7.0	0.7
6	Block3	cross	L	20	7.9	0.7
6	Block3	in	R	20	7.0	0.7
6	Block3	in	L	20	7.0	0.7
6	**MLC3**	**cross**	**R**	**20**	**8.9**	**0.7**
6	**MLC3**	**cross**	**L**	**20**	**8.6**	**0.7**
6	**MLC3**	**in**	**R**	**20**	**8.4**	**0.7**
6	**MLC3**	**in**	**L**	**20**	**6.9**	**0.7**
23	MLC3	cross	R	20	8.6	0.7
23	MLC3	cross	L	20	8.9	0.7
23	MLC3	in	R	20	9.1	0.7
23	MLC3	in	L	20	7.9	0.7
23	**MLC6**	**cross**	**R**	**20**	**-4.1**	**0.7**
23	**MLC6**	**cross**	**L**	**20**	**-3.1**	**0.7**
23	**MLC6**	**in**	**R**	**20**	**-3.1**	**0.7**
23	**MLC6**	**in**	**L**	**20**	**-3.1**	**0.7**

3.3.4 Penumbra

The penumbra results are provided in Appendix A for all fields listed in table 2-3. Figure 3-25 is a frequency distribution of the difference in penumbra from measured and calculated isodose distributions for these fields. Positive values indicate the penumbra of the TPS calculated isodose distribution is larger than the penumbra of the measured distribution, and vice versa for negative values.

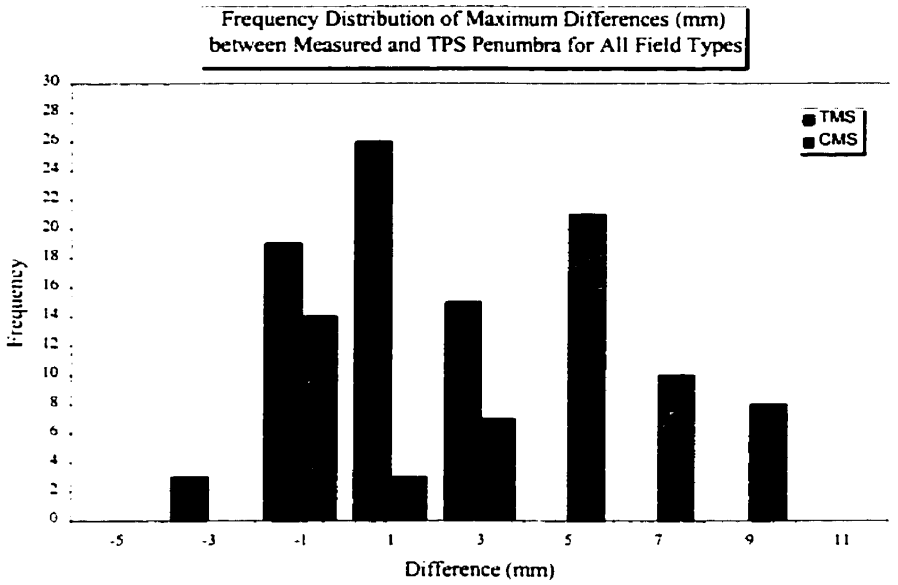

Figure 3-25: Frequency distribution of the difference between penumbras for measured and TPS calculated isodose distributions for all fields listed in Table 2-3. The penumbra was measured as the distance between the 80% and 20% isodose lines at the normalization depth (10cm).

The penumbra of a TPS calculated isodose distribution is expected to agree within ±2mm of the measured distribution [Fra 98]. The TMS distribution is centered about zero with a range of –3mm to +4mm. The values greater than ±2mm are listed in Table 3-22.

Table 3-22: Deviation (>±2mm) between penumbras of measured and TMS calculated isodose distributions.

Energy	Field	Plane	Position	Deviation (mm)	± (mm)
6	Block6	in	L	-3	1
6	**Block6**	**cross**	**L**	**-3**	**1**
23	15:5 x 10:10	in	R	3	1
23	**MLC6**	**in**	**R**	**3**	**1**
6	Block6	in	R	3	1
6	**MLC6**	**in**	**R**	**3**	**1**
23	MLC3	in	R	3	1
23	**Block6**	**in**	**R**	**3**	**1**
6	MLC3	in	R	4	1

With the exception of one asymmetric field, the remaining deviations greater than ±2mm are due to the MLC and blocks. In addition, it is noted that all, except one, of these deviations are for the in-plane (y-plane) and the MLC collimates the cross plane. Due to the large measurement uncertainty, these deviations could simply be a result of measurement errors.

The CMS distribution is much broader and shifted to the right indicating larger penumbras in their isodose distributions compared with the measured. The deviations greater than the expected agreement of ±2mm are provided in Table 3-23. It should be noted that the MLC and blocks are the source of the values in the bin labeled "9mm" and majority of the values in the bin labeled "7mm" as observed in the high gradient region. The explanation of this was discussed in the previous section for the high gradient region. TMS calculations in the penumbra and high gradient region are much more accurate than those performed by CMS in the same regions.

Table 3-23: Deviation (>±2mm) between penumbras of measured and CMS calculated isodose distributions.

Energy	Field	Plane	Position	Deviation (mm)	± (mm)
23	5:15 x 10:10	cross	R	6	1
23	5:15 x 10:10	cross	L	6	1
23	5:15 x 10:10	in	R	5	1
23	5:15 x 10:10	in	L	5	1
23	**0:10 x 10:10**	**cross**	**R**	**5**	**1**
23	**0:10 x 10:10**	**cross**	**L**	**6**	**1**
23	**0:10 x 10:10**	**in**	**R**	**6**	**1**
23	**0:10 x 10:10**	**in**	**L**	**6**	**1**
23	10:0 x 10:10	cross	R	6	1
23	10:0 x 10:10	cross	L	3	1
23	10:0 x 10:10	in	R	6	1
23	10:0 x 10:10	in	L	6	1
23	**15:5 x 10:10**	**cross**	**R**	**5**	**1**
23	**15:5 x 10:10**	**in**	**R**	**5**	**1**
23	**15:5 x 10:10**	**in**	**L**	**4**	**1**
6	5:15 x 10:10	cross	R	4	1
6	5:15 x 10:10	cross	L	5	1
6	5:15 x 10:10	in	R	3	1
6	**0:10 x 10:10**	**cross**	**R**	**5**	**1**
6	**0:10 x 10:10**	**cross**	**L**	**5**	**1**
6	**0:10 x 10:10**	**in**	**R**	**3**	**1**
6	**0:10 x 10:10**	**in**	**L**	**5**	**1**
6	10:0 x 10:10	cross	R	5	1
6	10:0 x 10:10	cross	L	4	1
6	10:0 x 10:10	in	R	4	1
6	10:0 x 10:10	in	L	3	1
6	**15:5 x 10:10**	**cross**	**R**	**5**	**1**
6	**15:5 x 10:10**	**cross**	**L**	**4**	**1**
6	**15:5 x 10:10**	**in**	**R**	**3**	**1**
23	Block3	cross	R	9	1
23	Block3	cross	L	9	1
23	Block3	in	R	9	1
23	Block3	in	L	9	1
6	**Block3**	**cross**	**R**	**8**	**1**
6	**Block3**	**cross**	**L**	**8**	**1**
6	**Block3**	**in**	**R**	**7**	**1**
6	**Block3**	**in**	**L**	**7**	**1**
6	MLC3	cross	R	6	1
6	MLC3	cross	L	6	1
6	MLC3	in	R	6	1
6	MLC3	in	L	6	1
23	**MLC3**	**cross**	**R**	**9**	**1**
23	**MLC3**	**cross**	**L**	**9**	**1**
23	**MLC3**	**in**	**R**	**8**	**1**
23	**MLC3**	**in**	**L**	**8**	**1**

4 Conclusion

In this study, the accuracy of photon beam dose calculations performed by Helax TMS and CMS-focus TPS was evaluated via comparison with measured dose. In particular, the accuracy of these calculations for asymmetric, MLC, block and virtual wedge fields was assessed. For TMS HSFs, the maximum percent deviation observed was (3.6 ± 0.3)%. In general, TMS performed well, within ±1%, for all fields, measured in-air, with the exception of the calculations for 23MV asymmetric fields. Output factors in phantom predicted by TMS and CMS were all within the expected agreement of ±2%. In general, for both TMS and CMS, calculated output factors for asymmetric fields were within the expected agreement of ±2%. The accuracy of CMS calculations of the output factors for MLC fields were found to be dependent on the field shape. In particular, since CMS-focus does not have an explicit head scatter model, the largest deviations, up to +5%, were observed for the fields in which the change in head scatter between the blocks and MLC was the greatest. TMS accurately (within ±2%) calculates the output factors for the MLC fields. Output factors calculated for the blocked fields exhibited an accuracy of <±2.5% for TMS, and <±2.9% for CMS.

The results for the virtual wedge output factor calculations were less accurate. In particular, for TMS, the calculations are more likely to overestimate the measured output with increasing wedge angle. Deviations as large as 4.6% were observed for the 60° virtual wedge. Although, no particular trends were observed for CMS calculated virtual wedge output factors, deviations as large as –3.6% were observed for CMS.

Finally, isodose distributions were measured, calculated and evaluated in several different regions. Dose distributions were accurately (within ±2%) calculated by both TMS and CMS in the low gradient central beam region. In the low gradient inner beam region the largest deviation of clinical significance observed on a TMS distribution was (2.1±0.3)%. Several deviations in the region of clinical significance (up to 3.0±0.3%) were observed with CMS calculated distributions in the inner beam region. In the high gradient region, TMS more accurately calculates the dose distribution than CMS, particularly for the blocked and MLC shaped fields. The maximum lateral displacement observed for the TMS calculated isodose distributions was (–4.3 ± 0.7)mm. For the CMS distributions lateral displacements as large as 10mm were observed for the blocked fields. These displacements in the distributions of the blocked and MLC shaped fields are almost always occurring at the 20% isodose line. This is due to the fact that transmission and penumbra functions for the blocks and MLC are not currently implemented at CCMB. Similar observations as noted in the high gradient region were made for the penumbra measurements. The TMS penumbra measurements were essentially < ±2mm within the limits of experimental uncertainty. For CMS, deviations observed for the blocked and MLC shaped fields were as large as (9±1)mm.

From this investigation it is seen that the two treatment planning systems were comparable for point dose calculations in asymmetric, square, and blocked fields. However, for calculations using the MLC, significant deviations were observed in the accuracy of TMS and CMS calculations. TMS calculations were significantly more accurate than those of CMS due to the change in head scatter between the block and MLC fields, not modeled explicitly by CMS. In addition, from evaluation of the isodose

distributions, TMS exhibited higher accuracy in the dose calculations near the clinically significant isodose lines, in comparison with CMS, in the low gradient inner beam region. TMS and CMS performed similarly in the inner beam central region. Extremely significant deviations were observed for block and MLC fields in the high gradient region and penumbra measurements for the CMS distribution. In general, TMS more accurately calculates the dose especially for MLC fields and in the high gradient and penumbra regions.

Further evaluation of these treatment planning systems, in terms of inhomogeneity and contour corrections, would provide additional insight into which treatment planning system more accurately predicts the dose in patient. At CCMB, a wax chest phantom already exists, containing two internal inhomogeneities, cork and plaster. Dose distributions containing the effects of the inhomogeneity could be obtained via film dosimetry. These results could then be compared with the predictions of each of the treatment planning systems using data obtained via a CT scan. Furthermore, changes in dose due to patient contours could be carried out by placing TLDs inside the wax phantom and determining the dose. Again these measurements could be compared with those predicted by the treatment planning systems.

5 Monitor Unit Calculation Verification

A treatment unit delivers radiation in monitor units as measured by the monitor chamber. Each machine is calibrated to deliver k cGy/MU, where k is usually unity, in the standard calibration geometry. In addition to the relative dose distribution, the TPS also provides the number of MU for each beam in order to deliver the prescribed dose to the patient. There are several sources of error, which can result in incorrect MU calculated by a TPS. Some of these errors are: (1) incorrect beam data entry into the TPS; (2) incorrect normalization of relative distribution with respect to the prescription point; (3) wrong selection of wedges; etc [Cal 93]. At the time of commissioning of treatment beams into a TPS, a set of tests are carried out [CMS & TMS] to ensure the accuracy of beam data in the TPS and to assess the accuracy of MU calculations in general. However, unforseen situations such as software bugs, corruption of internal data tables, inappropriate planning procedure, etc still can cause inaccurate MU calculations. Therefore, a completely independent method of MU calculation, which uses independently measured beam data, is desirable to verify the accuracy of MU on a patient to patient basis. The fundamental features of such a method are: (1) user friendliness; (2) unambiguous display of the steps in the MU calculation to resolve differences, if any, with the TPS; and (3) preferably an algorithm which does not mimic the algorithm used in the TPS. It is also desirable that the MU calculation program runs on computers which are separate from the TPS.

In this chapter, a simple MU calculation method is described. This method is implemented using Visual Basic in an Excel spread sheet, and uses the relative beam weightings corresponding to the TMS-Helax system [TMS].

5.1 Theory

The number of monitor units necessary to deliver a given dose GD_i from the i^{th} beam in a treatment plan is given by

5.1 $$MU = GD_i / DoseRate_i .$$

The dose rate (cGy/MU) of the i^{th} beam is determined at the plan normalization point by using a set of measured data and the calibrated dose rate. GD_i is the portion of the dose, prescribed to the normalization point of the plan, to be delivered by the i^{th} beam. The given dose for the i^{th} beam is calculated by relative beam weights in the treatment plan and the individual beam normalization used by a TPS [TMS]. Recall that the normalization point is the point of dose prescription and the relative dose at this point is generally 100%.

The dose rate of the i^{th} beam at the normalization point, $D_i(r_{norm})$ (cGy/MU), is given by

5.2 $$D_i(\vec{r}_{norm}) = k \cdot HSF(e_c) \cdot WHSF(e_c) \cdot PSF(e_b) \cdot TPR(d_{norm}, e_b) \cdot OAR(d_{norm}, r_{offset}) \cdot BHC(d_{norm}, e_b) \cdot IHC \cdot TF \cdot \left(\frac{100}{SSD + d_{norm}}\right)^2 \cdot WF_{off}(wr_{offset}, e_c),$$

where the various parameters are described in detail in the following.

k

is the calibration factor of the treatment unit, usually calibrated to deliver 1cGy/MU at the reference depth d_o, SAD, and for the reference field size r_o of 10cm x 10cm.

$HSF(e_c)$

is the head scatter factor which corrects for the change in the head scattered fluence with field size. In particular, it corrects for the change in head scatter from the reference field size to the equivalent square collimator field size, e_c, of the beam. It is defined as the ratio of the output in air for a given field to that for a reference field (10cm x 10cm). In the case of physical wedges, the change in head scatter fluence is contained in WHSF(e_c) described below. Therefore, HSF(e_c) is set to 1.0 for physical wedges.

WHSF(e_c)

is the wedge head scatter factor which corrects for the increased scattered fluence produced by the physical wedge present in the beam, also evaluated at the equivalent square collimator field size. It is defined as the ratio of the output in air for a wedged beam of a given field size, to that for a wedged beam of reference field (10cm x 10cm). When there is no physical wedge used in a beam, WHSF(e_c) is set to unity since head scattered fluence changed is now contained in HSF(e_c).

PSF(e_b)

is the phantom scatter factor which accounts for the change in dose due to scattered photons in phantom at a reference depth (dmax at CCMB) as a function of field size. It is evaluated for the equivalent square of the blocked field size. PSF is defined as the ratio of the output in-phantom for a given field at a reference depth (ie. dmax) to that for a reference field (10cm x 10cm) at the same depth.

TPR(d_{norm}, e_b)

is the tissue phantom ratio evaluated at the depth of the normalization point, for the blocked field size. It accounts for the change in phantom dose from the reference

depth to the depth of the normalization point. TPR is defined as the ratio of the dose in-phantom at a given depth for a given field at SAD, to that for the same field at a reference depth, at SAD [Khan 94].

$OAR(d_{norm}, r_{offset})$

is the off-axis ratio which corrects for changes in in-phantom dose due to lateral fluence changes caused by the flattening filter as a function of normalization depth and a radial distance, r_{offset}. r_{offset}, is the distance of the normalization point from the central axis of the beam projected in the isocentric plane. OAR is defined as the ratio of the in-phantom dose at the off-axis point of interest to that on the central axis at the same depth.

$BHC(d_{norm}, e_b)$

is the beam hardening correction factor which corrects for the change in beam quality in the presence of physical wedges and filters. It is defined as the ratio of the percentage depth dose for a wedged beam to that for an open (no wedge) beam for the same field size and depth.

$WF_{off}(wr_{offset})$

is the off-axis wedge factor which accounts for the decreased output of the treatment machine in the presence of the physical wedge. wr_{offset} is the distance of the normalization point projected in the isocentric plane from the central axis along the wedge gradient direction. The off-axis wedge factor is given by

$$WF_{off}(wr_{offset}) = WF_{on}(r_0) \cdot e^{-\mu(t-t_0)} \quad 5.3$$

where $WF_{on}(r_o)$ is the wedge factor at the central axis for the reference field r_o (10cm x 10cm), t is the divergent ray line path length through the wedge of the ray

joining the source to the normalization point, t_o is the central axis wedge thickness, and μ is the linear attenuation coefficient for the primary beam energy.

IHC

is the inhomogeneity correction factor defined as the ratio of the dose to the normalization point with and without taking tissue inhomogeneities into account. In the current implementation of MU calculation, this factor is evaluated from the TPS.

TF

is the factor which corrects for attenuation in the tray used to support the blocks and compensators.

$$\left(\frac{100}{SSD + d_{norm}}\right)^2$$

is the inverse square factor, correcting for variation of the output with distance from the source. The SSD is the source to surface distance along the ray joining the source to the normalization point.

The given dose is calculated by the method of standard dose rate normalization [TMS]. The dose rate $D_i(r_{norm})$ is divided by a standard dose rate $D_{std}(d_{max})$, and weighted by a beam weight factor w_i.

5.4
$$R_i = w_i \cdot \frac{D_i(r_{norm})}{D_{std}(d_{max})}$$

where R_i is the weighted dose rate relative to the standard dose rate. The standard dose rate $D_{std}(d_{max})$ is the dose rate in the standard geometry (dmax, 10cmx10cm, SSD=100cm) and is given by

5.5 $$D^{i}_{std}(d_{\max}) = k \cdot \left(\frac{100}{100 + d_{\max}} \right)^{2} \cdot WF_{on}(r_0).$$

The inclusion of the on-axis wedge factor corrects the standard dose rate for the wedge transmission. This allows for the beam weight factor w_i to be proportional to the primary energy fluence. For virtual wedges, the standard dose used is that of the corresponding open field and the wedge factor in equation 5.5 is unity. The given dose of the i^{th} beam , GD_i, is then calculated as follows

5.6 $$GD_i = PD \cdot \frac{R_i}{\sum_i R_i}$$

where PD is the prescription dose. Finally the MUs required to deliver GD_i is given by

5.7 $$MU_i = \frac{GD_i}{D_i(r_{norm}) \cdot BF}$$

where BF is the attenuation factor for cast and breast boards etc.

5.2 Materials and Methods

The monitor unit calculation is an Excel spreadsheet program that uses measured data to calculate the monitor units for the beams designed by the treatment planning system. The program requires input of patient and beam plan parameters, and calculates various parameters defined above via interpolation from measured data. The user interface is illustrated below in Figure 5-1.

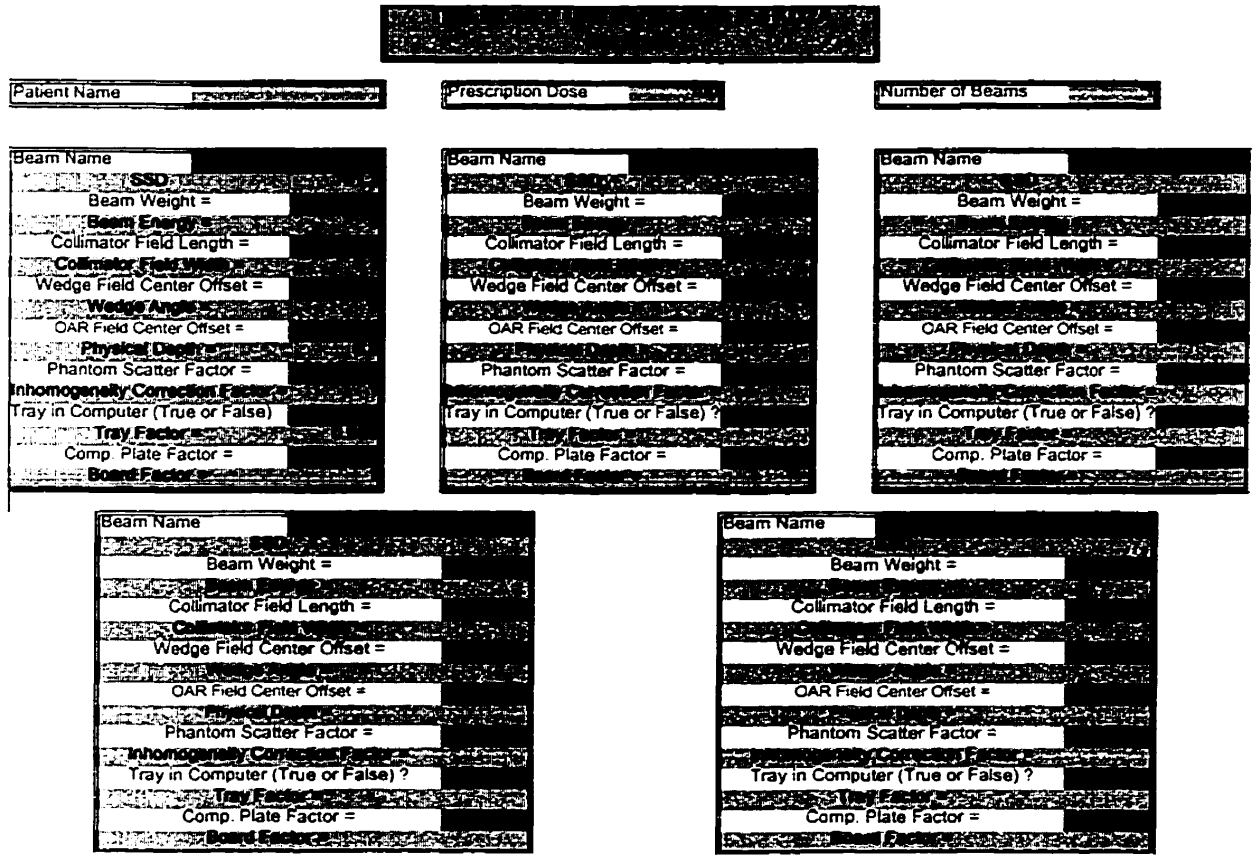

Figure 5-1: Sample of the MU Calculation User Input Interface.

Each parameter listed is entered by the user for each beam. The wr_{offset} (wedge field centre offset), and r_{offset} (OAR field centre offset) are measured from the isodose distribution. The PSF is either provided by TMS for irregular fields or obtained by interpolation from a table of measured PSFs at the equivalent blocked field size. The inhomogeneity correction factor is calculated by TMS as the ratio of the dose with the IHC on and off. The remaining input parameters are entered according to the treatment plan. Figure 5-2 illustrates the MU calculation output data.

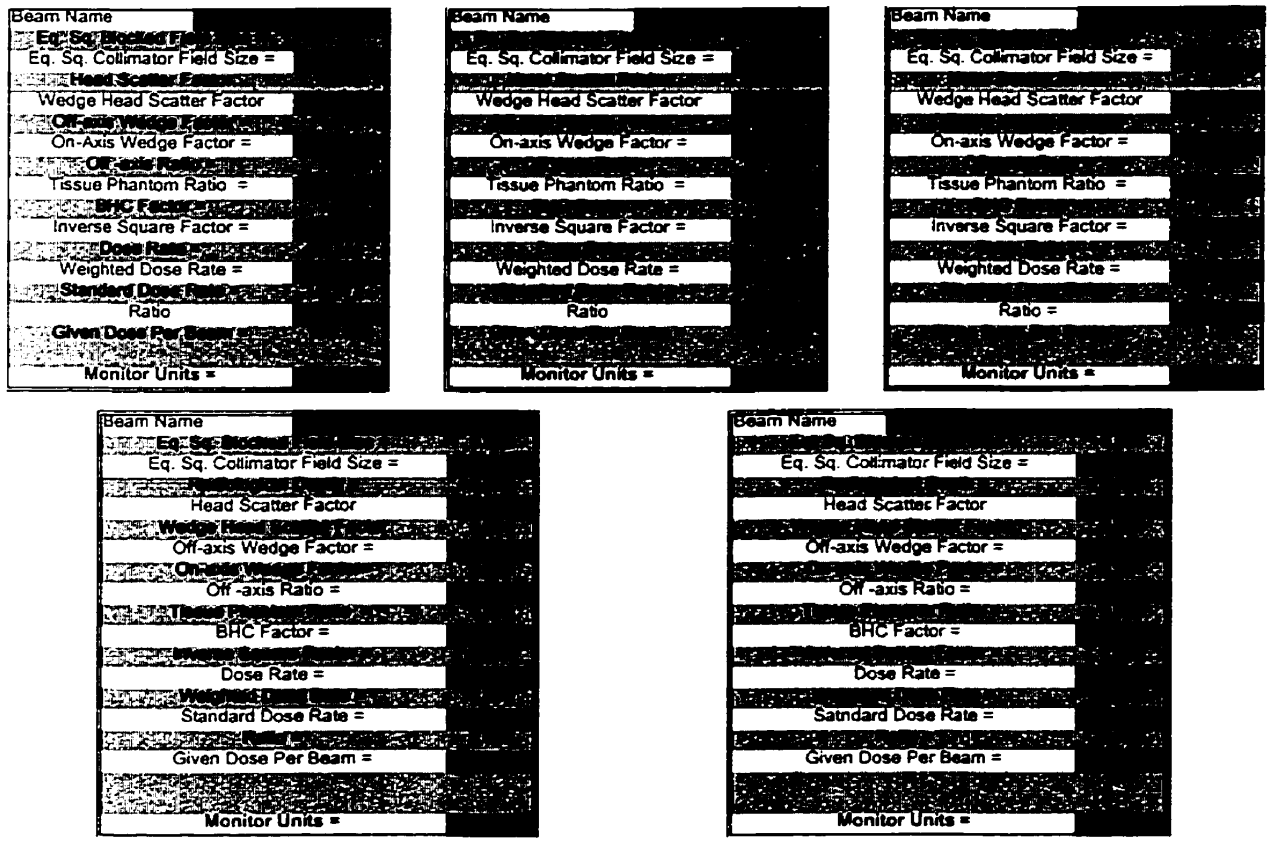

Figure 5-2: MU Calculation Output Interface

The equivalent square blocked field size is determined as the field size whose measured PSF matches the PSF entered by the user. The equivalent square collimator field size is determined by calculating the square having the same area to perimeter ratio as the collimator settings for the beam. The HSF and WHSF are determined by linear interpolation at the equivalent square collimator field size. The on-axis wedge factor is the wedge factor for a 10cmx10cm reference field. The off-axis wedge factor is calculated by equation 5.3. The OAR(dnorm, fco), TPR(E,dnorm, eb,dnorm), and BHC(WA,E,eb,dnorm) are determined via linear interpolation from tables of measured

data. The inverse square factor is given in equation 5.2, and the standard dose rate is calculated using equation 5.5.

5.3 Results and Discussion

Three clinical examples of MU calculations are provided. The MU calculated by both TMS and the Excel program are provided, along with the percent deviation, ΔMU, calculated as a local percent of the MU calculated by TMS. The first example, Table 5-1, involves treatment of a large brain tumour using a wedge pair. The difference in MU calculations for each of the beams is –0.9%. For the three field rectum treatment, Table 5-2, the MU calculated by this program are overestimating by approximately 1%. For the tangential breast treatment, Table 5-3, the MUs calculated by this program are underestimating the TMS calculated MUs by –1.3%. From these few examples it is seen that the MU calculation program successfully provides an independent verification of MUs calculated by TMS.

Table 5-1: MU calculations for a head and neck treatment (wedged pair)

Beam Name	Energy (MV)	Modulators	TMS MU	EXCEL MU	ΔMU
Right Lateral	6	45° wedge	362.1	358.9	-0.9%
Superior Vertex	6	45° wedge	362.2	358.9	-0.9%

Table 5-2: MU calculations for a 3 field rectum treatment

Beam Name	Energy (MV)	Modulators	TMS MU	EXCEL MU	ΔMU
Posterior	6	None	68.9	69.4	0.7%
Right Lateral	15	30° wedge	119.4	1205	0.9%
Left Lateral	15	30° wedge	119.4	120.5	0.9%

Table 5-3: MU calculations for a tangential breast treatment

Beam Name	Energy (MV)	Modulators	TMS MU	EXCEL MU	ΔMU
Right Medial	6	45° wedge	556.8	549.4	-1.3%
Right lateral Oblique	6	45° wedge	556.8	549.4	-1.3%

The major limitations of this program are the inhomogeneity correction factor, the phantom scatter factor, and the MLC head scatter. This MU calculation program does not account for the changes in the head scatter observed for fields formed by the MLC. The IHCF is obtained from TMS, while the PSF is supplied by TMS for irregular fields to calculate the equivalent square blocked field size. This prevents the calculation from being a completely independent check. Future work could involve developing a program that calculates the PSF via Clarkson's integration, and a method independent of TMS for calculating the IHCF.

5.4 Conclusion

An EXCEL MU calculation program was developed to provide an independent verification of MUs calculated by TMS. This assists in eliminating erroneous dose delivery due to incorrect calculation of MUs by TMS. Tests on the program were made for several clinical examples and the maximum deviation observed between MUs calculated by TMS and the program developed here was −1.3%. Typically the average deviation for a breast plan on a linac is 2%, and for ^{60}Co treatment units ranges from 2-4%. Other treatments exhibit errors less than 2%. Thus, this EXCEL program successfully provides an independent verification of MUs calculated by TMS.

6 References

[AA 89] A. Ahnesjo and P. Andreo (1989): Determination of effective bremsstrahlung spectra and electron contamination for photon dose calculations, *Phys. Med. Biol.* **34** 1451-1464.

[AAC 98] C. J. Arsenault, J. -C. Anctil, P. Courteau, and E. R. Lawrence (1998): Dosimetric Verification of a 3D Treatment Planning System Based on a Pencil-Beam Algorithm, presented at the COMP meeting in London, Ontario. June 1998.

[Ahn 92a] A. Ahnesjo (1992): A pencil beam model for photon dose calculation, *Med. Phys.* **19** 263-273.

[Ahn 92b] A. Ahnesjo, T. Knoos, and A. Montelius (1992):Application of the convolution method for calculation of output factors for therapy photon beams, *Med. Phys.* **19** 295-301.

[Ahn 94] A. Ahnesjo (1994): Analytic modeling of photon scatter from flattening filters in photon therapy beams, *Med. Phys.* **21** 1227-1235.

[Ahn 95a] A. Ahnesjo (1995): Collimator Scatter in Photon Therapy Beams, *Med. Phys.* **22** 267-278.

[Ahn 95b] A. Ahnesjo, L. Weber, and P. Nilsson (1995): Modeling transmission and scatter for photon beam attenuators, *Med. Phys.* **22** 1711-1720.

[AT 91] A. Ahnesjo and A. Trepp (1991): Acquisition of the effective lateral energy fluence distribution for photon beam dose calculations by convolution models, *Phys. Med. Biol.*, **36** 973-985.

[BBD 93] H. Beauvais, A. Bridier, and A. Dutreix (1993): Characteristics of contamination electrons in high energy photon beams, *Radiother. Oncol.* **29** 308-316.

[Cal 93] R. Calandrino, G. M. Cattaeo, A. Del Vecchio, C. Fiorino, B. Longobardi, P. Signorotto (1993): Human errors in calculation of monitor units in clinical radiotherapy practice, *Radiotherapy and Oncology*, **28** 86-88.

[CMS] CMS FOCUS Calculation Physics & Clinical Applications Manual for Release 2.4.0, Volumes 1&2.

[Day 50] M. J. Day (1950): A note on the calculation of dose in x-ray fields, *Br. J. Radiol.*, **13** 368-369.

[Fra 98] B. Fraass et al (1998): Americal Association of Physicists in Medicine Radiation Therapy Committee Task Group 53: Quality Assurance for clinical radiotherapy treatment planning, *Med. Phys.* **25** 1773-1823.

[Helax] Dose Formalisms & Models in Helax-TMS, Version 4.0.

[Hig 92] P.D. Higgins, F.H. Attix, J.H. Hubbell, S.M. Seltzer, M.J. Berger and C.H. Sibata (1992): Mass Energy-Transfer and Mass Energy-Absorption Coefficients, Including In-flight Positron Annihilation for Photon Energies 1 keV to 100 keV, *Natl. Inst. Stand. Technol. Internal Report, NISTIR* **4812**

[JT 99] P. A. Jursinic, B. R. Thomadsen (1999): Measurements of head scatter factors with cylindrical build-up caps and columnar miniphantoms, *Med. Phys.* **26** 512-517.

[Khan 94] F. M. Khan (1994): The Physics of Radiation Therapy, 2nd ed. Maryland, Williams & Wilkins.

[Lew 96] J. S. Lewis (1996): Quality Assurance Overview and Procedures for the MCTRF MLC of the KD2-B, *Internal Document, CCMB.*

[Lyd 98] J.M. Lydon (1998): Photon dose calculations in homogeneous media for a treatment planning system using a collapsed cone superposition convolution algorithm, *Phys. Med. Biol.* **43** 1813-1822.

[MS 82] T. R. Mackie and J. W. Scrimger (1982): Contamination of a 15 MV photon beam by electrons and scattered photons, *Radiology* **144** 403-409.

[Nil 85] B. Nilsson (1985): Electron Contamination from different materials in high energy photon beams, *Phys. Med. Biol.* **30** 139-151.

[Van 93] J. Van Dyk et al (1993): Commissioning and Quality Assurance of Treatment Planning Computers, *I. J. Radiation Oncology Biol. Phys.* **26** 261-273.

A. Appendix A

The following are tables of all the measured and calculated output and head scatter factors, as well as the deviations between the measured and calculated isodose distributions.

A.1 Head Scatter Factors

A.1.1 6MV HSFs

Table A-1: 6MV TMS ΔHSFs for Square Fields

Field Side		HSF		ΔHSF	
(cm)	Measured	±	TMS	%	±
15	1.020	0.005	1.019	-0.1	0.4
20	1.030	0.005	1.027	-0.3	0.4
40	1.037	0.005	1.04	0.3	0.4

Table A-2: 6MV TMS ΔHSFs for Asymmetric Fields

Field (cm)		HSF		ΔHSF	
(X1:X2 x Y1:Y2)	Measured	±	TMS	%	±
0:5 x 0:5	0.995	0.005	0.994	-0.1	0.5
0:10 x 0:10	1.051	0.005	1.044	-0.7	0.5
0:15 x 0:15	1.077	0.005	1.075	-0.2	0.5
0:20 x 0:20	1.097	0.005	1.087	-0.9	0.5
0:5 x 5:5	0.998	0.005	0.996	-0.2	0.5
0:10 x 10:10	1.062	0.005	1.059	-0.3	0.5
0:15 x 15:15	1.077	0.005	1.075	-0.2	0.5
0:20 x 20:20	1.090	0.005	1.088	-0.1	0.5
5:5 x 0:5	0.981	0.005	0.989	0.9	0.5
10:10 x 0:10	1.051	0.005	1.045	-0.6	0.5
15:15 x 0:15	1.070	0.005	1.064	-0.6	0.5
20:20 x 0:20	1.085	0.005	1.081	-0.3	0.5

Table A-3: 6MV TMS ΔHSFs for MLC Fields

Field (cm)		HSF		ΔHSF	
Pattern (Y1:Y2)	Measured	±	TMS	%	±
MLC 3 (7.5:7.5)	1.017	0.005	1.019	0.2	0.5
MLC 4 (2.8:3.0)	0.964	0.005	0.966	0.2	0.5
MLC 5 (5.5:5.5)	0.993	0.005	0.993	0.0	0.5
MLC 6 (9.5:9.5)	1.024	0.005	1.028	0.4	0.5
MLC 7 (9.5:9.5)	1.027	0.005	1.024	-0.3	0.5
MLC 8 (13.5:13.5)	0.991	0.004	0.988	-0.3	0.4
MLC 9 (13.5:13.5)	1.005	0.005	1.016	1.1	0.5
MLC 10 (5.0:5.0)	0.998	0.005	0.997	-0.1	0.5

Table A-4: 6MV TMS ΔHSFs for Collimator Fields

Field (cm) Pattern (X x Y)	Measured	HSF ±	TMS	ΔHSF %	±
Pat 3 (15 x 15)	1.020	0.005	1.019	-0.1	0.5
Pat 4 (5.4x2.8:3.0)	0.971	0.004	0.969	-0.2	0.4
Pat 5 (28.4 x 11)	1.013	0.005	1.011	-0.2	0.5
Pat 6 (20x20)	1.028	0.005	1.027	-0.1	0.4
Pat 7 (26.4 x 19)	1.031	0.004	1.029	-0.2	0.4
Pat 8 (5.2:3.9 x 27)	1.015	0.004	1.015	0.0	0.4
Pat 9 (39 x 27)	1.034	0.004	1.035	0.1	0.4
Pat 10 (10x10)	1.000	0.000	1	0.0	0.0

Table A-5: 6MV TMS ΔHSFs for Blocked Fields

Field (cm) Pattern (X x Y)	Measured	HSF ±	TMS	ΔHSF %	±
Pat 3 (15 x 15)	0.992	0.005	0.993	0.1	0.5
Pat 4 (5.4x2.8:3.0)	0.941	0.004	0.938	-0.3	0.4
Pat 5 (28.4 x 11)	0.983	0.005	0.983	0.0	0.5
Pat 6 (20x20)	1.001	0.005	1.005	0.4	0.5
Pat 7 (26.4 x 19)	1.006	0.004	1.004	-0.2	0.4
Pat 8 (5.2:3.9 x 27)	0.985	0.004	0.983	-0.2	0.4
Pat 9 (39 x 27)	0.996	0.004	0.999	0.3	0.4
Pat 10 (10x10)	0.971	0.003	0.97	-0.1	0.4

A.1.2 23MV HSFs

Table A-6: 23MV TMS ΔHSFs for Square Fields

Field Side (cm)	Measured	HSF ±	TMS	ΔHSF %	±
15	1.016	0.003	1.016	0.0	0.3
20	1.024	0.003	1.024	0.0	0.3
40	1.029	0.003	1.03	0.1	0.3

Table A-7: 23MV TMS ΔHSFs for Asymmetric Fields

Field (cm) (X1:X2 x Y1:Y2)	Measured	HSF ±	TMS	ΔHSF %	±
0:5 x 0:5	1.002	0.003	1.008	0.5	0.3
0:10 x 0:10	1.033	0.003	1.047	1.4	0.3
0:15 x 0:15	1.037	0.003	1.07	3.1	0.3
0:20 x 0:20	1.042	0.003	1.08	3.6	0.3
0:5 x 5:5	0.990	0.003	0.986	-0.4	0.3
0:10 x 10:10	1.051	0.003	1.049	-0.2	0.3
0:15 x 15:15	1.039	0.003	1.049	0.9	0.3
0:20 x 20:20	1.036	0.003	1.052	1.5	0.3
5:5 x 0:5	1.001	0.003	1.007	0.6	0.3
10:10 x 0:10	1.059	0.003	1.06	0.1	0.3
15:15 x 0:15	1.053	0.003	1.07	1.6	0.3
20:20 x 0:20	1.052	0.003	1.073	2.0	0.3

Table A-8: 23MV TMS ΔHSFs for MLC Fields

Field (cm) Pattern (Y1:Y2)	Measured	HSF ±	TMS	ΔHSF %	±
MLC 3 (7.5:7.5)	1.013	0.003	1.016	0.3	0.3
MLC 4 (2.8:3.0)	0.969	0.003	0.968	-0.1	0.3
MLC 5 (5.5:5.5)	0.991	0.004	0.991	0.0	0.4
MLC 6 (9.5:9.5)	1.020	0.004	1.024	0.4	0.4
MLC 7 (9.5:9.5)	1.021	0.004	1.02	-0.1	0.4
MLC 8 (13.5:13.5)	0.993	0.003	0.982	-1.1	0.3
MLC 9 (13.5:13.5)	0.999	0.004	1.005	0.6	0.4
MLC 10 (5.0:5.0)	0.999	0.004	0.997	-0.2	0.4

Table A-9: 23MV TMS ΔHSFs for Collimator Fields

Field (cm) Pattern (X x Y)	Measured	HSF ±	TMS	ΔHSF %	±
Pat 3 (15 x 15)	1.016	0.004	1.016	0.0	0.4
Pat 4 (5.4x2.8:3.0)	0.970	0.003	0.971	0.1	0.3
Pat 5 (28.4 x 11)	1.009	0.004	1.008	-0.1	0.4
Pat 6 (20x20)	1.026	0.003	1.024	-0.2	0.3
Pat 7 (26.4 x 19)	1.023	0.003	1.025	0.2	0.3
Pat 8 (5.2:3.9x27)	1.012	0.003	1.013	0.1	0.3
Pat 9 (39 x 27)	1.028	0.003	1.028	0.0	0.3
Pat 10(10x10)	1.000	0.000	1.000	0.0	0.0

Table A-10: 23MV TMS ΔHSFs for Blocked Fields

Field (cm) Pattern (X x Y)	Measured	HSF ±	TMS	ΔHSF %	±
Pat 3 (15 x 15)	1.002	0.004	1.002	0.0	0.4
Pat 4 (5.4x2.8:3.0)	0.952	0.003	0.953	0.1	0.3
Pat 5 (28.4 x 11)	0.992	0.004	0.993	0.1	0.4
Pat 6 (20x20)	1.012	0.003	1.012	0.0	0.3
Pat 7 (26.4 x 19)	1.009	0.003	1.012	0.3	0.3
Pat 8 (5.2:3.9x27)	0.996	0.003	0.993	-0.3	0.3
Pat 9 (39 x 27)	1.005	0.003	1.006	0.1	0.3
Pat 10 (10x10)	0.981	0.003	0.983	0.2	0.3

A.2 Output Factors

A.2.1 TMS OFs

Table A-11: Square Field TMS ΔOFs

Energy	Depth	Square Field		OF		ΔOF	
(MV)	(cm)	(cm)	Measured	±	TMS	%	±
23	3.5	15	1.047	0.000	1.045	-0.2	0.0
23	3.5	20	1.058	0.000	1.061	0.3	0.0
23	3.5	40	1.089	0.000	1.087	-0.2	0.0
23	5	15	1.001	0.000	1.010	0.9	0.0
23	5	20	1.017	0.000	1.030	1.2	0.0
23	5	40	1.041	0.000	1.047	0.6	0.0
23	10	15	0.829	0.000	0.829	0.0	0.1
23	10	20	0.846	0.000	0.848	0.2	0.1
23	10	40	0.874	0.000	0.864	-1.1	0.0
6	1.5	15	1.031	0.000	1.033	0.2	0.0
6	1.5	20	1.050	0.000	1.046	-0.4	0.0
6	1.5	40	1.080	0.000	1.090	0.9	0.0
6	5	15	0.910	0.000	0.91	0.0	0.0
6	5	20	0.932	0.000	0.931	-0.1	0.0
6	5	40	0.965	0.000	0.969	0.4	0.0
6	10	15	0.718	0.000	0.723	0.7	0.1
6	10	20	0.748	0.000	0.749	0.1	0.1
6	10	40	0.786	0.000	0.786	-0.1	0.1

Table A-12: Right Quadrant (0:X x 0:X) Asymmetric Field TMS ΔOFs

Energy	Depth	(X1:X2 x Y1:Y2)		OF		ΔOF	
(MV)	(cm)	(cm)	Measured	±	TMS	%	±
23	3.5	0:5 x 0:5	0.975	0.001	0.965	-1.0	0.1
23	3.5	0:10 x 0:10	1.053	0.001	1.044	-0.9	0.1
23	3.5	0:15 x 0:15	1.096	0.001	1.094	-0.2	0.1
23	3.5	0:20 x 0:20	1.125	0.001	1.119	-0.5	0.1
23	5	0:5 x 0:5	0.947	0.001	0.940	-0.7	0.1
23	5	0:10 x 0:10	1.019	0.001	1.014	-0.5	0.1
23	5	0:15 x 0:15	1.051	0.001	1.059	0.7	0.1
23	5	0:20 x 0:20	1.074	0.001	1.081	0.6	0.1
23	10	0:5 x 0:5	0.765	0.001	0.76	-0.6	0.1
23	10	0:10 x 0:10	0.834	0.001	0.832	-0.2	0.1
23	10	0:15 x 0:15	0.861	0.001	0.868	0.8	0.1
23	10	0:20 x 0:20	0.881	0.001	0.892	1.2	0.1
6	1.5	0:5 x 0:5	0.978	0.001	0.980	0.2	0.1
6	1.5	0:10 x 0:10	1.058	0.001	1.046	-1.1	0.1
6	1.5	0:15 x 0:15	1.108	0.001	1.088	-1.8	0.1
6	1.5	0:20 x 0:20	1.142	0.001	1.115	-2.4	0.1
6	5	0:5 x 0:5	0.835	0.001	0.833	-0.2	0.1
6	5	0:10 x 0:10	0.919	0.001	0.908	-1.2	0.1
6	5	0:15 x 0:15	0.967	0.001	0.957	-1.1	0.1
6	5	0:20 x 0:20	1.002	0.001	0.988	-1.4	0.1
6	10	0:5 x 0:5	0.623	0.001	0.625	0.3	0.2
6	10	0:10 x 0:10	0.709	0.001	0.707	-0.2	0.2
6	10	0:15 x 0:15	0.748	0.001	0.757	1.1	0.2
6	10	0:20 x 0:20	0.782	0.001	0.792	1.3	0.1

Table A-13: Right Half (0:X x X:X) Asymmetric Field TMS ΔOFs

Energy	Depth	(X1:X2 x Y1:Y2)	OF			ΔOF	
(MV)	(cm)	(cm)	Measured	±	TMS	%	±
23	3.5	0:5 x 5:5	0.983	0.001	0.963	-2.0	0.1
23	3.5	0:10 x 10:10	1.080	0.001	1.069	-1.0	0.1
23	3.5	0:15 x 15:15	1.100	0.001	1.088	-1.1	0.1
23	3.5	0:20 x 20:20	1.116	0.001	1.097	-1.7	0.1
23	5	0:5 x 5:5	0.954	0.001	0.937	-1.8	0.1
23	5	0:10 x 10:10	1.042	0.001	1.036	-0.5	0.1
23	5	0:15 x 15:15	1.054	0.001	1.052	-0.2	0.1
23	5	0:20 x 20:20	1.065	0.001	1.059	-0.6	0.1
23	10	0:5 x 5:5	0.777	0.001	0.762	-2.0	0.1
23	10	0:10 x 10:10	0.857	0.001	0.85	-0.8	0.1
23	10	0:15 x 15:15	0.871	0.001	0.869	-0.2	0.1
23	10	0:20 x 20:20	0.881	0.001	0.873	-0.9	0.1
6	1.5	0:5 x 5:5	0.992	0.001	0.984	-0.8	0.1
6	1.5	0:10 x 10:10	1.077	0.001	1.065	-1.1	0.1
6	1.5	0:15 x 15:15	1.118	0.001	1.096	-2.0	0.1
6	1.5	0:20 x 20:20	1.140	0.001	1.123	-1.5	0.1
6	5	0:5 x 5:5	0.854	0.001	0.844	-1.2	0.1
6	5	0:10 x 10:10	0.943	0.001	0.931	-1.2	0.1
6	5	0:15 x 15:15	0.981	0.001	0.968	-1.3	0.1
6	5	0:20 x 20:20	1.007	0.001	0.995	-1.2	0.1
6	10	0:5 x 5:5	0.646	0.001	0.642	-0.7	0.2
6	10	0:10 x 10:10	0.734	0.001	0.734	0.0	0.2
6	10	0:15 x 15:15	0.776	0.001	0.774	-0.2	0.1
6	10	0:20 x 20:20	0.807	0.001	0.8	-0.8	0.1

Table A-14: Top Half (X:X x 0:X) Asymmetric Field TMS ΔOFs

Energy	Depth	(X1:X2 x Y1:Y2)	OF			ΔOF	
(MV)	(cm)	(cm)	Measured	±	TMS	%	±
23	3.5	5:5 x 0:5	0.983	0.001	0.98	-0.3	0.1
23	3.5	10:10 x 0:10	1.085	0.001	1.078	-0.6	0.1
23	3.5	15:15 x 0:15	1.109	0.001	1.104	-0.4	0.1
23	3.5	20:20 x 0:20	1.128	0.001	1.122	-0.5	0.1
23	5	5:5 x 0:5	0.956	0.001	0.954	-0.2	0.1
23	5	10:10 x 0:10	1.047	0.001	1.044	-0.3	0.1
23	5	15:15 x 0:15	1.065	0.001	1.067	0.2	0.1
23	5	20:20 x 0:20	1.078	0.001	1.084	0.6	0.1
23	10	5:5 x 0:5	0.778	0.001	0.775	-0.4	0.1
23	10	10:10 x 0:10	0.861	0.001	0.857	-0.5	0.1
23	10	15:15 x 0:15	0.882	0.001	0.88	-0.2	0.1
23	10	20:20 x 0:20	0.891	0.001	0.893	0.2	0.1
6	1.5	5:5 x 0:5	0.975	0.001	0.982	0.7	0.1
6	1.5	10:10 x 0:10	1.063	0.001	1.054	-0.8	0.1
6	1.5	15:15 x 0:15	1.101	0.001	1.087	-1.3	0.1
6	1.5	20:20 x 0:20	1.129	0.001	1.113	-1.4	0.1
6	5	5:5 x 0:5	0.840	0.001	0.842	0.2	0.1
6	5	10:10 x 0:10	0.933	0.001	0.922	-1.2	0.1
6	5	15:15 x 0:15	0.971	0.001	0.96	-1.1	0.1
6	5	20:20 x 0:20	1.000	0.001	0.987	-1.3	0.1
6	10	5:5 x 0:5	0.638	0.001	0.641	0.5	0.2
6	10	10:10 x 0:10	0.728	0.001	0.728	0.0	0.2
6	10	15:15 x 0:15	0.768	0.001	0.767	-0.2	0.1
6	10	20:20 x 0:20	0.793	0.001	0.794	0.2	0.1

Table A-15: 6MV measured and TMS OFs for the collimated fields of the blocked patterns (block absent)

Depth	(X1:X2 x Y1:Y2)	OF			ΔOF	
(cm)	(cm)	Measured	±	TMS	%	±
1.5	Pat 3 (15 x 15)	1.031	0.000	1.033	0.2	0.0
1.5	Pat 4 (5.4x2.8:3.0)	0.949	0.000	0.954	0.5	0.0
1.5	Pat 5 (28.4 x 11)	1.026	0.000	1.026	0.0	0.0
1.5	Pat 6 (20x20)	1.050	0.000	1.046	-0.4	0.0
1.5	Pat 7 (26.4 x 19)	1.058	0.000	1.059	0.0	0.0
1.5	Pat 8 (5.2:3.9 x 27)	1.026	0.000	1.023	-0.3	0.0
1.5	Pat 9 (39 x 27)	1.077	0.000	1.078	0.1	0.0
1.5	Pat 10 (10x10)	1.000	0.000	1.000	0.0	0.0
5	Pat 3 (15 x 15)	0.908	0.000	0.910	0.2	0.0
5	Pat 4 (5.4x2.8:3.0)	0.816	0.000	0.813	-0.4	0.1
5	Pat 5 (28.4 x 11)	0.902	0.000	0.903	0.1	0.0
5	Pat 6 (20x20)	0.929	0.000	0.931	0.2	0.0
5	Pat 7 (26.4 x 19)	0.933	0.000	0.939	0.6	0.0
5	Pat 8 (5.2:3.9 x 27)	0.896	0.000	0.895	-0.1	0.0
5	Pat 9 (39 x 27)	0.953	0.000	0.956	0.3	0.0
5	Pat 10 (10x10)	0.871	0.000	0.870	-0.1	0.1
10	Pat 3 (15 x 15)	0.718	0.000	0.723	0.7	0.1
10	Pat 4 (5.4x2.8:3.0)	0.613	0.000	0.617	0.7	0.1
10	Pat 5 (28.4 x 11)	0.713	0.000	0.715	0.3	0.1
10	Pat 6 (20x20)	0.743	0.000	0.749	0.8	0.1
10	Pat 7 (26.4 x 19)	0.750	0.000	0.755	0.6	0.1
10	Pat 8 (5.2:3.9 x 27)	0.702	0.000	0.705	0.4	0.1
10	Pat 9 (39 x 27)	0.772	0.000	0.775	0.4	0.1
10	Pat 10 (10x10)	0.674	0.000	0.678	0.6	0.1

Table A-16: 23MV measured and TMS OFs for the collimated fields of the blocked patterns (block absent)

Depth	(X1:X2 x Y1:Y2)	OF			ΔOF	
(cm)	(cm)	Measured	±	TMS	%	±
3.5	Pat 3 (15 x 15)	1.039	0.000	1.045	0.6	0.0
3.5	Pat 4 (5.4x2.8:3.0)	0.943	0.000	0.934	-0.9	0.0
3.5	Pat 5 (28.4 x 11)	1.031	0.000	1.035	0.4	0.0
3.5	Pat 6 (20x20)	1.059	0.001	1.061	0.1	0.0
3.5	Pat 7 (26.4 x 19)	1.062	0.000	1.072	0.9	0.0
3.5	Pat 8 (5.2:3.9 x 27)	1.030	0.000	1.024	-0.6	0.0
3.5	Pat 9 (39 x 27)	1.081	0.000	1.082	0.1	0.0
3.5	Pat 10 (10x10)	1.000	0.000	1.000	0.0	0.0
5	Pat 3 (15 x 15)	1.002	0.000	1.010	0.8	0.0
5	Pat 4 (5.4x2.8:3.0)	0.916	0.000	0.910	-0.7	0.0
5	Pat 5 (28.4 x 11)	0.993	0.000	1.001	0.8	0.0
5	Pat 6 (20x20)	1.017	0.001	1.030	1.3	0.1
5	Pat 7 (26.4 x 19)	1.020	0.000	1.034	1.3	0.0
5	Pat 8 (5.2:3.9 x 27)	0.993	0.000	0.992	-0.1	0.0
5	Pat 9 (39 x 27)	1.034	0.000	1.043	0.8	0.0
5	Pat 10 (10x10)	0.970	0.000	0.971	0.1	0.0
10	Pat 3 (15 x 15)	0.829	0.000	0.829	0.0	0.1
10	Pat 4 (5.4x2.8:3.0)	0.746	0.000	0.742	-0.5	0.1
10	Pat 5 (28.4 x 11)	0.823	0.000	0.822	-0.1	0.1
10	Pat 6 (20x20)	0.845	0.001	0.848	0.3	0.1
10	Pat 7 (26.4 x 19)	0.850	0.000	0.850	0.0	0.1
10	Pat 8 (5.2:3.9 x 27)	0.820	0.000	0.815	-0.7	0.1
10	Pat 9 (39 x 27)	0.866	0.000	0.8598	-0.7	0.0
10	Pat 10 (10x10)	0.799	0.000	0.796	-0.4	0.1

Table A-17: 23MV measured and TMS OFs for blocked field patterns

Pattern (X1:X2 x Y1:Y2)	Depth (cm)	OF Measured	±	OF TMS	ΔOF %	±
Pat 3 (15 x 15)	3.5	1.024	0.000	1.018	-0.6	0.0
Pat 3 (15 x 15)	5	0.984	0.000	0.988	0.4	0.0
Pat 3 (15 x 15)	10	0.812	0.000	0.813	0.2	0.1
Pat 4 (5.4x2.8:3.0)	3.5	0.921	0.000	0.907	-1.4	0.0
Pat 4 (5.4x2.8:3.0)	5	0.893	0.000	0.885	-0.9	0.0
Pat 4 (5.4x2.8:3.0)	10	0.725	0.000	0.721	-0.5	0.1
Pat 5 (28.4 x 11)	3.5	0.992	0.000	0.974	-1.8	0.0
Pat 5 (28.4 x 11)	5	0.957	0.000	0.947	-1.0	0.0
Pat 5 (28.4 x 11)	10	0.782	0.000	0.776	-0.8	0.1
Pat 6 (20x20)	3.5	1.045	0.001	1.046	0.1	0.0
Pat 6 (20x20)	5	1.000	0.001	1.012	1.1	0.1
Pat 6 (20x20)	10	0.828	0.001	0.834	0.7	0.1
Pat 7 (26.4 x 19)	3.5	1.045	0.000	1.043	-0.1	0.0
Pat 7 (26.4 x 19)	5	1.000	0.000	1.009	0.9	0.0
Pat 7 (26.4 x 19)	10	0.829	0.000	0.830	0.1	0.1
Pat 8 (5.2:3.9 x 27)	3.5	0.992	0.000	0.968	-2.5	0.0
Pat 8 (5.2:3.9 x 27)	5	0.957	0.000	0.941	-1.6	0.0
Pat 8 (5.2:3.9 x 27)	10	0.781	0.000	0.770	-1.4	0.1
Pat 9 (39 x 27)	3.5	1.025	0.000	1.015	-1.0	0.0
Pat 9 (39 x 27)	5	0.985	0.000	0.983	-0.2	0.0
Pat 9 (39 x 27)	10	0.810	0.000	0.805	-0.6	0.1
Pat 10 (10x10)	3.5	0.982	0.000	0.966	-1.6	0.0
Pat 10 (10x10)	5	0.951	0.000	0.942	-0.9	0.0
Pat 10 (10x10)	10	0.780	0.000	0.775	-0.5	0.1

Table A-18: 6MV measured and TMS OFs for blocked field patterns

Pattern (X1:X2 x Y1:Y2)	Depth (cm)	OF Measured	●	OF TMS	ΔOF %	±
Pat 3 (15 x 15)	1.5	1.000	0.000	1.004	0.4	0.0
Pat 3 (15 x 15)	5	0.878	0.000	0.882	0.4	0.1
Pat 3 (15 x 15)	10	0.692	0.000	0.699	1.0	0.1
Pat 4 (5.4x2.8:3.0)	1.5	0.915	0.000	0.921	0.6	0.0
Pat 4 (5.4x2.8:3.0)	5	0.785	0.000	0.783	-0.3	0.1
Pat 4 (5.4x2.8:3.0)	10	0.587	0.000	0.590	0.5	0.1
Pat 5 (28.4 x 11)	1.5	0.978	0.000	0.979	0.1	0.0
Pat 5 (28.4 x 11)	5	0.846	0.000	0.845	-0.1	0.1
Pat 5 (28.4 x 11)	10	0.650	0.000	0.653	0.5	0.1
Pat 6 (20x20)	1.5	1.021	0.000	1.025	0.4	0.0
Pat 6 (20x20)	5	0.897	0.000	0.905	0.9	0.0
Pat 6 (20x20)	10	0.715	0.000	0.726	1.5	0.1
Pat 7 (26.4 x 19)	1.5	1.027	0.000	1.024	-0.3	0.0
Pat 7 (26.4 x 19)	5	0.899	0.000	0.905	0.6	0.0
Pat 7 (26.4 x 19)	10	0.716	0.000	0.722	0.9	0.1
Pat 8 (5.2:3.9 x 27)	1.5	0.979	0.000	0.971	-0.8	0.0
Pat 8 (5.2:3.9 x 27)	5	0.843	0.000	0.837	-0.8	0.1
Pat 8 (5.2:3.9 x 27)	10	0.645	0.000	0.645	0.0	0.1
Pat 9 (39 x 27)	1.5	1.014	0.000	1.015	0.1	0.0
Pat 9 (39 x 27)	5	0.879	0.000	0.883	0.5	0.1
Pat 9 (39 x 27)	10	0.687	0.000	0.696	1.2	0.1
Pat 10 (10x10)	1.5	0.968	0.000	0.967	0.0	0.0
Pat 10 (10x10)	5	0.838	0.000	0.839	0.1	0.1
Pat 10 (10x10)	10	0.646	0.000	0.651	0.8	0.1

Table A-19: 23MV measured and TMS OFs for MLC field patterns

Pattern (X1:X2 x Y1:Y2)	Depth (cm)	OF Measured	OF ±	TMS	ΔOF %	ΔOF ±
Pat 3 (15 x 15)	3.5	1.033	0.000	1.038	0.4	0.0
Pat 3 (15 x 15)	5	0.999	0.000	1.005	0.6	0.0
Pat 3 (15 x 15)	10	0.827	0.000	0.826	-0.1	0.1
Pat 4 (5.4x2.8:3.0)	3.5	0.930	0.000	0.925	-0.5	0.0
Pat 4 (5.4x2.8:3.0)	5	0.906	0.000	0.901	-0.6	0.0
Pat 4 (5.4x2.8:3.0)	10	0.736	0.000	0.734	-0.3	0.1
Pat 5 (28.4 x 11)	3.5	0.985	0.000	0.977	-0.8	0.0
Pat 5 (28.4 x 11)	5	0.955	0.000	0.949	-0.6	0.0
Pat 5 (28.4 x 11)	10	0.782	0.000	0.776	-0.8	0.1
Pat 6 (20x20)	3.5	1.052	0.000	1.062	0.9	0.0
Pat 6 (20x20)	5	1.012	0.000	1.026	1.4	0.0
Pat 6 (20x20)	10	0.841	0.000	0.843	0.3	0.1
Pat 7 (26.4 x 19)	3.5	1.052	0.000	1.055	0.3	0.0
Pat 7 (26.4 x 19)	5	1.013	0.000	1.019	0.6	0.0
Pat 7 (26.4 x 19)	10	0.842	0.000	0.838	-0.4	0.1
Pat 8 (5.2:3.9 x 27)	3.5	0.977	0.001	0.959	-1.8	0.1
Pat 8 (5.2:3.9 x 27)	5	0.946	0.001	0.933	-1.4	0.1
Pat 8 (5.2:3.9 x 27)	10	0.771	0.000	0.763	-1.2	0.1
Pat 9 (39 x 27)	3.5	1.016	0.000	1.011	-0.5	0.0
Pat 9 (39 x 27)	5	0.978	0.000	0.979	0.1	0.0
Pat 9 (39 x 27)	10	0.807	0.000	0.802	-0.7	0.1
Pat 10 (10x10)	3.5	0.992	0.000	0.986	-0.6	0.0
Pat 10 (10x10)	5	0.965	0.000	0.959	-0.7	0.0
Pat 10 (10x10)	10	0.794	0.000	0.787	-0.9	0.1

Table A-20: 6MV measured and TMS OFs for MLC field patterns

Pattern (X1:X2 x Y1:Y2)	Depth (cm)	OF Measured	OF ±	TMS	ΔOF %	ΔOF ±
Pat 3 (15 x 15)	1.5	1.027	0.000	1.031	0.4	0.0
Pat 3 (15 x 15)	5	0.908	0.000	0.906	-0.2	0.0
Pat 3 (15 x 15)	10	0.715	0.000	0.717	0.2	0.1
Pat 4 (5.4x2.8:3.0)	1.5	0.943	0.000	0.949	0.7	0.0
Pat 4 (5.4x2.8:3.0)	5	0.810	0.000	0.806	-0.5	0.1
Pat 4 (5.4x2.8:3.0)	10	0.606	0.000	0.608	0.3	0.1
Pat 5 (28.4 x 11)	1.5	0.988	0.000	0.991	0.2	0.0
Pat 5 (28.4 x 11)	5	0.863	0.000	0.854	-0.9	0.1
Pat 5 (28.4 x 11)	10	0.662	0.000	0.660	-0.4	0.1
Pat 6 (20x20)	1.5	1.044	0.000	1.048	0.4	0.0
Pat 6 (20x20)	5	0.927	0.000	0.927	0.0	0.0
Pat 6 (20x20)	10	0.739	0.000	0.741	0.3	0.1
Pat 7 (26.4 x 19)	1.5	1.045	0.000	1.046	0.1	0.0
Pat 7 (26.4 x 19)	5	0.927	0.000	0.924	-0.4	0.0
Pat 7 (26.4 x 19)	10	0.738	0.000	0.737	-0.2	0.1
Pat 8 (5.2:3.9 x 27)	1.5	0.984	0.000	0.978	-0.6	0.0
Pat 8 (5.2:3.9 x 27)	5	0.855	0.000	0.842	-1.5	0.1
Pat 8 (5.2:3.9 x 27)	10	0.653	0.000	0.648	-0.8	0.1
Pat 9 (39 x 27)	1.5	1.015	0.000	1.032	1.7	0.0
Pat 9 (39 x 27)	5	0.890	0.000	0.897	0.8	0.1
Pat 9 (39 x 27)	10	0.698	0.000	0.704	0.8	0.1
Pat 10 (10x10)	1.5	0.994	0.000	0.994	-0.1	0.0
Pat 10 (10x10)	5	0.869	0.000	0.861	-0.9	0.1
Pat 10 (10x10)	10	0.669	0.000	0.668	-0.2	0.1

Table A-21: 23 MV 15°Virtual Wedge measured and TMS OFs

Field (X1:X2 x Y1:Y2)	Depth (cm)	OF Measured	±	OF TMS	ΔOF %	±
0:5 x 0:5	3.5	0.944	0.001	0.940	-0.4	0.1
0:5 x 0:5	5	0.917	0.001	0.916	-0.1	0.1
0:5 x 0:5	10	0.740	0.001	0.742	0.3	0.2
0:5 x 5:5	3.5	0.977	0.001	0.968	-0.9	0.1
0:5 x 5:5	5	0.949	0.001	0.942	-0.7	0.1
0:5 x 5:5	10	0.772	0.001	0.767	-0.6	0.1
5:5 x 0:5	3.5	0.951	0.001	0.954	0.3	0.1
5:5 x 0:5	5	0.922	0.001	0.928	0.6	0.1
5:5 x 0:5	10	0.753	0.001	0.756	0.4	0.1
0:10 x 0:10	3.5	0.995	0.001	0.986	-0.9	0.1
0:10 x 0:10	5	0.961	0.001	0.958	-0.3	0.1
0:10 x 0:10	10	0.789	0.001	0.789	0.0	0.1
0:10 x 10:10	3.5	1.078	0.001	1.076	-0.2	0.1
0:10 x 10:10	5	1.039	0.001	1.039	0.0	0.1
0:10 x 10:10	10	0.855	0.001	0.855	0.0	0.1
10:10 x 0:10	3.5	1.019	0.001	1.015	-0.4	0.1
10:10 x 0:10	5	0.985	0.001	0.984	-0.1	0.1
10:10 x 0:10	10	0.811	0.001	0.809	-0.2	0.1
0:15 x 0:15	3.5	1.003	0.001	1.003	0.0	0.1
0:15 x 0:15	5	0.963	0.001	0.972	1.0	0.1
0:15 x 0:15	10	0.792	0.001	0.802	1.3	0.1
15:15 x 0:15	3.5	1.017	0.001	1.009	-0.8	0.1
15:15 x 0:15	5	0.976	0.001	0.976	0.0	0.1
15:15 x 0:15	10	0.811	0.001	0.808	-0.3	0.1
0:20 x 0:20	3.5	1.007	0.001	0.999	-0.8	0.1
0:20 x 0:20	5	0.962	0.001	0.967	0.6	0.1
0:20 x 0:20	10	0.794	0.001	0.801	0.9	0.1
20:20 x 0:20	3.5	1.009	0.001	0.996	-1.3	0.1
20:20 x 0:20	5	0.965	0.001	0.963	-0.2	0.1
20:20 x 0:20	10	0.801	0.001	0.798	-0.4	0.1

Table A-22: 23 MV 30°Virtual Wedge measured and TMS OFs

Field (X1:X2 x Y1:Y2)	Depth (cm)	OF			ΔOF	
		Measured	±	TMS	%	±
0:5 x 0:5	3.5	0.908	0.001	0.910	0.2	0.1
0:5 x 0:5	5	0.883	0.001	0.887	0.5	0.1
0:5 x 0:5	10	0.714	0.001	0.720	0.9	0.2
0:5 x 5:5	3.5	0.970	0.001	0.971	0.1	0.1
0:5 x 5:5	5	0.943	0.001	0.943	0.0	0.1
0:5 x 5:5	10	0.768	0.001	0.769	0.2	0.1
5:5 x 0:5	3.5	0.914	0.001	0.923	1.0	0.1
5:5 x 0:5	5	0.888	0.001	0.899	1.2	0.1
5:5 x 0:5	10	0.725	0.001	0.733	1.2	0.2
0:10 x 0:10	3.5	0.925	0.001	0.923	-0.2	0.1
0:10 x 0:10	5	0.896	0.001	0.898	0.2	0.1
0:10 x 0:10	10	0.737	0.001	0.742	0.6	0.2
0:10 x 10:10	3.5	1.071	0.001	1.081	0.9	0.1
0:10 x 10:10	5	1.033	0.001	1.045	1.2	0.1
0:10 x 10:10	10	0.849	0.001	0.859	1.1	0.1
10:10 x 0:10	3.5	0.948	0.001	0.951	0.3	0.1
10:10 x 0:10	5	0.916	0.001	0.922	0.6	0.1
10:10 x 0:10	10	0.758	0.001	0.761	0.5	0.1
0:15 x 0:15	3.5	0.903	0.001	0.909	0.7	0.1
0:15 x 0:15	5	0.869	0.001	0.883	1.6	0.1
0:15 x 0:15	10	0.718	0.001	0.732	1.9	0.2
15:15 x 0:15	3.5	0.916	0.001	0.916	0.0	0.1
15:15 x 0:15	5	0.879	0.001	0.887	0.9	0.1
15:15 x 0:15	10	0.735	0.001	0.737	0.3	0.2
0:20 x 0:20	3.5	0.877	0.001	0.878	0.1	0.1
0:20 x 0:20	5	0.840	0.001	0.851	1.3	0.1
0:20 x 0:20	10	0.697	0.001	0.709	1.8	0.2
20:20 x 0:20	3.5	0.878	0.001	0.876	-0.3	0.1
20:20 x 0:20	5	0.842	0.001	0.848	0.7	0.1
20:20 x 0:20	10	0.702	0.001	0.706	0.6	0.2

Table A-23: 23 MV 45°Virtual Wedge measured and TMS OFs

Field (X1:X2 x Y1:Y2)	Depth (cm)	OF Measured	±	TMS	ΔOF %	±
0:5 x 0:5	3.5	0.858	0.001	0.870	1.4	0.1
0:5 x 0:5	5	0.838	0.001	0.849	1.3	0.1
0:5 x 0:5	10	0.679	0.001	0.690	1.6	0.2
0:5 x 5:5	3.5	0.964	0.001	0.975	1.2	0.1
0:5 x 5:5	5	0.937	0.001	0.947	1.1	0.1
0:5 x 5:5	10	0.764	0.001	0.772	1.0	0.1
5:5 x 0:5	3.5	0.866	0.001	0.883	2.0	0.1
5:5 x 0:5	5	0.843	0.001	0.860	2.0	0.1
5:5 x 0:5	10	0.689	0.001	0.703	2.0	0.2
0:10 x 0:10	3.5	0.838	0.001	0.845	0.8	0.1
0:10 x 0:10	5	0.812	0.001	0.823	1.3	0.1
0:10 x 0:10	10	0.671	0.001	0.682	1.6	0.2
0:10 x 10:10	3.5	1.069	0.001	1.090	1.9	0.1
0:10 x 10:10	5	1.031	0.001	1.053	2.1	0.1
0:10 x 10:10	10	0.849	0.001	0.867	2.1	0.1
10:10 x 0:10	3.5	0.857	0.001	0.870	1.5	0.1
10:10 x 0:10	5	0.830	0.001	0.845	1.8	0.1
10:10 x 0:10	10	0.690	0.001	0.699	1.3	0.2
0:15 x 0:15	3.5	0.784	0.001	0.797	1.7	0.1
0:15 x 0:15	5	0.755	0.001	0.776	2.7	0.2
0:15 x 0:15	10	0.627	0.001	0.646	3.1	0.2
15:15 x 0:15	3.5	0.793	0.001	0.802	1.1	0.1
15:15 x 0:15	5	0.764	0.001	0.779	2.0	0.1
15:15 x 0:15	10	0.641	0.001	0.651	1.6	0.2
0:20 x 0:20	3.5	0.727	0.001	0.738	1.5	0.2
0:20 x 0:20	5	0.698	0.001	0.717	2.7	0.2
0:20 x 0:20	10	0.584	0.001	0.602	3.1	0.2
20:20 x 0:20	3.5	0.728	0.001	0.736	1.1	0.2
20:20 x 0:20	5	0.700	0.001	0.715	2.2	0.2
20:20 x 0:20	10	0.590	0.001	0.600	1.8	0.2

Table A-24: 23 MV 60°Virtual Wedge measured and TMS OFs

Field (X1:X2 x Y1:Y2)	Depth (cm)	OF Measured	±	TMS	ΔOF %	●
0:5 x 0:5	3.5	0.795	0.001	0.806	1.4	0.1
0:5 x 0:5	5	0.775	0.001	0.787	1.6	0.1
0:5 x 0:5	10	0.631	0.001	0.643	2.0	0.1
0:5 x 5:5	3.5	0.962	0.001	0.982	2.1	0.1
0:5 x 5:5	5	0.936	0.001	0.955	2.0	0.1
0:5 x 5:5	10	0.763	0.001	0.779	2.1	0.1
5:5 x 0:5	3.5	0.801	0.001	0.818	2.2	0.1
5:5 x 0:5	5	0.780	0.001	0.798	2.3	0.1
5:5 x 0:5	10	0.640	0.001	0.655	2.3	0.1
0:10 x 0:10	3.5	0.716	0.001	0.725	1.3	0.2
0:10 x 0:10	5	0.694	0.001	0.708	2.0	0.2
0:10 x 0:10	10	0.578	0.001	0.591	2.2	0.2
0:10 x 10:10	3.5	1.076	0.001	1.112	3.4	0.1
0:10 x 10:10	5	1.038	0.001	1.075	3.5	0.1
0:10 x 10:10	10	0.854	0.001	0.886	3.7	0.1
10:10 x 0:10	3.5	0.733	0.001	0.747	1.9	0.2
10:10 x 0:10	5	0.709	0.001	0.727	2.5	0.2
10:10 x 0:10	10	0.593	0.001	0.606	2.2	0.2
0:15 x 0:15	3.5	0.620	0.001	0.636	2.6	0.2
0:15 x 0:15	5	0.600	0.001	0.621	3.5	0.2
0:15 x 0:15	10	0.503	0.001	0.523	3.9	0.2
15:15 x 0:15	3.5	0.627	0.001	0.641	2.2	0.2
15:15 x 0:15	5	0.606	0.001	0.624	2.9	0.2
15:15 x 0:15	10	0.512	0.001	0.527	3.0	0.2
0:20 x 0:20	3.5	0.535	0.001	0.548	2.5	0.2
0:20 x 0:20	5	0.516	0.001	0.535	3.6	0.2
0:20 x 0:20	10	0.436	0.001	0.456	4.6	0.3
20:20 x 0:20	3.5	0.536	0.001	0.548	2.3	0.2
20:20 x 0:20	5	0.517	0.001	0.534	3.2	0.2
20:20 x 0:20	10	0.443	0.001	0.454	2.5	0.3

Table A-25: 6 MV 15°Virtual Wedge measured and TMS OFs

Field (X1:X2 x Y1:Y2)	Depth (cm)	OF Measured	±	TMS	ΔOF %	±
0:5 x 0:5	1.5	0.952	0.001	0.946	-0.7	0.1
0:5 x 0:5	5	0.812	0.001	0.805	-0.9	0.1
0:5 x 0:5	10	0.605	0.001	0.605	-0.1	0.2
0:5 x 5:5	1.5	0.992	0.001	0.987	-0.5	0.1
0:5 x 5:5	5	0.850	0.001	0.842	-0.9	0.1
0:5 x 5:5	10	0.642	0.001	0.643	0.1	0.2
5:5 x 0:5	1.5	0.935	0.001	0.948	1.4	0.1
5:5 x 0:5	5	0.803	0.001	0.814	1.3	0.1
5:5 x 0:5	10	0.609	0.001	0.622	2.2	0.2
0:10 x 0:10	1.5	0.981	0.001	0.972	-0.9	0.1
0:10 x 0:10	5	0.848	0.001	0.846	-0.3	0.1
0:10 x 0:10	10	0.653	0.001	0.661	1.3	0.2
0:10 x 10:10	1.5	1.078	0.001	1.072	-0.5	0.1
0:10 x 10:10	5	0.937	0.001	0.936	-0.1	0.1
0:10 x 10:10	10	0.729	0.001	0.737	1.1	0.2
10:10 x 0:10	1.5	0.986	0.001	0.98	-0.6	0.1
10:10 x 0:10	5	0.860	0.001	0.859	-0.1	0.1
10:10 x 0:10	10	0.672	0.001	0.679	1.1	0.2
0:15 x 0:15	1.5	0.994	0.001	0.976	-1.8	0.1
0:15 x 0:15	5	0.863	0.001	0.861	-0.3	0.1
0:15 x 0:15	10	0.675	0.001	0.685	1.5	0.2
15:15 x 0:15	1.5	0.987	0.001	0.976	-1.2	0.1
15:15 x 0:15	5	0.864	0.001	0.864	0.0	0.1
15:15 x 0:15	10	0.687	0.001	0.694	1.0	0.2
0:20 x 0:20	1.5	0.992	0.001	0.963	-2.9	0.1
0:20 x 0:20	5	0.862	0.001	0.856	-0.7	0.1
0:20 x 0:20	10	0.677	0.001	0.688	1.7	0.2
20:20 x 0:20	1.5	0.978	0.001	0.962	-1.7	0.1
20:20 x 0:20	5	0.858	0.001	0.856	-0.3	0.1
20:20 x 0:20	10	0.686	0.001	0.692	0.8	0.2

Table A-26: 6 MV 30°Virtual Wedge measured and TMS OFs

Field (X1:X2 x Y1:Y2)	Depth (cm)	OF Measured	OF ●	OF TMS	ΔOF %	ΔOF ±
0:5 x 0:5	1.5	0.910	0.001	0.908	-0.2	0.1
0:5 x 0:5	5	0.776	0.001	0.773	-0.3	0.1
0:5 x 0:5	10	0.580	0.001	0.582	0.3	0.2
0:5 x 5:5	1.5	0.988	0.001	0.989	0.1	0.1
0:5 x 5:5	5	0.849	0.001	0.845	-0.5	0.1
0:5 x 5:5	10	0.641	0.001	0.645	0.6	0.2
5:5 x 0:5	1.5	0.891	0.001	0.909	2.0	0.1
5:5 x 0:5	5	0.767	0.001	0.782	1.9	0.2
5:5 x 0:5	10	0.583	0.001	0.598	2.6	0.2
0:10 x 0:10	1.5	0.897	0.001	0.894	-0.4	0.1
0:10 x 0:10	5	0.778	0.001	0.78	0.2	0.1
0:10 x 0:10	10	0.601	0.001	0.612	1.8	0.2
0:10 x 10:10	1.5	1.076	0.001	1.078	0.2	0.1
0:10 x 10:10	5	0.936	0.001	0.941	0.5	0.1
0:10 x 10:10	10	0.731	0.001	0.741	1.3	0.2
10:10 x 0:10	1.5	0.900	0.001	0.901	0.1	0.1
10:10 x 0:10	5	0.789	0.001	0.792	0.4	0.1
10:10 x 0:10	10	0.618	0.001	0.629	1.8	0.2
0:15 x 0:15	1.5	0.872	0.001	0.862	-1.2	0.1
0:15 x 0:15	5	0.761	0.001	0.763	0.3	0.2
0:15 x 0:15	10	0.598	0.001	0.61	2.0	0.2
15:15 x 0:15	1.5	0.865	0.001	0.862	-0.4	0.1
15:15 x 0:15	5	0.762	0.001	0.766	0.5	0.2
15:15 x 0:15	10	0.609	0.001	0.619	1.7	0.2
0:20 x 0:20	1.5	0.834	0.001	0.817	-2.1	0.1
0:20 x 0:20	5	0.731	0.001	0.73	-0.1	0.2
0:20 x 0:20	10	0.578	0.001	0.592	2.3	0.2
20:20 x 0:20	1.5	0.824	0.001	0.817	-0.9	0.1
20:20 x 0:20	5	0.726	0.001	0.731	0.7	0.2
20:20 x 0:20	10	0.585	0.001	0.595	1.6	0.2

Table A-27: 6 MV 45°Virtual Wedge measured and TMS OFs

Field (X1:X2 x Y1:Y2)	Depth (cm)	OF Measured	±	TMS	ΔOF %	±
0:5 x 0:5	1.5	0.858	0.001	0.857	-0.1	0.1
0:5 x 0:5	5	0.733	0.001	0.732	-0.2	0.2
0:5 x 0:5	10	0.549	0.001	0.552	0.5	0.2
0:5 x 5:5	1.5	0.988	0.001	0.993	0.5	0.1
0:5 x 5:5	5	0.848	0.001	0.848	0.0	0.1
0:5 x 5:5	10	0.642	0.001	0.648	1.0	0.2
5:5 x 0:5	1.5	0.841	0.001	0.859	2.2	0.1
5:5 x 0:5	5	0.724	0.001	0.741	2.3	0.2
5:5 x 0:5	10	0.551	0.001	0.568	3.0	0.2
0:10 x 0:10	1.5	0.800	0.001	0.798	-0.2	0.1
0:10 x 0:10	5	0.696	0.001	0.699	0.5	0.2
0:10 x 0:10	10	0.539	0.001	0.551	2.2	0.2
0:10 x 10:10	1.5	1.082	0.001	1.088	0.5	0.1
0:10 x 10:10	5	0.941	0.001	0.951	1.0	0.1
0:10 x 10:10	10	0.736	0.001	0.75	1.9	0.2
10:10 x 0:10	1.5	0.802	0.001	0.805	0.4	0.1
10:10 x 0:10	5	0.705	0.001	0.71	0.7	0.2
10:10 x 0:10	10	0.555	0.001	0.567	2.1	0.2
0:15 x 0:15	1.5	0.736	0.001	0.729	-0.9	0.2
0:15 x 0:15	5	0.644	0.001	0.649	0.7	0.2
0:15 x 0:15	10	0.511	0.001	0.523	2.4	0.2
15:15 x 0:15	1.5	0.729	0.001	0.729	0.0	0.2
15:15 x 0:15	5	0.646	0.001	0.652	1.0	0.2
15:15 x 0:15	10	0.519	0.001	0.53	2.1	0.2
0:20 x 0:20	1.5	0.665	0.001	0.655	-1.6	0.2
0:20 x 0:20	5	0.587	0.001	0.59	0.5	0.2
0:20 x 0:20	10	0.470	0.001	0.483	2.8	0.2
20:20 x 0:20	1.5	0.657	0.001	0.655	-0.2	0.2
20:20 x 0:20	5	0.585	0.001	0.591	1.1	0.2
20:20 x 0:20	10	0.476	0.001	0.486	2.1	0.2

Table A-28: 6 MV 60°Virtual Wedge measured and TMS OFs

Field (X1:X2 x Y1:Y2)	Depth (cm)	OF Measured	±	TMS	ΔOF %	±
0:5 x 0:5	1.5	0.773	0.001	0.778	0.7	0.2
0:5 x 0:5	5	0.662	0.001	0.666	0.5	0.2
0:5 x 0:5	10	0.499	0.001	0.505	1.3	0.2
0:5 x 5:5	1.5	0.988	0.001	1.002	1.4	0.1
0:5 x 5:5	5	0.847	0.001	0.856	1.1	0.1
0:5 x 5:5	10	0.642	0.001	0.654	1.9	0.2
5:5 x 0:5	1.5	0.756	0.001	0.779	3.0	0.2
5:5 x 0:5	5	0.654	0.001	0.674	3.1	0.2
5:5 x 0:5	10	0.500	0.001	0.519	3.8	0.2
0:10 x 0:10	1.5	0.653	0.001	0.657	0.7	0.2
0:10 x 0:10	5	0.571	0.001	0.579	1.4	0.2
0:10 x 0:10	10	0.448	0.001	0.46	2.6	0.3
0:10 x 10:10	1.5	1.104	0.001	1.114	1.0	0.1
0:10 x 10:10	5	0.961	0.001	0.976	1.5	0.1
0:10 x 10:10	10	0.753	0.001	0.772	2.6	0.2
10:10 x 0:10	1 5	0.655	0.001	0.663	1.2	0.2
10:10 x 0:10	5	0.578	0.001	0.589	1.8	0.2
10:10 x 0:10	10	0.461	0.001	0.474	2.9	0.3
0:15 x 0:15	1.5	0.547	0.001	0.547	0.0	0.2
0:15 x 0:15	5	0.486	0.001	0.492	1.2	0.2
0:15 x 0:15	10	0.390	0.001	0.402	3.1	0.3
15:15 x 0:15	1.5	0.543	0.001	0.548	1.0	0.2
15:15 x 0:15	5	0.486	0.001	0.495	1.9	0.2
15:15 x 0:15	10	0.396	0.001	0.408	3.1	0.3
0:20 x 0:20	1.5	0.452	0.001	0.451	-0.3	0.3
0:20 x 0:20	5	0.406	0.001	0.412	1.4	0.3
0:20 x 0:20	10	0.331	0.001	0.343	3.6	0.4
20:20 x 0:20	1.5	0.446	0.001	0.452	1.3	0.3
20:20 x 0:20	5	0.403	0.001	0.413	2.5	0.3
20:20 x 0:20	10	0.334	0.001	0.346	3.6	0.4

A.2.2 CMS OFs

Table A-29: Square Field CMS ΔOFs

Energy	Depth	Square Field		OF		ΔOF	
(MV)	(cm)	*(cm)*	Measured	±	CMS	%	±
23	3.5	15	1.047	0.000	1.039	-0.8	0.0
23	3.5	20	1.058	0.000	1.059	0.1	0.0
23	5	15	1.001	0.000	1.003	0.3	0.0
23	5	20	1.017	0.000	1.018	0.0	0.0
23	10	15	0.829	0.000	0.832	0.3	0.1
23	10	20	0.846	0.000	0.847	0.1	0.1
6	1.5	15	1.031	0.000	1.033	0.2	0.0
6	1.5	20	1.050	0.000	1.057	0.6	0.0
6	5	15	0.910	0.000	0.907	-0.3	0.0
6	5	20	0.932	0.000	0.933	0.1	0.0
6	10	15	0.718	0.000	0.716	-0.3	0.1
6	10	20	0.748	0.000	0.745	-0.5	0.1

Table A-30: Right Quadrant (0:X x 0:X) Asymmetric Field CMS ΔOFs

Energy	Depth	(X1:X2 x Y1:Y2)		OF		ΔOF	
(MV)	(cm)	(cm)	Measured	±	CMS	%	±
23	3.5	0:5 x 0:5	0.975	0.001	0.956	-1.9	0.1
23	3.5	0:10 x 0:10	1.053	0.001	1.043	-0.9	0.1
23	3.5	0:15 x 0:15	1.096	0.001	1.081	-1.4	0.1
23	5	0:5 x 0:5	0.947	0.001	0.927	-2.1	0.1
23	5	0:10 x 0:10	1.019	0.001	1.008	-1.1	0.1
23	5	0:15 x 0:15	1.051	0.001	1.038	-1.3	0.1
23	10	0:5 x 0:5	0.765	0.001	0.747	-2.4	0.1
23	10	0:10 x 0:10	0.834	0.001	0.828	-0.7	0.1
23	10	0:15 x 0:15	0.861	0.001	0.851	-1.1	0.1
6	1.5	0:5 x 0:5	0.978	0.001	0.970	-0.9	0.1
6	1.5	0:10 x 0:10	1.058	0.001	1.052	-0.5	0.1
6	1.5	0:15 x 0:15	1.108	0.001	1.105	-0.2	0.1
6	5	0:5 x 0:5	0.835	0.001	0.829	-0.7	0.1
6	5	0:10 x 0:10	0.919	0.001	0.907	-1.3	0.1
6	5	0:15 x 0:15	0.967	0.001	0.954	-1.4	0.1
6	10	0:5 x 0:5	0.623	0.001	0.616	-1.1	0.2
6	10	0:10 x 0:10	0.709	0.001	0.697	-1.7	0.2
6	10	0:15 x 0:15	0.748	0.001	0.745	-0.5	0.2

Table A-31: Right Half (0:X x X:X) Asymmetric Field CMS ΔOFs

Energy	Depth	(X1:X2 x Y1:Y2)		OF		ΔOF	
(MV)	(cm)	(cm)	Measured	±	CMS	%	±
23	3.5	0:5 x 5:5	0.983	0.001	0.974	-0.9	0.1
23	3.5	0:10 x 10:10	1.080	0.001	1.082	0.2	0.1
23	3.5	0:15 x 15:15	1.100	0.001	1.103	0.2	0.1
23	5	0:5 x 5:5	0.954	0.001	0.947	-0.8	0.1
23	5	0:10 x 10:10	1.042	0.001	1.040	-0.2	0.1
23	5	0:15 x 15:15	1.054	0.001	1.053	0.0	0.1
23	10	0:5 x 5:5	0.777	0.001	0.770	-0.9	0.1
23	10	0:10 x 10:10	0.857	0.001	0.855	-0.2	0.1
23	10	0:15 x 15:15	0.871	0.001	0.875	0.5	0.1
6	1.5	0:5 x 5:5	0.992	0.001	0.975	-1.7	0.1
6	1.5	0:10 x 10:10	1.077	0.001	1.068	-0.9	0.1
6	1.5	0:15 x 15:15	1.118	0.001	1.112	-0.6	0.1
6	5	0:5 x 5:5	0.854	0.001	0.841	-1.5	0.1
6	5	0:10 x 10:10	0.943	0.001	0.929	-1.4	0.1
6	5	0:15 x 15:15	0.981	0.001	0.972	-1.0	0.1
6	10	0:5 x 5:5	0.646	0.001	0.637	-1.4	0.2
6	10	0:10 x 10:10	0.734	0.001	0.726	-1.1	0.2
6	10	0:15 x 15:15	0.776	0.001	0.771	-0.7	0.1

Table A-32: Top Half (X:X x 0:X) Asymmetric Field CMS ΔOFs

Energy	Depth	(X1:X2 x Y1:Y2)		OF		ΔOF	
(MV)	(cm)	(cm)	Measured	±	CMS	%	±
23	3.5	5:5 x 0:5	0.983	0.001	0.974	-0.9	0.1
23	3.5	10:10 x 0:10	1.085	0.001	1.082	-0.3	0.1
23	3.5	15:15 x 0:15	1.109	0.001	1.103	-0.5	0.1
23	5	5:5 x 0:5	0.956	0.001	0.947	-0.9	0.1
23	5	10:10 x 0:10	1.047	0.001	1.040	-0.6	0.1
23	5	15:15 x 0:15	1.065	0.001	1.053	-1.1	0.1
23	10	5:5 x 0:5	0.778	0.001	0.770	-1.0	0.1
23	10	10:10 x 0:10	0.861	0.001	0.855	-0.7	0.1
23	10	15:15 x 0:15	0.8821	0.0011	0.875	-0.8	0.1
6	1.5	5:5 x 0:5	0.975	0.001	0.975	0.0	0.1
6	1.5	10:10 x 0:10	1.063	0.001	1.068	0.4	0.1
6	1.5	15:15 x 0:15	1.1009	0.0012	1.112	1.0	0.1
6	5	5:5 x 0:5	0.840	0.001	0.841	0.1	0.1
6	5	10:10 x 0:10	0.933	0.001	0.929	-0.4	0.1
6	5	15:15 x 0:15	0.9707	0.0012	0.972	0.1	0.1
6	10	5:5 x 0:5	0.638	0.001	0.636	-0.2	0.2
6	10	10:10 x 0:10	0.728	0.001	0.726	-0.2	0.2
6	10	15:15 x 0:15	0.7683	0.0011	0.771	0.3	0.1

Table A-33: 6MV measured and CMS OFs for the collimated fields of the blocked patterns (block absent)

Depth	(X1:X2 x Y1:Y2)	OF			ΔOF	
(cm)	(cm)	Measured	±	CMS	%	±
1.5	Pat 3 (15 x 15)	1.0312	0.0005	1.033	0.2	0.0
1.5	Pat 4 (5.4x2.8:3.0)	0.9486	0.0005	0.949	0.1	0.0
1.5	Pat 5 (28.4 x 11)	1.0258	0.0005	1.037	1.1	0.0
1.5	Pat 6 (20x20)	1.0500	0.0005	1.057	0.7	0.0
1.5	Pat 7 (26.4 x 19)	1.0584	0.0005	1.062	0.4	0.0
1.5	Pat 8 (5.2:3.9 x 27)	1.0257	0.0005	1.024	-0.1	0.0
1.5	Pat 10 (10x10)	1.0000	0.0000	1.000	0.0	0.0
5	Pat 3 (15 x 15)	0.9083	0.0004	0.907	-0.1	0.0
5	Pat 4 (5.4x2.8:3.0)	0.8163	0.0004	0.818	0.2	0.1
5	Pat 5 (28.4 x 11)	0.9025	0.0004	0.911	0.9	0.0
5	Pat 6 (20x20)	0.9292	0.0004	0.933	0.4	0.0
5	Pat 7 (26.4 x 19)	0.9329	0.0004	0.939	0.6	0.0
5	Pat 8 (5.2:3.9 x 27)	0.8959	0.0004	0.898	0.2	0.0
5	Pat 10 (10x10)	0.8709	0.0004	0.871	0.0	0.1
10	Pat 3 (15 x 15)	0.7182	0.0004	0.716	-0.3	0.1
10	Pat 4 (5.4x2.8:3.0)	0.6125	0.0004	0.615	0.4	0.1
10	Pat 5 (28.4 x 11)	0.7129	0.0004	0.722	1.2	0.1
10	Pat 6 (20x20)	0.7430	0.0004	0.745	0.3	0.1
10	Pat 7 (26.4 x 19)	0.7503	0.0004	0.753	0.3	0.1
10	Pat 8 (5.2:3.9 x 27)	0.7019	0.0004	0.706	0.5	0.1
10	Pat 10 (10x10)	0.6743	0.0004	0.675	0.1	0.1

Table A-34: 23MV measured and CMS OFs for the collimated fields of the blocked patterns (block absent)

Depth	(X1:X2 x Y1:Y2)	OF			ΔOF	
(cm)	(cm)	Measured	±	CMS	%	±
3.5	Pat 3 (15 x 15)	1.0388	0.0005	1.039	0.0	0.0
3.5	Pat 4 (5.4x2.8:3.0)	0.9430	0.0004	0.939	-0.4	0.0
3.5	Pat 5 (28.4 x 11)	1.0306	0.0005	1.044	1.3	0.0
3.5	Pat 6 (20x20)	1.0595	0.0005	1.059	-0.1	0.0
3.5	Pat 7 (26.4 x 19)	1.0621	0.0005	1.065	0.3	0.0
3.5	Pat 8 (5.2:3.9 x 27)	1.0300	0.0005	1.030	0.0	0.0
3.5	Pat 10 (10x10)	1.0000	0.0000	1.000	0.0	0.0
5	Pat 3 (15 x 15)	1.0017	0.0005	1.003	0.2	0.0
5	Pat 4 (5.4x2.8:3.0)	0.9162	0.0004	0.915	-0.2	0.0
5	Pat 5 (28.4 x 11)	0.9935	0.0005	1.008	1.4	0.0
5	Pat 6 (20x20)	1.0165	0.0005	1.018	0.1	0.1
5	Pat 7 (26.4 x 19)	1.0204	0.0005	1.022	0.2	0.0
5	Pat 8 (5.2:3.9 x 27)	0.9935	0.0005	0.996	0.2	0.0
5	Pat 10 (10x10)	0.9704	0.0004	0.971	0.1	0.0
10	Pat 3 (15 x 15)	0.8290	0.0004	0.832	0.3	0.1
10	Pat 4 (5.4x2.8:3.0)	0.7456	0.0004	0.744	-0.2	0.1
10	Pat 5 (28.4 x 11)	0.8230	0.0004	0.836	1.5	0.1
10	Pat 6 (20x20)	0.8454	0.0006	0.847	0.2	0.1
10	Pat 7 (26.4 x 19)	0.8500	0.0004	0.852	0.3	0.1
10	Pat 8 (5.2:3.9 x 27)	0.8203	0.0004	0.823	0.4	0.1
10	Pat 10 (10x10)	0.7988	0.0004	0.799	0.1	0.1

Table A-35: 23MV measured and CMS OFs for blocked field patterns

Pattern (X1:X2 x Y1:Y2)	Depth (cm)	OF Measured	±	OF CMS	ΔOF %	±
Pat 3 (15 x 15)	3.5	1.024	0.000	1.017	-0.7	0.0
Pat 3 (15 x 15)	5	0.984	0.000	0.983	-0.1	0.0
Pat 3 (15 x 15)	10	0.812	0.000	0.814	0.3	0.1
Pat 4 (5.4x2.8:3.0)	3.5	0.921	0.000	0.919	-0.1	0.0
Pat 4 (5.4x2.8:3.0)	5	0.893	0.000	0.895	0.1	0.0
Pat 4 (5.4x2.8:3.0)	10	0.725	0.000	0.726	0.1	0.1
Pat 5 (28.4 x 11)	3.5	0.992	0.000	1.017	2.5	0.0
Pat 5 (28.4 x 11)	5	0.957	0.000	0.981	2.6	0.0
Pat 5 (28.4 x 11)	10	0.782	0.000	0.804	2.9	0.1
Pat 6 (20x20)	3.5	1.045	0.001	1.036	-0.9	0.0
Pat 6 (20x20)	5	1.000	0.001	0.998	-0.3	0.1
Pat 6 (20x20)	10	0.828	0.001	0.829	0.1	0.1
Pat 7 (26.4 x 19)	3.5	1.045	0.000	1.041	-0.4	0.0
Pat 7 (26.4 x 19)	5	1.000	0.000	1.002	0.2	0.0
Pat 7 (26.4 x 19)	10	0.829	0.000	0.833	0.4	0.1
Pat 8 (5.2:3.9 x 27)	3.5	0.992	0.000	0.999	0.7	0.0
Pat 8 (5.2:3.9 x 27)	5	0.957	0.000	0.970	1.4	0.0
Pat 8 (5.2:3.9 x 27)	10	0.781	0.000	0.793	1.6	0.1
Pat 10 (10x10)	3.5	0.982	0.000	0.978	-0.4	0.0
Pat 10 (10x10)	5	0.951	0.000	0.951	0.0	0.0
Pat 10 (10x10)	10	0.780	0.000	0.781	0.2	0.1

Table A-36: 6MV measured and CMS OFs for blocked field patterns

Pattern (X1:X2 x Y1:Y2)	Depth (cm)	OF Measured	±	OF CMS	ΔOF %	±
Pat 3 (15 x 15)	1.5	1.000	0.000	0.997	-0.3	0.0
Pat 3 (15 x 15)	5	0.878	0.000	0.874	-0.5	0.0
Pat 3 (15 x 15)	10	0.692	0.000	0.689	-0.4	0.1
Pat 4 (5.4x2.8:3.0)	1.5	0.915	0.000	0.917	0.1	0.0
Pat 4 (5.4x2.8:3.0)	5	0.785	0.000	0.788	0.3	0.1
Pat 4 (5.4x2.8:3.0)	10	0.587	0.000	0.588	0.2	0.1
Pat 5 (28.4 x 11)	1.5	0.978	0.000	0.987	0.9	0.0
Pat 5 (28.4 x 11)	5	0.846	0.000	0.857	1.2	0.1
Pat 5 (28.4 x 11)	10	0.650	0.000	0.657	1.2	0.1
Pat 6 (20x20)	1.5	1.021	0.000	1.018	-0.2	0.0
Pat 6 (20x20)	5	0.897	0.000	0.897	-0.1	0.0
Pat 6 (20x20)	10	0.715	0.000	0.714	-0.1	0.1
Pat 7 (26.4 x 19)	1.5	1.027	0.000	1.020	-0.6	0.0
Pat 7 (26.4 x 19)	5	0.899	0.000	0.898	-0.1	0.0
Pat 7 (26.4 x 19)	10	0.716	0.000	0.714	-0.2	0.1
Pat 8 (5.2:3.9 x 27)	1.5	0.979	0.000	0.976	-0.3	0.0
Pat 8 (5.2:3.9 x 27)	5	0.843	0.000	0.846	0.3	0.1
Pat 8 (5.2:3.9 x 27)	10	0.645	0.000	0.647	0.3	0.1
Pat 10 (10x10)	1.5	0.968	0.000	0.963	-0.4	0.0
Pat 10 (10x10)	5	0.838	0.000	0.836	-0.3	0.1
Pat 10 (10x10)	10	0.646	0.000	0.644	-0.3	0.1

Table A-37: 23MV measured and CMS Ofs for MLC field patterns

Pattern (X1:X2 x Y1:Y2)	Depth (cm)	Measured	OF ±	CMS	ΔOF %	ΔOF ±
Pat 3 (15 x 15)	3.5	1.033	0.000	1.038	0.4	0.0
Pat 3 (15 x 15)	5	0.999	0.000	1.003	0.4	0.0
Pat 3 (15 x 15)	10	0.827	0.000	0.830	0.4	0.1
Pat 4 (5.4x2.8:3.0)	3.5	0.930	0.000	0.938	0.9	0.0
Pat 4 (5.4x2.8:3.0)	5	0.906	0.000	0.913	0.7	0.0
Pat 4 (5.4x2.8:3.0)	10	0.736	0.000	0.740	0.6	0.1
Pat 5 (28.4 x 11)	3.5	0.985	0.000	1.033	4.9	0.0
Pat 5 (28.4 x 11)	5	0.955	0.000	1.001	4.9	0.0
Pat 5 (28.4 x 11)	10	0.782	0.000	0.820	4.9	0.1
Pat 6 (20x20)	3.5	1.052	0.000	1.057	0.4	0.0
Pat 6 (20x20)	5	1.012	0.000	1.018	0.6	0.0
Pat 6 (20x20)	10	0.841	0.000	0.846	0.6	0.1
Pat 7 (26.4 x 19)	3.5	1.052	0.000	1.062	1.0	0.0
Pat 7 (26.4 x 19)	5	1.013	0.000	1.023	1.0	0.0
Pat 7 (26.4 x 19)	10	0.842	0.000	0.850	0.9	0.1
Pat 8 (5.2:3.9 x 27)	3.5	0.977	0.001	1.020	4.4	0.1
Pat 8 (5.2:3.9 x 27)	5	0.946	0.001	0.990	4.6	0.1
Pat 8 (5.2:3.9 x 27)	10	0.771	0.000	0.810	4.9	0.1
Pat 10 (10x10)	3.5	0.992	0.000	0.998	0.6	0.0
Pat 10 (10x10)	5	0.965	0.000	0.970	0.5	0.0
Pat 10 (10x10)	10	0.794	0.000	0.797	0.4	0.1

Table A-38: 6MV measured and CMS OFs for MLC field patterns

Pattern (X1:X2 x Y1:Y2)	Depth (cm)	Measured	OF ±	CMS	ΔOF %	ΔOF ±
Pat 3 (15 x 15)	1.5	1.027	0.000	1.030	0.3	0.0
Pat 3 (15 x 15)	5	0.908	0.000	0.903	-0.5	0.0
Pat 3 (15 x 15)	10	0.715	0.000	0.712	-0.4	0.1
Pat 4 (5.4x2.8:3.0)	1.5	0.943	0.000	0.947	0.5	0.0
Pat 4 (5.4x2.8:3.0)	5	0.810	0.000	0.814	0.4	0.1
Pat 4 (5.4x2.8:3.0)	10	0.606	0.000	0.608	0.2	0.1
Pat 5 (28.4 x 11)	1.5	0.988	0.000	1.019	3.1	0.0
Pat 5 (28.4 x 11)	5	0.863	0.000	0.885	2.6	0.1
Pat 5 (28.4 x 11)	10	0.662	0.000	0.679	2.6	0.1
Pat 6 (20x20)	1.5	1.044	0.000	1.052	0.8	0.0
Pat 6 (20x20)	5	0.927	0.000	0.926	-0.1	0.0
Pat 6 (20x20)	10	0.739	0.000	0.738	-0.1	0.1
Pat 7 (26.4 x 19)	1.5	1.045	0.000	1.054	0.9	0.0
Pat 7 (26.4 x 19)	5	0.927	0.000	0.928	0.1	0.0
Pat 7 (26.4 x 19)	10	0.738	0.000	0.738	0.0	0.1
Pat 8 (5.2:3.9 x 27)	1.5	0.984	0.000	1.008	2.5	0.0
Pat 8 (5.2:3.9 x 27)	5	0.855	0.000	0.874	2.2	0.1
Pat 8 (5.2:3.9 x 27)	10	0.653	0.000	0.668	2.3	0.1
Pat 10 (10x10)	1.5	0.994	0.000	0.995	0.1	0.0
Pat 10 (10x10)	5	0.869	0.000	0.863	-0.6	0.1
Pat 10 (10x10)	10	0.669	0.000	0.665	-0.5	0.1

Table A-39: 23 MV 15°Virtual Wedge measured and CMS OFs

Field (X1:X2 x Y1:Y2)	Depth (cm)	OF Measured	OF ±	OF CMS	ΔOF %	ΔOF ±
0:5 x 0:5	3.5	0.944	0.001	0.913	-3.3	0.1
0:5 x 0:5	5	0.917	0.001	0.886	-3.4	0.1
0:5 x 0:5	10	0.740	0.001	0.715	-3.4	0.1
0:5 x 5:5	3.5	0.977	0.001	0.974	-0.3	0.1
0:5 x 5:5	5	0.949	0.001	0.946	-0.3	0.1
0:5 x 5:5	10	0.772	0.001	0.770	-0.2	0.1
5:5 x 0:5	3.5	0.951	0.001	0.930	-2.3	0.1
5:5 x 0:5	5	0.922	0.001	0.904	-2.0	0.1
5:5 x 0:5	10	0.753	0.001	0.738	-2.0	0.1
0:10 x 0:10	3.5	0.995	0.001	0.961	-3.4	0.1
0:10 x 0:10	5	0.961	0.001	0.930	-3.3	0.1
0:10 x 0:10	10	0.789	0.001	0.766	-2.9	0.1
0:10 x 10:10	3.5	1.078	0.001	1.081	0.3	0.1
0:10 x 10:10	5	1.039	0.001	1.040	0.1	0.1
0:10 x 10:10	10	0.855	0.001	0.855	-0.1	0.1
10:10 x 0:10	3.5	1.019	0.001	0.996	-2.2	0.1
10:10 x 0:10	5	0.985	0.001	0.959	-2.6	0.1
10:10 x 0:10	10	0.811	0.001	0.791	-2.4	0.1

Table A-40: 23 MV 30°Virtual Wedge measured and CMS OFs

Field (X1:X2 x Y1:Y2)	Depth (cm)	OF Measured	OF ±	OF CMS	ΔOF %	ΔOF ±
0:5 x 0:5	3.5	0.908	0.001	0.892	-1.7	0.1
0:5 x 0:5	5	0.883	0.001	0.866	-2.0	0.1
0:5 x 0:5	10	0.714	0.001	0.699	-2.0	0.2
0:5 x 5:5	3.5	0.970	0.001	0.974	0.4	0.1
0:5 x 5:5	5	0.943	0.001	0.946	0.4	0.1
0:5 x 5:5	10	0.768	0.001	0.770	0.3	0.1
5:5 x 0:5	3.5	0.914	0.001	0.908	-0.6	0.1
5:5 x 0:5	5	0.888	0.001	0.884	-0.5	0.1
5:5 x 0:5	10	0.725	0.001	0.722	-0.4	0.2
0:10 x 0:10	3.5	0.925	0.001	0.906	-2.1	0.1
0:10 x 0:10	5	0.896	0.001	0.877	-2.1	0.1
0:10 x 0:10	10	0.737	0.001	0.725	-1.6	0.1
0:10 x 10:10	3.5	1.071	0.001	1.081	0.9	0.1
0:10 x 10:10	5	1.033	0.001	1.039	0.6	0.1
0:10 x 10:10	10	0.849	0.001	0.855	0.6	0.1
10:10 x 0:10	3.5	0.948	0.001	0.939	-0.9	0.1
10:10 x 0:10	5	0.916	0.001	0.905	-1.2	0.1
10:10 x 0:10	10	0.758	0.001	0.749	-1.1	0.1

Table A-41: 23 MV 45°Virtual Wedge measured and CMS OFs

Field (X1:X2 x Y1:Y2)	Depth (cm)	OF Measured	±	CMS	ΔOF %	±
0:5 x 0:5	3.5	0.858	0.001	0.852	-0.7	0.1
0:5 x 0:5	5	0.838	0.001	0.827	-1.3	0.1
0:5 x 0:5	10	0.679	0.001	0.670	-1.3	0.2
0:5 x 5:5	3.5	0.964	0.001	0.974	1.0	0.1
0:5 x 5:5	5	0.937	0.001	0.946	1.0	0.1
0:5 x 5:5	10	0.764	0.001	0.770	0.8	0.1
5:5 x 0:5	3.5	0.866	0.001	0.868	0.2	0.1
5:5 x 0:5	5	0.843	0.001	0.845	0.2	0.1
5:5 x 0:5	10	0.689	0.001	0.691	0.3	0.2
0:10 x 0:10	3.5	0.838	0.001	0.824	-1.7	0.1
0:10 x 0:10	5	0.812	0.001	0.800	-1.5	0.1
0:10 x 0:10	10	0.671	0.001	0.664	-1.1	0.2
0:10 x 10:10	3.5	1.069	0.001	1.080	1.0	0.1
0:10 x 10:10	5	1.031	0.001	1.039	0.7	0.1
0:10 x 10:10	10	0.849	0.001	0.854	0.6	0.1
10:10 x 0:10	3.5	0.857	0.001	0.856	-0.2	0.1
10:10 x 0:10	5	0.830	0.001	0.826	-0.5	0.1
10:10 x 0:10	10	0.690	0.001	0.686	-0.5	0.2

Table A-42: 23 MV 60°Virtual Wedge measured and CMS OFs

Field (X1:X2 x Y1:Y2)	Depth (cm)	OF Measured	±	CMS	ΔOF %	±
0:5 x 0:5	3.5	0.795	0.001	0.794	-0.1	0.1
0:5 x 0:5	5	0.775	0.001	0.772	-0.4	0.1
0:5 x 0:5	10	0.631	0.001	0.627	-0.6	0.1
0:5 x 5:5	3.5	0.962	0.001	0.974	1.3	0.1
0:5 x 5:5	5	0.936	0.001	0.946	1.1	0.1
0:5 x 5:5	10	0.763	0.001	0.770	1.0	0.1
5:5 x 0:5	3.5	0.801	0.001	0.809	1.0	0.1
5:5 x 0:5	5	0.780	0.001	0.788	1.0	0.1
5:5 x 0:5	10	0.640	0.001	0.647	1.1	0.1
0:10 x 0:10	3.5	0.716	0.001	0.713	-0.4	0.2
0:10 x 0:10	5	0.694	0.001	0.693	-0.1	0.2
0:10 x 0:10	10	0.578	0.001	0.580	0.3	0.2
0:10 x 10:10	3.5	1.076	0.001	1.080	0.4	0.1
0:10 x 10:10	5	1.038	0.001	1.039	0.1	0.1
0:10 x 10:10	10	0.854	0.001	0.854	0.0	0.1
10:10 x 0:10	3.5	0.733	0.001	0.740	0.9	0.2
10:10 x 0:10	5	0.709	0.001	0.716	1.0	0.2
10:10 x 0:10	10	0.593	0.001	0.599	1.1	0.2

Table A-43: 6 MV 15°Virtual Wedge measured and CMS OFs

Field (X1:X2 x Y1:Y2)	Depth (cm)	OF Measured	±	CMS	ΔOF %	±
0:5 x 0:5	1.5	0.952	0.001	0.930	-2.3	0.1
0:5 x 0:5	5	0.812	0.001	0.796	-2.0	0.1
0:5 x 0:5	10	0.605	0.001	0.594	-2.0	0.2
0:5 x 5:5	1.5	0.992	0.001	0.975	-1.7	0.1
0:5 x 5:5	5	0.850	0.001	0.841	-1.0	0.1
0:5 x 5:5	10	0.642	0.001	0.636	-1.0	0.2
5:5 x 0:5	1.5	0.935	0.001	0.936	0.1	0.1
5:5 x 0:5	5	0.803	0.001	0.809	0.6	0.1
5:5 x 0:5	10	0.609	0.001	0.612	0.6	0.2
0:10 x 0:10	1.5	0.981	0.001	0.972	-1.0	0.1
0:10 x 0:10	5	0.848	0.001	0.839	-1.1	0.1
0:10 x 0:10	10	0.653	0.001	0.647	-0.9	0.2
0:10 x 10:10	1.5	1.078	0.001	1.067	-1.0	0.1
0:10 x 10:10	5	0.937	0.001	0.929	-0.8	0.1
0:10 x 10:10	10	0.729	0.001	0.726	-0.4	0.2
10:10 x 0:10	1.5	0.986	0.001	0.986	0.0	0.1
10:10 x 0:10	5	0.860	0.001	0.861	0.1	0.1
10:10 x 0:10	10	0.672	0.001	0.675	0.4	0.2

Table A-44: 6 MV 30°Virtual Wedge measured and CMS OFs

Field (X1:X2 x Y1:Y2)	Depth (cm)	OF Measured	±	CMS	ΔOF %	±
0:5 x 0:5	1.5	0.910	0.001	0.899	-1.2	0.1
0:5 x 0:5	5	0.776	0.001	0.770	-0.7	0.1
0:5 x 0:5	10	0.580	0.001	0.575	-0.9	0.2
0:5 x 5:5	1.5	0.988	0.001	0.975	-1.3	0.1
0:5 x 5:5	5	0.849	0.001	0.841	-0.9	0.1
0:5 x 5:5	10	0.641	0.001	0.636	-0.8	0.2
5:5 x 0:5	1.5	0.891	0.001	0.904	1.4	0.1
5:5 x 0:5	5	0.767	0.001	0.782	1.9	0.2
5:5 x 0:5	10	0.583	0.001	0.593	1.8	0.2
0:10 x 0:10	1.5	0.897	0.001	0.902	0.5	0.1
0:10 x 0:10	5	0.778	0.001	0.782	0.4	0.1
0:10 x 0:10	10	0.601	0.001	0.605	0.6	0.2
0:10 x 10:10	1.5	1.076	0.001	1.066	-0.9	0.1
0:10 x 10:10	5	0.936	0.001	0.929	-0.8	0.1
0:10 x 10:10	10	0.731	0.001	0.726	-0.8	0.2
10:10 x 0:10	1.5	0.900	0.001	0.916	1.7	0.1
10:10 x 0:10	5	0.789	0.001	0.802	1.6	0.1
10:10 x 0:10	10	0.618	0.001	0.631	2.1	0.2

Table A-45: 6 MV 45°Virtual Wedge measured and CMS OFs

Field (X1:X2 x Y1:Y2)	Depth (cm)	OF Measured	±	OF CMS	ΔOF %	±
0:5 x 0:5	1.5	0.858	0.001	0.848	-1.2	0.1
0:5 x 0:5	5	0.733	0.001	0.728	-0.7	0.2
0:5 x 0:5	10	0.549	0.001	0.545	-0.8	0.2
0:5 x 5:5	1.5	0.988	0.001	0.975	-1.4	0.1
0:5 x 5:5	5	0.848	0.001	0.841	-0.9	0.1
0:5 x 5:5	10	0.642	0.001	0.636	-1.0	0.2
5:5 x 0:5	1.5	0.841	0.001	0.853	1.5	0.1
5:5 x 0:5	5	0.724	0.001	0.739	2.1	0.2
5:5 x 0:5	10	0.551	0.001	0.562	1.9	0.2
0:10 x 0:10	1.5	0.800	0.001	0.800	0.1	0.1
0:10 x 0:10	5	0.696	0.001	0.696	0.1	0.2
0:10 x 0:10	10	0.539	0.001	0.542	0.4	0.2
0:10 x 10:10	1.5	1.082	0.001	1.065	-1.6	0.1
0:10 x 10:10	5	0.941	0.001	0.928	-1.4	0.1
0:10 x 10:10	10	0.736	0.001	0.725	-1.5	0.2
10:10 x 0:10	1.5	0.802	0.001	0.814	1.4	0.1
10:10 x 0:10	5	0.705	0.001	0.715	1.5	0.2
10:10 x 0:10	10	0.555	0.001	0.566	1.9	0.2

Table A-46: 6 MV 60°Virtual Wedge measured and CMS OFs

Field (X1:X2 x Y1:Y2)	Depth (cm)	OF Measured	±	OF CMS	ΔOF %	±
0:5 x 0:5	1.5	0.773	0.001	0.771	-0.3	0.2
0:5 x 0:5	5	0.662	0.001	0.664	0.3	0.2
0.5 x 0:5	10	0.499	0.001	0.499	0.1	0.2
0:5 x 5:5	1.5	0.988	0.001	0.975	-1.4	0.1
0:5 x 5:5	5	0.847	0.001	0.841	-0.7	0.1
0:5 x 5:5	10	0.642	0.001	0.636	-1.0	0.2
5:5 x 0:5	1.5	0.756	0.001	0.776	2.5	0.2
5:5 x 0:5	5	0.654	0.001	0.674	3.2	0.2
5:5 x 0:5	10	0.500	0.001	0.515	3.1	0.2
0:10 x 0:10	1.5	0.653	0.001	0.658	0.9	0.2
0:10 x 0:10	5	0.571	0.001	0.577	1.0	0.2
0:10 x 0:10	10	0.448	0.001	0.453	1.0	0.3
0:10 x 10:10	1.5	1.104	0.001	1.066	-3.4	0.1
0:10 x 10:10	5	0.961	0.001	0.928	-3.4	0.1
0:10 x 10:10	10	0.753	0.001	0.725	-3.6	0.1
10:10 x 0:10	1.5	0.655	0.001	0.669	2.1	0.2
10:10 x 0:10	5	0.578	0.001	0.592	2.4	0.2
10:10 x 0:10	10	0.461	0.001	0.473	2.6	0.3

A.3 Isodose Distribution Evaluation Data

1 A.3.1 Low Gradient Central Beam Region

Table A-47: Evaluation Measurements of Measured and TMS Isodose Distributions in the Low Gradient Central Beam Region

Energy	Field	Plane	Isodose Line (%)			ΔL	
(MV)	(X1:X2 x Y1:Y2)		CMS	Measured	(±)	(%)	±
23	5:15 x 10:10	cross	120	119.5	0.3	0.4	0.3
23	5:15 x 10:10	in	120	119.4	0.3	0.5	0.3
23	0:10 x 10:10	cross	–				
23	0:10 x 10:10	in	120	119.8	0.2	0.2	0.2
23	10:0 x 10:10	cross	120	119.5	0.3	0.4	0.3
23	10:0 x 10:10	in	120	119.6	0.3	0.3	0.3
23	15:5 x 10:10	cross	120	119.3	0.3	0.6	0.3
23	15:5 x 10:10	in	120	119.1	0.3	0.8	0.3
6	5:15 x 10:10	cross	140	141.9	0.4	-1.3	0.3
6	5:15 x 10:10	in	140	142.0	0.4	-1.4	0.3
6	0:10 x 10:10	cross	140	142.7	0.4	-1.9	0.3
6	0:10 x 10:10	in	140	142.2	0.4	-1.5	0.3
6	10:0 x 10:10	cross	140	142.4	0.4	-1.7	0.3
6	10:0 x 10:10	in	140	142.1	0.4	-1.5	0.3
6	15:5 x 10:10	cross	140	142.3	0.4	-1.6	0.3
6	15:5 x 10:10	in	140	142.2	0.4	-1.5	0.3
23	Block6	cross	120	119.0	0.3	0.8	0.3
23	Block6	in	120	119.1	0.3	0.8	0.3
23	Block3	cross	120	119.6	0.3	0.3	0.3
23	Block3	in	120	119.6	0.3	0.3	0.3
6	Block6	cross	140	141.1	0.4	-0.8	0.3
6	Block6	in	140	141.1	0.4	-0.8	0.3
6	Block3	cross	–				
6	Block3	in	80	79.7	0.3	0.4	0.4
6	MLC3	cross	140	141.2	0.4	-0.8	0.3
6	MLC3	in	140	141.0	0.4	-0.7	0.3
6	MLC6	cross	140	140.8	0.4	-0.6	0.3
6	MLC6	in	140	140.3	0.4	-0.2	0.3
23	MLC3	cross	120	119.0	0.3	0.8	0.3
23	MLC3	in	120	119.1	0.3	0.8	0.3
23	MLC6	cross	120	118.6	0.3	1.2	0.3
23	MLC6	in	120	118.9	0.3	0.9	0.3

Table A-48: Evaluation Measurements of Measured and CMS Isodose Distributions in the Low Gradient Central Beam Region

Energy	Field	Plane	Isodose Line (%)			ΔL	
(MV)	(X1:X2 x Y1:Y2)		CMS	Measured	(±)	(%)	±
23	5:15 x 10:10	cross	–			0.0	
23	5:15 x 10:10	in	120	120.1	0.3	-0.1	0.2
23	0:10 x 10:10	cross	–			0.0	
23	0:10 x 10:10	in	–			0.0	
23	10:0 x 10:10	cross	120	119.6	0.3	0.3	0.3
23	10:0 x 10:10	in	120	119.5	0.3	0.4	0.3
23	15:5 x 10:10	cross	120	119.7	0.3	0.3	0.3
23	15:5 x 10:10	in	120	119.6	0.3	0.3	0.3
6	5:15 x 10:10	cross	80	80.6	0.3	-0.7	0.4
6	5:15 x 10:10	in	140	139.2	0.4	0.6	0.3
6	0:10 x 10:10	cross	120	120.9	0.4	-0.7	0.3
6	0:10 x 10:10	in	120	120.8	0.4	-0.7	0.3
6	10:0 x 10:10	cross	120	120.4	0.4	-0.3	0.3
6	10:0 x 10:10	in	80	80.3	0.3	-0.4	0.4
6	15:5 x 10:10	cross	120	120.6	0.4	-0.5	0.3
6	15:5 x 10:10	in	140	139.2	0.4	0.6	0.3
23	Block6	cross	120	119.7	0.2	0.3	0.2
23	Block6	in	–			0.0	
23	Block3	cross	–			0.0	
23	Block3	in	–			0.0	
6	Block6	cross	140	139.2	0.4	0.6	0.3
6	Block6	in	140	139.2	0.4	0.6	0.3
6	Block3	cross	140	138.5	0.4	0.0	0.3
6	Block3	in	140	138.6	0.4	1.0	0.3
6	MLC3	cross	140	139.6	0.4	0.3	0.3
6	MLC3	in	140	139.6	0.4	0.3	0.3
6	MLC6	cross	140	139.0	0.4	0.7	0.3
6	MLC6	in	140	138.9	0.4	0.8	0.3
23	MLC3	cross	120	119.5	0.3	0.4	0.3
23	MLC3	in	120	119.7	0.3	0.3	0.3
23	MLC6	cross	–			0.0	
23	MLC6	in	–			0.0	

A.3.2 Low Gradient Inner Beam Region

Table A-49: Evaluation Measurements of Measured and TMS 23MV Isodose Distributions in the Low Gradient Inner Beam Region

Field	Plane	Position	Isodose Line (%)			ΔL	
(X1:X2 x Y1:Y2)			TMS	Measured	(±)	(%)	±
5:15 x 10:10	Cross	R	120	121.6	0.3	-1.3	0.2
5:15 x 10:10	Cross	L	120	118.4	0.3	1.4	0.3
5:15 x 10:10	in	R	100	101.1	0.3	-1.1	0.3
5:15 x 10:10	in	L	120	119.2	0.3	0.7	0.3
0:10 x 10:10	Cross	R	120	119.1	0.3	0.8	0.3
0:10 x 10:10	Cross	L	120	120.6	0.3	-0.5	0.2
0:10 x 10:10	in	R	120	120.9	0.3	-0.7	0.2
0:10 x 10:10	in	L	80	78.9	0.3	1.4	0.4
10:0 x 10:10	Cross	R	120	118.8	0.3	1.0	0.3
10:0 x 10:10	Cross	L	80	79.2	0.3	1.0	0.4
10:0 x 10:10	in	R	120	119.1	0.3	0.8	0.3
10:0 x 10:10	in	L	120	120.9	0.3	-0.7	0.2
15:5 x 10:10	Cross	R	120	117.8	0.3	1.9	0.3
15:5 x 10:10	Cross	L	120	122.1	0.3	-1.7	0.2
15:5 x 10:10	in	R	100	101.1	0.3	-1.1	0.3
15:5 x 10:10	in	L	120	121.3	0.3	-1.1	0.2
Block6	cross	R	120	121.5	0.3	-1.2	0.2
Block6	cross	L	120	122.5	0.3	-2.0	0.2
Block6	in	R	120	121.8	0.3	-1.5	0.2
Block6	in	L	120	121.8	0.3	-1.5	0.2
Block3	cross	R	120	121.2	0.3	-1.0	0.2
Block3	cross	L	120	120.8	0.3	-0.7	0.2
Block3	in	R	120	119.0	0.3	0.8	0.3
Block3	in	L	100	97.9	0.3	2.1	0.3
MLC3	cross	R	100	101.3	0.3	-1.3	0.3
MLC3	cross	L	120	120.4	0.6	-0.3	0.5
MLC3	in	R	100	100.6	0.3	-0.6	0.3
MLC3	in	L	100	101.7	0.3	-1.7	0.3
MLC6	cross	R	120	122.0	0.3	-1.6	0.2
MLC6	cross	L	120	122.2	0.3	-1.8	0.2
MLC6	in	R	100	101.8	0.3	-1.8	0.3
MLC6	in	L	100	101.3	0.3	-1.3	0.3

Table A-50: Evaluation Measurements of Measured and TMS 6MV Isodose Distributions in the Low Gradient Inner Beam Region

Field (X1:X2 x Y1:Y2)	Plane	Position	Isodose Line (%)			ΔL	
			TMS	Measured	(±)	(%)	±
5:15 x 10:10	cross	R	140	144.3	0.4	-3.0	0.3
5:15 x 10:10	cross	L	120	121.6	0.3	-1.3	0.2
5:15 x 10:10	in	R	140	144.9	0.4	-3.4	0.3
5:15 x 10:10	in	L	140	144.1	0.4	-2.8	0.3
0:10 x 10:10	cross	R	80	82.5	0.4	-3.0	0.5
0:10 x 10:10	cross	L	140	142.9	0.4	-2.0	0.3
0:10 x 10:10	in	R	140	144.5	0.5	-3.1	0.3
0:10 x 10:10	in	L	140	142.7	0.4	-1.9	0.3
10:0 x 10:10	cross	R	140	142.4	0.4	-1.7	0.3
10:0 x 10:10	cross	L	140	142.1	0.4	-1.5	0.3
10:0 x 10:10	in	R	140	143.7	0.5	-2.6	0.3
10:0 x 10:10	in	L	140	143.6	0.5	-2.5	0.3
15:5 x 10:10	cross	R	120	121.8	0.4	-1.5	0.3
15:5 x 10:10	cross	L	140	145.7	0.4	-3.9	0.3
15:5 x 10:10	in	R	140	144.1	0.4	-2.8	0.3
15:5 x 10:10	in	L	140	143.6	0.4	-2.5	0.3
Block6	cross	R	140	141.7	0.4	-1.2	0.3
Block6	cross	L	140	142.5	0.4	-1.8	0.3
Block6	in	R	140	142.1	0.4	-1.5	0.3
Block6	in	L	140	142.4	0.4	-1.7	0.3
Block3	cross	R	80	78.7	0.3	1.7	0.4
Block3	cross	L	140	141.3	0.4	-0.9	0.3
Block3	in	R	140	141.1	0.4	-0.8	0.3
Block3	in	L	140	141.2	0.4	-0.8	0.3
MLC3	cross	R	140	141.8	0.4	-1.3	0.3
MLC3	cross	L	140	141.2	0.4	-0.8	0.3
MLC3	in	R	140	142.1	0.5	-1.5	0.3
MLC3	in	L	140	142.5	0.4	-1.8	0.3
MLC6	cross	R	140	142.5	0.4	-1.8	0.3
MLC6	cross	L	140	142.9	0.4	-2.0	0.3
MLC6	in	R	140	142.6	0.4	-1.8	0.3
MLC6	in	L	140	142.1	0.4	-1.5	0.3

Table A-51: Evaluation Measurements of Measured and CMS 23MV Isodose Distributions in the Low Gradient Inner Beam Region

Field	Plane	Position	Isodose Line (%)			ΔL	
(X1:X2 x Y1:Y2)			CMS	Measured	(±)	(%)	±
5:15 x 10:10	cross	R	120	120.6	0.3	-0.5	0.2
5:15 x 10:10	cross	L	100	97.9	0.2	2.1	0.2
5:15 x 10:10	in	R	120	120.9	0.3	-0.7	0.2
5:15 x 10:10	in	L	120	118.2	0.3	1.5	0.3
0:10 x 10:10	cross	R	100	99.5	0.2	0.5	0.2
0:10 x 10:10	cross	L	100	98.6	0.3	1.4	0.3
0:10 x 10:10	in	R	120	121.3	0.3	-1.1	0.2
0:10 x 10:10	in	L	120	118.5	0.3	1.3	0.3
10:0 x 10:10	cross	R	100	97.7	0.3	2.4	0.3
10:0 x 10:10	cross	L	120	119.6	0.3	0.3	0.3
10:0 x 10:10	in	R	120	120.7	0.3	-0.6	0.2
10:0 x 10:10	in	L	120	117.8	0.3	1.9	0.3
15:5 x 10:10	cross	R	100	97.1	0.3	3.0	0.3
15:5 x 10:10	cross	L	120	120.3	0.3	-0.2	0.2
15:5 x 10:10	in	R	120	119.1	0.3	0.8	0.3
15:5 x 10:10	in	L	120	118.0	0.3	1.7	0.3
Block6	cross	R	120	117.0	0.3	2.6	0.3
Block6	cross	L	120	118.1	0.3	1.6	0.3
Block6	in	R	100	101.1	0.3	-1.1	0.3
Block6	in	L	120	116.7	0.3	2.8	0.3
Block3	cross	R	120	118.2	0.3	1.5	0.3
Block3	cross	L	120	119.1	0.3	0.8	0.3
Block3	in	R	100	100.7	0.3	-0.7	0.3
Block3	in	L	120	117.9	0.3	1.8	0.3
MLC3	cross	R	120	118.7	0.4	1.1	0.3
MLC3	cross	L	120	118.9	0.3	0.9	0.3
MLC3	in	R	100	101.2	0.3	-1.2	0.3
MLC3	in	L	120	118.1	0.3	1.6	0.3
MLC6	cross	R	120	118.6	0.3	1.2	0.3
MLC6	cross	L	120	118.7	0.3	1.1	0.3
MLC6	in	R	100	101.2	0.3	-1.2	0.3
MLC6	in	L	120	118.4	0.3	1.4	0.3

Table A-52: Evaluation Measurements of Measured and CMS 6MV Isodose Distributions in the Low Gradient Inner Beam Region

Field	Plane	Position	Isodose Line (%)			ΔL	
(X1:X2 x Y1:Y2)			CMS	Measured	(±)	(%)	±
5:15 x 10:10	cross	R	120	120.8	0.4	-0.7	0.3
5:15 x 10:10	cross	L	120	117.1	0.4	2.5	0.4
5:15 x 10:10	in	R	140	137.5	0.4	1.8	0.3
5:15 x 10:10	in	L	140	136.8	0.4	2.3	0.3
0:10 x 10:10	cross	R	120	120.8	0.4	-0.7	0.3
0:10 x 10:10	cross	L	100	98.2	0.4	1.8	0.4
0:10 x 10:10	in	R	120	120.9	0.4	-0.7	0.3
0:10 x 10:10	in	L	140	137.2	0.5	2.0	0.4
10:0 x 10:10	cross	R	120	117.0	0.4	2.6	0.4
10:0 x 10:10	cross	L	140	139.1	0.4	0.6	0.3
10:0 x 10:10	in	R	140	139.1	0.4	0.6	0.3
10:0 x 10:10	in	L	140	138.1	0.5	1.4	0.4
15:5 x 10:10	cross	R	100	98.0	0.4	2.0	0.4
15:5 x 10:10	cross	L	120	121.4	0.4	-1.2	0.3
15:5 x 10:10	in	R	140	137.6	0.4	1.7	0.3
15:5 x 10:10	in	L	140	137.1	0.4	2.1	0.3
Block6	cross	R	140	137.9	0.4	1.5	0.3
Block6	cross	L	140	138.3	0.4	1.2	0.3
Block6	in	R	140	137.5	0.4	1.8	0.3
Block6	in	L	140	137.1	0.4	2.1	0.3
Block3	cross	R	140	137.8	0.4	1.6	0.3
Block3	cross	L	140	138.3	0.4	1.2	0.3
Block3	in	R	140	138.1	0.4	1.4	0.3
Block3	in	L	140	137.4	0.4	1.9	0.3
MLC3	cross	R	100	98.1	0.4	1.9	0.4
MLC3	cross	L	140	138.4	0.4	1.2	0.3
MLC3	in	R	100	99.0	0.3	1.0	0.3
MLC3	in	L	140	138.4	0.4	1.2	0.3
MLC6	cross	R	140	138.7	0.4	0.9	0.3
MLC6	cross	L	140	138.7	0.4	0.9	0.3
MLC6	in	R	140	138.7	0.4	0.9	0.3
MLC6	in	L	140	137.5	0.4	1.8	0.3

2 A.3.3 High Gradient Region

Table A-53: Evaluation Measurements of Measured and TMS 23MV Isodose Distributions in the High Gradient Region

Field (X1:X2 x Y1:Y2)	Plane	Position	Isodose Line %	Lateral Deviation (mm)	± (mm)
5:15 x 10:10	cross	R	80	1.9	0.7
5:15 x 10:10	cross	L	20	1.4	0.7
5:15 x 10:10	in	R	20	2.1	0.7
5:15 x 10:10	in	L	100	-1.9	0.7
0:10 x 10:10	cross	R	80	2.9	0.7
0:10 x 10:10	cross	L	100	2.1	0.7
0:10 x 10:10	in	R	20	2.6	0.7
0:10 x 10:10	in	L	100	-1.9	0.7
10:0 x 10:10	cross	R	80	2.1	0.7
10:0 x 10:10	cross	L	20	1.7	0.7
10:0 x 10:10	in	R	20	2.1	0.7
10:0 x 10:10	in	L	100	-1.7	0.7
15:5 x 10:10	cross	R	100	-0.9	0.7
15:5 x 10:10	cross	L	120	-2.1	0.7
15:5 x 10:10	in	R	20	2.9	0.7
15:5 x 10:10	in	L	100	-1.7	0.7
Block6	cross	R	120	-3.6	0.7
Block6	cross	L	100	2.1	0.7
Block6	in	R	20	2.9	0.7
Block6	in	L	80	1.7	0.7
Block3	cross	R	80	2.1	0.7
Block3	cross	L	80	1.4	0.7
Block3	in	R	100	1.3	0.7
Block3	in	L	80	1.7	0.7
MLC3	cross	R	20	1.1	0.7
MLC3	cross	L	120	1.4	0.7
MLC3	in	R	20	2.1	0.7
MLC3	in	L	20	1.0	0.7
MLC6	cross	R	120	-2.1	0.7
MLC6	cross	L	20	1.7	0.7
MLC6	in	R	20	3.6	0.7
MLC6	in	L	120	-1.4	0.7

Table A-54: Evaluation Measurements of Measured and TMS 6MV Isodose Distributions in the High Gradient Region

Field (X1:X2 x Y1:Y2)	Plane	Position	Isodose Line %	Lateral Deviation (mm)	± (mm)
5:15 x 10:10	cross	R	140	-3.4	0.7
5:15 x 10:10	cross	L	100	1.1	0.7
5:15 x 10:10	in	R	40	2.1	0.7
5:15 x 10:10	in	L	120	-1.7	0.7
0:10 x 10:10	cross	R	80	1.0	0.7
0:10 x 10:10	cross	L	20	1.0	0.7
0:10 x 10:10	in	R	140	-2.9	0.7
0:10 x 10:10	in	L	140	-2.9	0.7
10:0 x 10:10	cross	R	100	-1.7	0.7
10:0 x 10:10	cross	L	20	1.3	0.7
10:0 x 10:10	in	R	140	-2.1	0.7
10:0 x 10:10	in	L	140	-2.8	0.7
15:5 x 10:10	cross	R	120	-1.3	0.7
15:5 x 10:10	cross	L	100	3.6	0.7
15:5 x 10:10	in	R	20	1.4	0.7
15:5 x 10:10	in	L	120	-1.4	0.7
Block6	cross	R	140	-1.7	0.7
Block6	cross	L	100	3.1	0.7
Block6	in	R	140	-4.3	0.7
Block6	in	L	100	3.0	0.7
Block3	cross	R	20	-2.1	0.7
Block3	cross	L	80	2.9	0.7
Block3	in	R	80	2.6	0.7
Block3	in	L	80	2.9	0.7
MLC3	cross	R	20	1.6	0.7
MLC3	cross	L	100	1.9	0.7
MLC3	in	R	20	3.1	0.7
MLC3	in	L	80	1.7	0.7
MLC6	cross	R	100	1.4	0.7
MLC6	cross	L	100	2.9	0.7
MLC6	in	R	20	3.3	0.7
MLC6	in	L	80	1.1	0.7

Table A-55: Evaluation Measurements of Measured and CMS 23MV Isodose Distributions in the High Gradient Region

Field (X1:X2 x Y1:Y2)	Plane	Position	Isodose Line %	Lateral Deviation (mm)	± (mm)
5:15 x 10:10	cross	R	20	3.4	0.7
5:15 x 10:10	cross	L	20	4.3	0.7
5:15 x 10:10	in	R	20	3.6	0.7
5:15 x 10:10	in	L	20	3.4	0.7
0:10 x 10:10	cross	R	120	-3.6	0.7
0:10 x 10:10	cross	L	20	5.0	0.7
0:10 x 10:10	in	R	20	4.3	0.7
0:10 x 10:10	in	L	20	4.0	0.7
10:0 x 10:10	cross	R	20	4.1	0.7
10:0 x 10:10	cross	L	100	-4.3	0.7
10:0 x 10:10	in	R	20	4.3	0.7
10:0 x 10:10	in	L	20	3.6	0.7
15:5 x 10:10	cross	R	20	4.3	0.7
15:5 x 10:10	cross	L	100	-3.0	0.7
15:5 x 10:10	in	R	20	4.3	0.7
15:5 x 10:10	in	L	20	-3.1	0.7
Block6	cross	R	20	-2.9	0.7
Block6	cross	L	20	-2.9	0.7
Block6	in	R	20	-2.9	0.7
Block6	in	L	80	-2.4	0.7
Block3	cross	R	20	10.0	0.7
Block3	cross	L	20	10.0	0.7
Block3	in	R	20	8.9	0.7
Block3	in	L	20	8.6	0.7
MLC3	cross	R	20	8.6	0.7
MLC3	cross	L	20	8.9	0.7
MLC3	in	R	20	9.1	0.7
MLC3	in	L	20	7.9	0.7
MLC6	cross	R	20	-4.1	0.7
MLC6	cross	L	20	-3.1	0.7
MLC6	in	R	20	-3.1	0.7
MLC6	in	L	20	-3.1	0.7

Table A-56: Evaluation Measurements of Measured and CMS 6MV Isodose Distributions in the High Gradient Region

Field (X1:X2 x Y1:Y2)	Plane	Position	Isodose Line %	Lateral Deviation (mm)	± (mm)
5:15 x 10:10	cross	R	20	2.9	0.7
5:15 x 10:10	cross	L	20	3.6	0.7
5:15 x 10:10	in	R	20	3.1	0.7
5:15 x 10:10	in	L	120	-1.9	0.7
0:10 x 10:10	cross	R	140	-4.0	0.7
0:10 x 10:10	cross	L	20	3.6	0.7
0:10 x 10:10	in	R	20	3.5	0.7
0:10 x 10:10	in	L	120	-2.0	0.7
10:0 x 10:10	cross	R	20	3.3	0.7
10:0 x 10:10	cross	L	120	-3.1	0.7
10:0 x 10:10	in	R	20	3.4	0.7
10:0 x 10:10	in	L	120	-1.7	0.7
15:5 x 10:10	cross	R	20	3.9	0.7
15:5 x 10:10	cross	L	80	-2.9	0.7
15:5 x 10:10	in	R	20	3.1	0.7
15:5 x 10:10	in	L	120	-1.7	0.7
Block6	cross	R	140	-4.3	0.7
Block6	cross	L	20	3.6	0.7
Block6	in	R	20	-2.9	0.7
Block6	in	L	20	-3.6	0.7
Block3	cross	R	20	7.0	0.7
Block3	cross	L	20	7.9	0.7
Block3	in	R	20	7.0	0.7
Block3	in	L	20	7.0	0.7
MLC3	cross	R	20	8.9	0.7
MLC3	cross	L	20	8.6	0.7
MLC3	in	R	20	8.4	0.7
MLC3	in	L	20	6.9	0.7
MLC6	cross	R	20	-2.9	0.7
MLC6	cross	L	20	-2.4	0.7
MLC6	in	R	20	-2.9	0.7
MLC6	in	L	20	-2.9	0.7

A.3.4 Penumbra Region

Table A-57: Evaluation Measurements of Measured and TMS 23MV Isodose Distributions in the Penumbra Region

Field (X1:X2 x Y1:Y2)	Plane	Position	Penumbra (cm) ± 0.07 TMS	Measured	Deviation (mm)	± (mm)
5:15 x 10:10	cross	R	1.14	1.14	0	1
5:15 x 10:10	cross	L	1.07	1.07	0	1
5:15 x 10:10	in	R	1.36	1.14	2	1
5:15 x 10:10	in	L	1.36	1.21	2	1
0:10 x 10:10	cross	R	1.14	1.07	1	1
0:10 x 10:10	cross	L	1.14	1.11	0	1
0:10 x 10:10	in	R	1.29	1.07	2	1
0:10 x 10:10	in	L	1.36	1.16	2	1
10:0 x 10:10	cross	R	1.20	1.11	1	1
10:0 x 10:10	cross	L	1.07	1.30	-2	1
10:0 x 10:10	in	R	1.31	1.09	2	1
10:0 x 10:10	in	L	1.36	1.16	2	1
15:5 x 10:10	cross	R	1.16	1.07	1	1
15:5 x 10:10	cross	L	1.11	--		1
15:5 x 10:10	in	R	1.39	1.13	3	1
15:5 x 10:10	in	L	1.43	1.23	2	1
Block6	cross	R	1.03	1.03	0	1
Block6	cross	L	0.91	1.00	-1	1
Block6	in	R	1.31	0.97	3	1
Block6	in	L	0.86	0.94	-1	1
Block3	cross	R	0.89	1.00	-1	1
Block3	cross	L	0.89	0.97	-1	1
Block3	in	R	0.89	0.89	0	1
Block3	in	L	0.86	0.93	-1	1
MLC3	cross	R	1.00	1.00	0	1
MLC3	cross	L	1.07	1.00	1	1
MLC3	in	R	1.36	1.04	3	1
MLC3	in	L	1.07	1.00	1	1
MLC6	cross	R	1.07	1.01	1	1
MLC6	cross	L	1.14	1.01	1	1
MLC6	in	R	1.29	1.00	3	1
MLC6	in	L	1.06	1.03	0	1

Table A-58: Evaluation Measurements of Measured and TMS 6MV Isodose Distributions in the Penumbra Region

Field (X1:X2 x Y1:Y2)	Plane	Position	Penumbra (cm) ± 0.07		Deviation (mm)	± (mm)
			TMS	Measured		
5:15 x 10:10	cross	R	1.11	1.13	0	1
5:15 x 10:10	cross	L	1.14	1.03	1	1
5:15 x 10:10	in	R	1.40	1.17	2	1
5:15 x 10:10	in	L	1.36	1.31	1	1
0:10 x 10:10	cross	R	1.06	0.97	1	1
0:10 x 10:10	cross	L	1.14	1.00	1	1
0:10 x 10:10	in	R	1.29	1.10	2	1
0:10 x 10:10	in	L	1.29	1.21	1	1
10:0 x 10:10	cross	R	1.10	1.00	1	1
10:0 x 10:10	cross	L	1.07	0.99	1	1
10:0 x 10:10	in	R	1.29	1.08	2	1
10:0 x 10:10	in	L	1.29	1.20	1	1
15:5 x 10:10	cross	R	1.14	1.00	1	1
15:5 x 10:10	cross	L	1.11	1.07	0	1
15:5 x 10:10	in	R	1.40	1.17	2	1
15:5 x 10:10	in	L	1.36	1.30	1	1
Block6	cross	R	1.01	1.00	0	1
Block6	cross	L	0.71	1.00	-3	1
Block6	in	R	1.30	1.00	3	1
Block6	in	L	0.67	1.00	-3	1
Block3	cross	R	0.70	0.86	-2	1
Block3	cross	L	0.83	0.86	0	1
Block3	in	R	0.83	0.83	0	1
Block3	in	L	0.83	0.86	0	1
MLC3	cross	R	1.00	1.00	0	1
MLC3	cross	L	1.07	0.97	1	1
MLC3	in	R	1.31	0.94	4	1
MLC3	in	L	0.93	0.99	-1	1
MLC6	cross	R	1.00	1.00	0	1
MLC6	cross	L	1.01	1.01	0	1
MLC6	in	R	1.31	1.01	3	1
MLC6	in	L	1.09	1.04	1	1

Table A-59: Evaluation Measurements of Measured and CMS 23MV Isodose Distributions in the Penumbra Region

Field (X1:X2 x Y1:Y2)	Plane	Position	Penumbra (cm) ± 0.07		Deviation (mm)	± (mm)
			CMS	Measured		
5:15 x 10:10	cross	R	1.69	1.14	6	1
5:15 x 10:10	cross	L	1.69	1.07	6	1
5:15 x 10:10	in	R	1.64	1.14	5	1
5:15 x 10:10	in	L	1.66	1.21	5	1
0:10 x 10:10	cross	R	1.57	1.07	5	1
0:10 x 10:10	cross	L	1.74	1.11	6	1
0:10 x 10:10	in	R	1.64	1.07	6	1
0:10 x 10:10	in	L	1.71	1.16	6	1
10:0 x 10:10	cross	R	1.71	1.11	6	1
10:0 x 10:10	cross	L	1.62	1.30	3	1
10:0 x 10:10	in	R	1.64	1.09	6	1
10:0 x 10:10	in	L	1.71	1.16	6	1
15:5 x 10:10	cross	R	1.57	1.07	5	1
15:5 x 10:10	cross	L	1.64	–		1
15:5 x 10:10	in	R	1.64	1.13	5	1
15:5 x 10:10	in	L	1.64	1.23	4	1
Block6	cross	R	0.93	1.03	-1	1
Block6	cross	L	1.00	1.00	0	1
Block6	in	R	0.93	0.97	0	1
Block6	in	L	0.97	0.94	0	1
Block3	cross	R	1.86	1.00	9	1
Block3	cross	L	1.89	0.97	9	1
Block3	in	R	1.79	0.89	9	1
Block3	in	L	1.84	0.93	9	1
MLC3	cross	R	1.86	1.00	9	1
MLC3	cross	L	1.89	1.00	9	1
MLC3	in	R	1.79	1.04	8	1
MLC3	in	L	1.84	1.00	8	1
MLC6	cross	R	0.93	1.01	-1	1
MLC6	cross	L	1.00	1.01	0	1
MLC6	in	R	0.93	1.00	-1	1
MLC6	in	L	0.97	1.03	-1	1

Table A-60: Evaluation Measurements of Measured and CMS 6MV Isodose Distributions in the Penumbra Region

Field (X1:X2 x Y1:Y2)	Plane	Position	Penumbra (cm) ± 0.07		Deviation (mm)	± (mm)
			CMS	Measured		
5:15 x 10:10	cross	R	1.50	1.14	4	1
5:15 x 10:10	cross	L	1.50	1.04	5	1
5:15 x 10:10	in	R	1.50	1.17	3	1
5:15 x 10:10	in	L	1.46	1.31	2	1
0:10 x 10:10	cross	R	1.43	0.90	5	1
0:10 x 10:10	cross	L	1.50	1.00	5	1
0:10 x 10:10	in	R	1.43	1.10	3	1
0:10 x 10:10	in	L	1.70	1.21	5	1
10:0 x 10:10	cross	R	1.50	1.00	5	1
10:0 x 10:10	cross	L	1.43	0.99	4	1
10:0 x 10:10	in	R	1.44	1.08	4	1
10:0 x 10:10	in	L	1.46	1.20	3	1
15:5 x 10:10	cross	R	1.53	1.00	5	1
15:5 x 10:10	cross	L	1.50	1.07	4	1
15:5 x 10:10	in	R	1.50	1.17	3	1
15:5 x 10:10	in	L	1.46	1.30	2	1
Block6	cross	R	0.93	1.00	-1	1
Block6	cross	L	0.90	1.00	-1	1
Block6	in	R	0.89	1.00	-1	1
Block6	in	L	0.86	1.00	-1	1
Block3	cross	R	1.61	0.86	8	1
Block3	cross	L	1.61	0.86	8	1
Block3	in	R	1.57	0.83	7	1
Block3	in	L	1.57	0.86	7	1
MLC3	cross	R	1.61	1.00	6	1
MLC3	cross	L	1.61	0.97	6	1
MLC3	in	R	1.57	0.94	6	1
MLC3	in	L	1.57	0.99	6	1
MLC6	cross	R	0.89	1.00	-1	1
MLC6	cross	L	0.89	1.01	-1	1
MLC6	in	R	0.86	1.01	-2	1
MLC6	in	L	0.86	1.04	-2	1

B. Appendix B

Graphical display (excluding frequency distributions) of the majority of the results provided in Appendix A are given in the following.

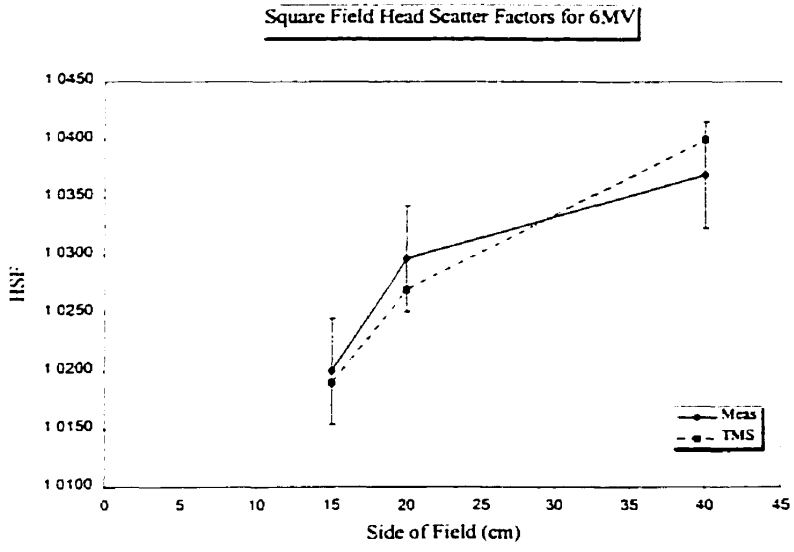

Figure B-1: Plot of measured and calculated square field HSFs for 6MV photons. Measurements were made on Siemens dual energy linear accelerator at the centre of the field. Calculations were performed on helax TMS treatment planning system.

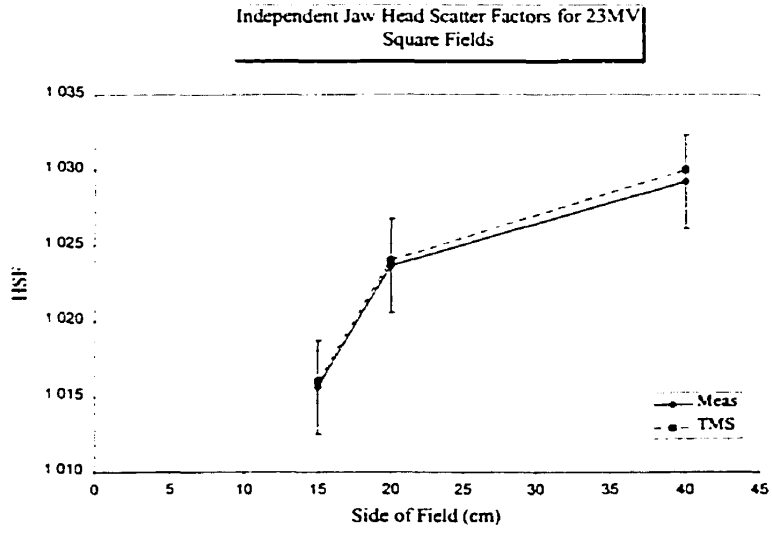

Figure B-2: Plot of measured and calculated square field HSFs for 23MV photons. Measurements were made on Siemens dual energy linear accelerator at the centre of the field. Calculations were performed on helax TMS treatment planning system.

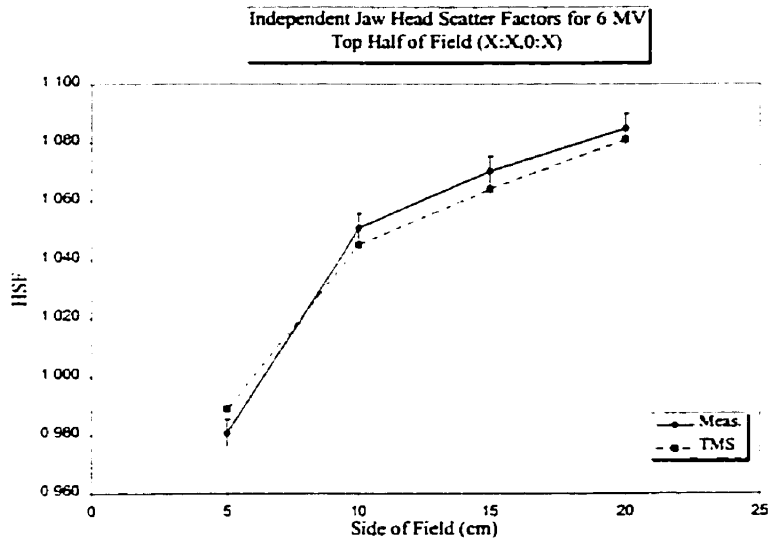

Figure B-3: Plot of 6MV asymmetric field HSFs for the top half of the field versus the dimensions of the side of the field, X. The abscissa is the value of X used in the title to define the field size. Measurements were made on Siemens dual energy accelerator at the centre of the field. Calculations were performed on Helax TMS treatment planning system.

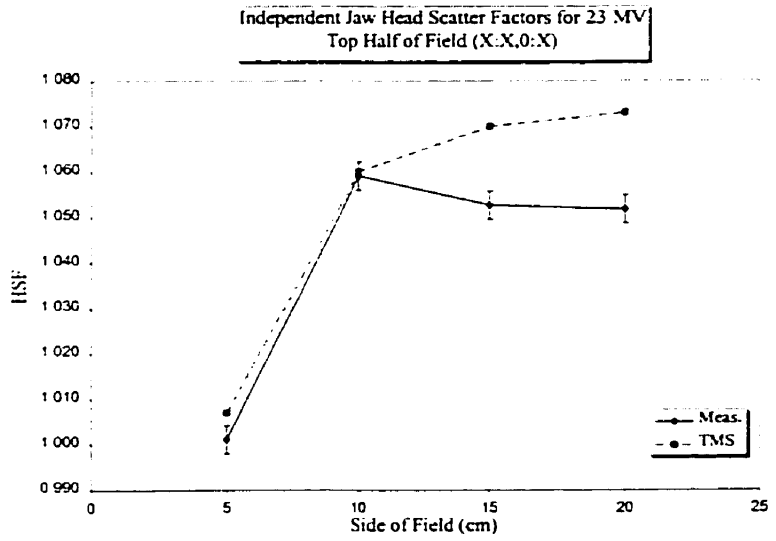

Figure B-4:Plot of the 23MV asymmetric field HSFs for the top half of the field versus the dimension of the side of the field, X. The abscissa is the value of X used in the title to define the field size. Measurements were made on Siemens dual energy linear accelerator at the centre of the field. Calculations were performed on Helax-TMS treatment planning system.

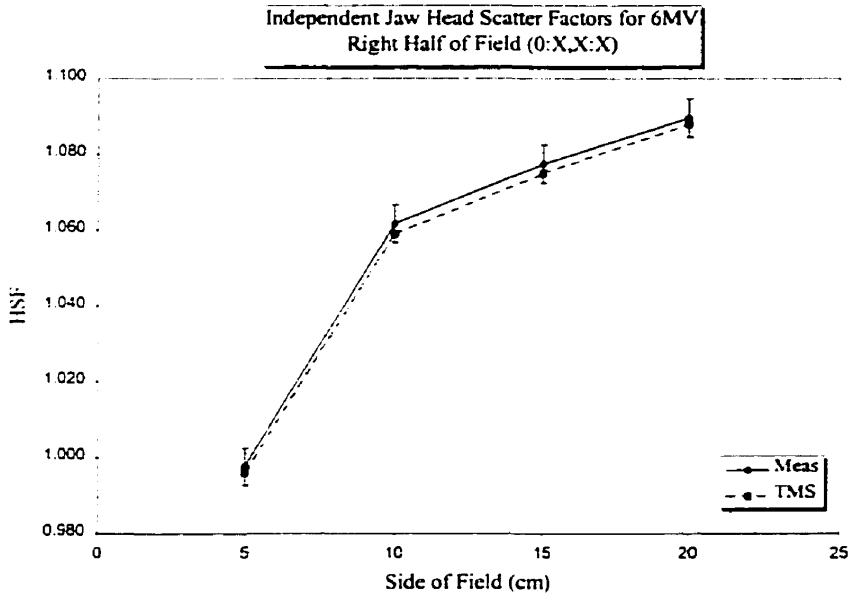

Figure B-5: Plot of the 6MV asymmetric field HSFs for the right half of the field versus the dimension of the side of the field, X. The abscissa is the value of X used in the title to define the field size. Measurements were made on Siemens dual energy linear accelerator at the centre of the field. Calculations were performed on Helax-TMS treatment planning system.

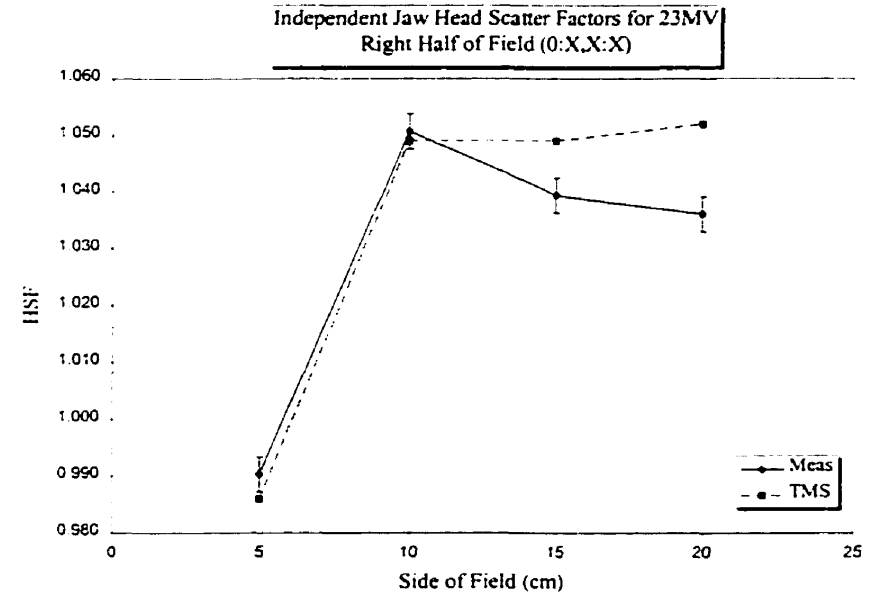

Figure B-6: Plot of the 23MV asymmetric field HSFs for the right half of the field versus the dimension of the side of the field, X. The abscissa is the value of X used in the title to define the field size. Measurements were made on Siemens dual energy linear accelerator at the centre of the field. Calculations were performed on Helax-TMS treatment planning system.

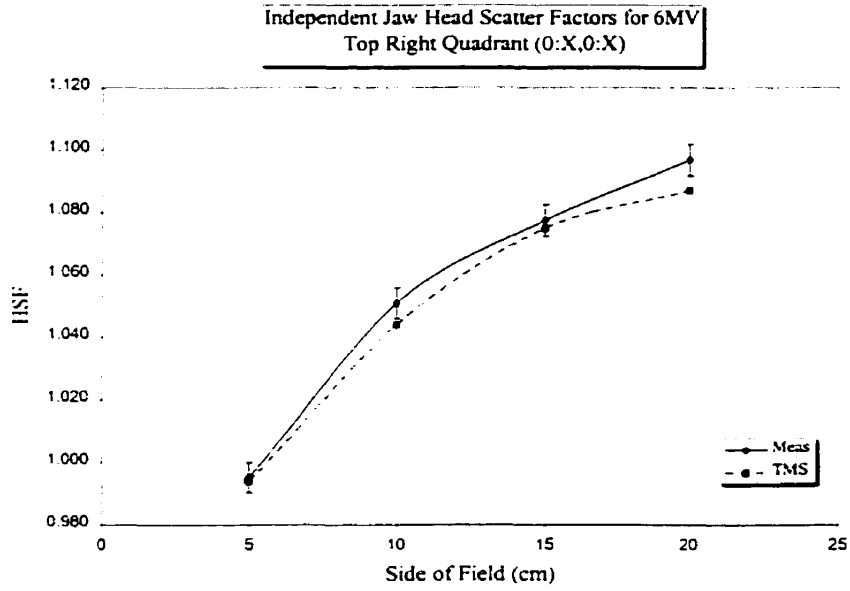

Figure B-7: Plot of the 6MV asymmetric field HSFs for the top right quadrant of the field versus the dimension of the side of the field, X. The abscissa is the value of X used in the title to define the field size. Measurements were made on Siemens dual energy linear accelerator at the centre of the field. Calculations were performed on Helax-TMS treatment planning system.

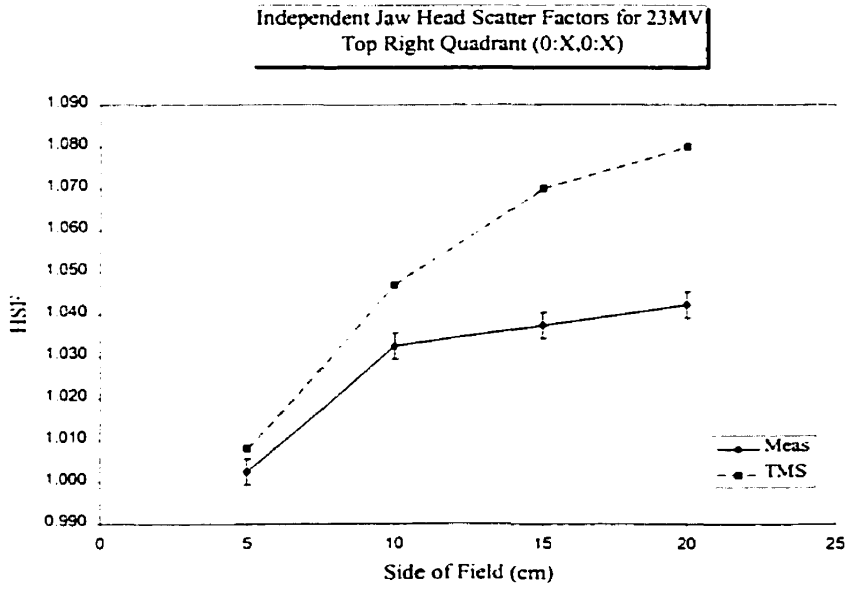

Figure B-8: Plot of the 23MV asymmetric field HSFs for the top right quadrant of the field versus the dimension of the side of the field, X. The abscissa is the value of X used in the title to define the field size. Measurements were made on Siemens dual energy linear accelerator at the centre of the field. Calculations were performed on Helax-TMS treatment planning system.

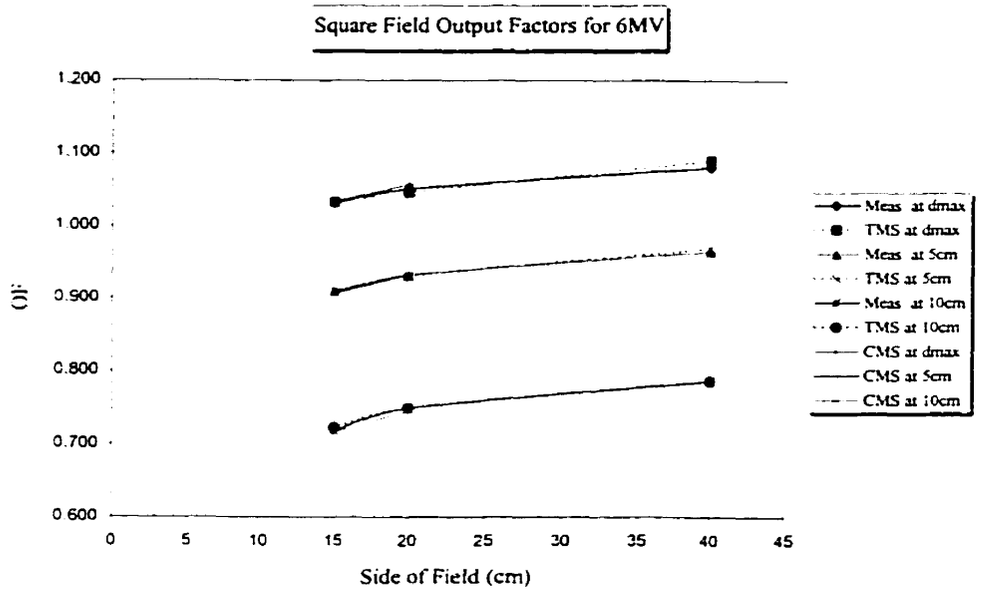

Figure B-9: Output factors for 6MV square fields. The output is determined in-phantom relative to the output for a 10x10 field at dmax. Measurements were made on Siemens dual energy linear accelerator at the centre of the field. Calculations were performed on Helax TMS and CMS-Focus.

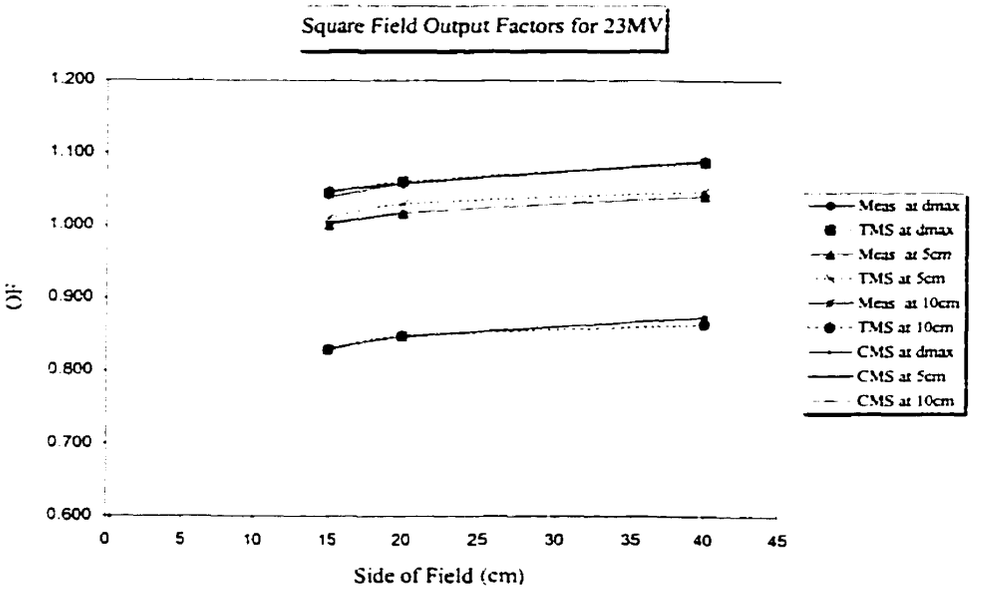

Figure B-10: Output factors for 23MV square fields. The output is determined in-phantom relative to the output for a 10x10 field at dmax. Measurements were made on Siemens dual energy linear accelerator at the centre of the field. Calculations were performed on Helax TMS and CMS-Focus.

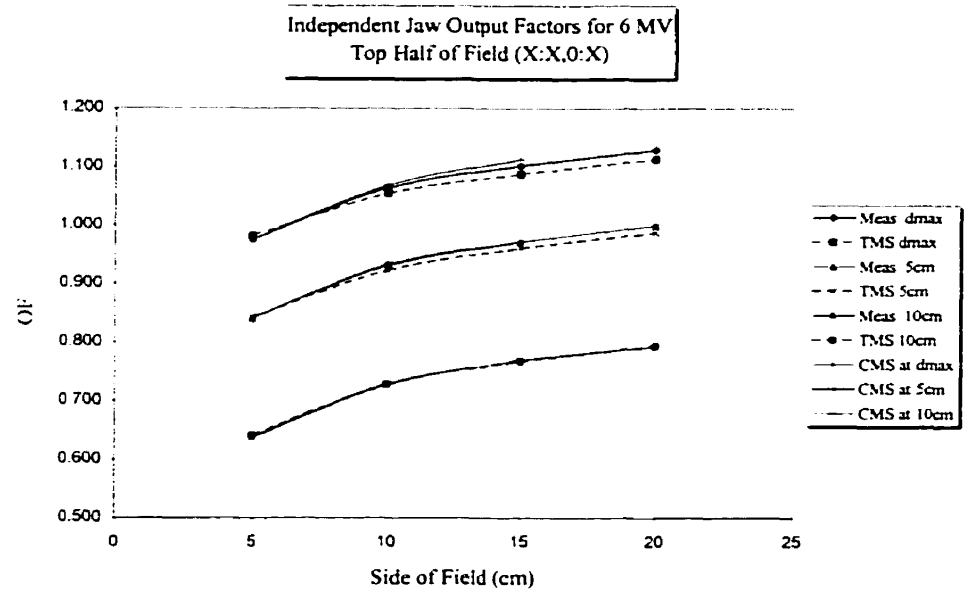

Figure B-11: 6MV asymmetric field output factors for the top half of the field. The output is determined in-phantom relative to the output for a 10x10 field at dmax. Measurements were made on Siemens dual energy linear accelerator at the centre of the field. Calculations were performed on Helax TMS and CMS-Focus.

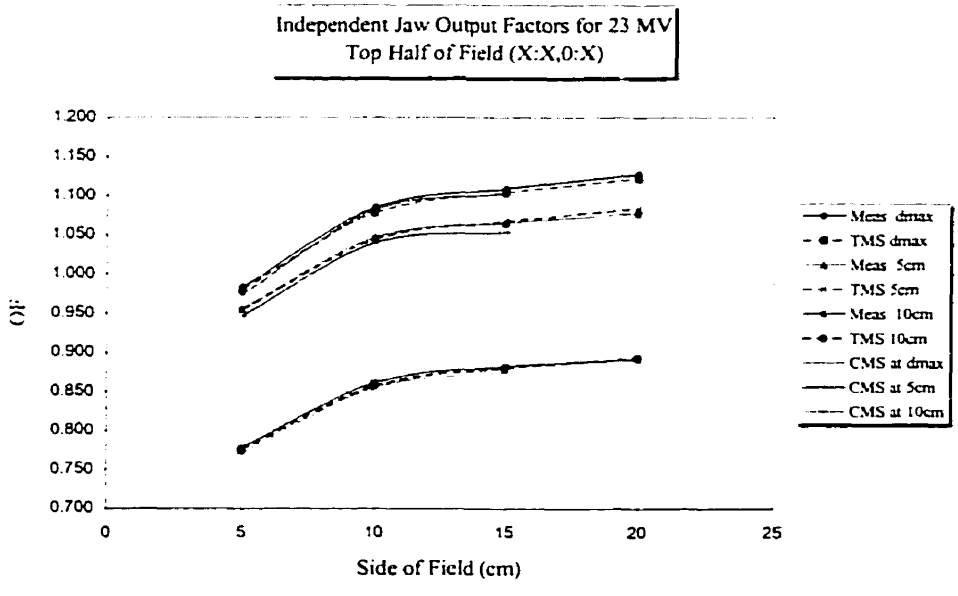

Figure B-12: 23MV asymmetric field output factors for the top half of the field. The output is determined in-phantom relative to the output for a 10x10 field at dmax. Measurements were made on Siemens dual energy linear accelerator at the centre of the field. Calculations were performed on Helax TMS and CMS-Focus.

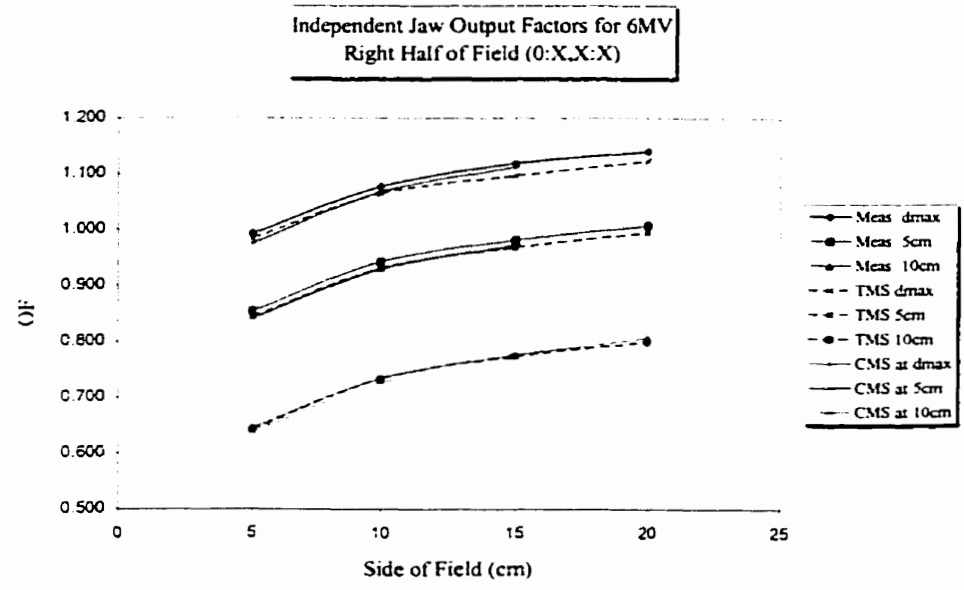

Figure B-13: 6MV asymmetric field output factors for the right half of the field. The output is determined in-phantom relative to the output for a 10x10 field at dmax. Measurements were made on Siemens dual energy linear accelerator at the centre of the field. Calculations were performed on Helax TMS and CMS-Focus.

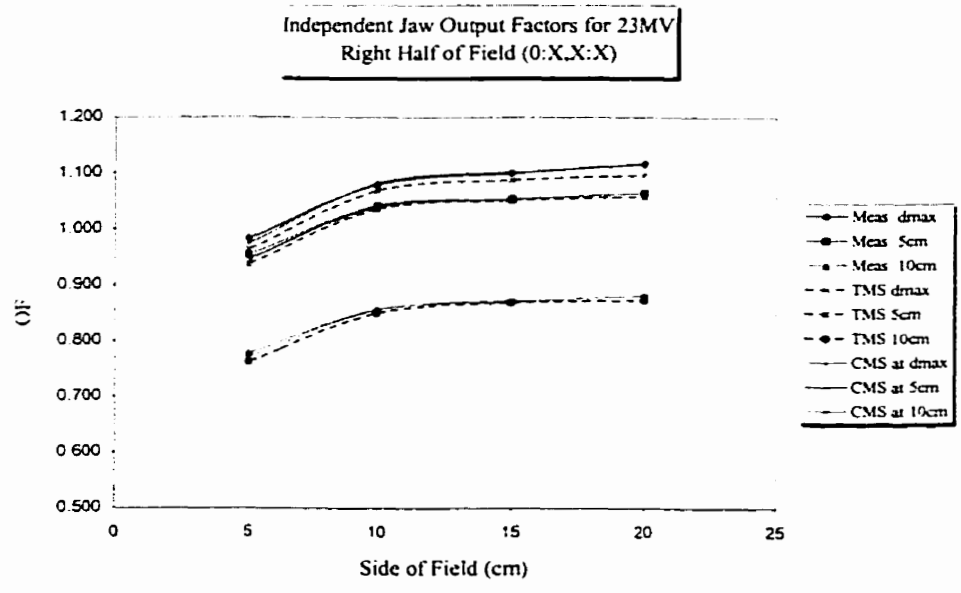

Figure B-14: 23MV asymmetric field output factors for the right half of the field. The output is determined in-phantom relative to the output for a 10x10 field at dmax. Measurements were made on Siemens dual energy linear accelerator at the centre of the field. Calculations were performed on Helax TMS and CMS-Focus.

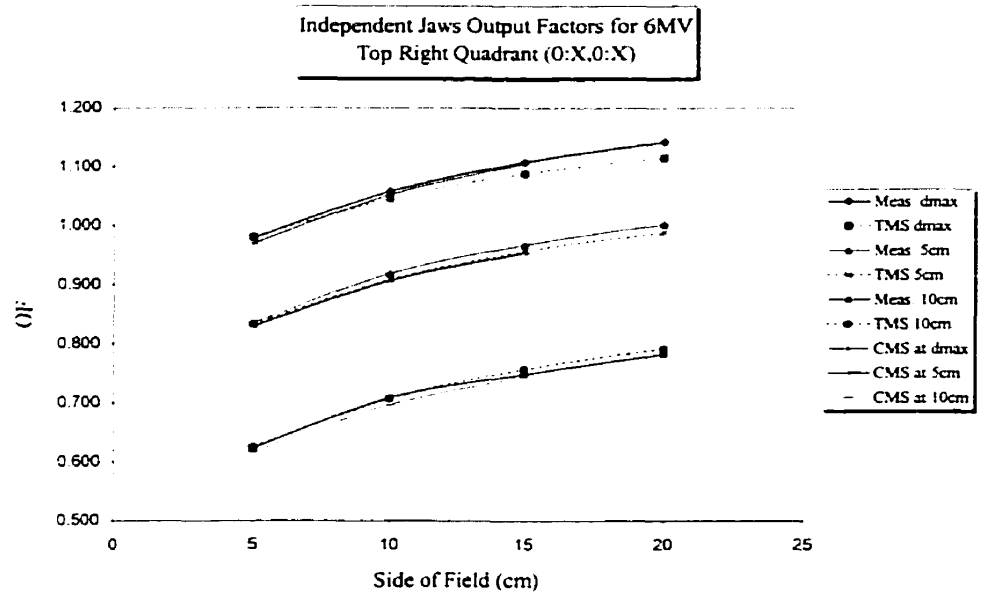

Figure B-15: 6MV asymmetric field output factors for the top right quadrant of the field. The output is determined in-phantom relative to the output for a 10x10 field at dmax. Measurements were made on Siemens dual energy linear accelerator at the centre of the field. Calculations were performed on Helax TMS and CMS-Focus.

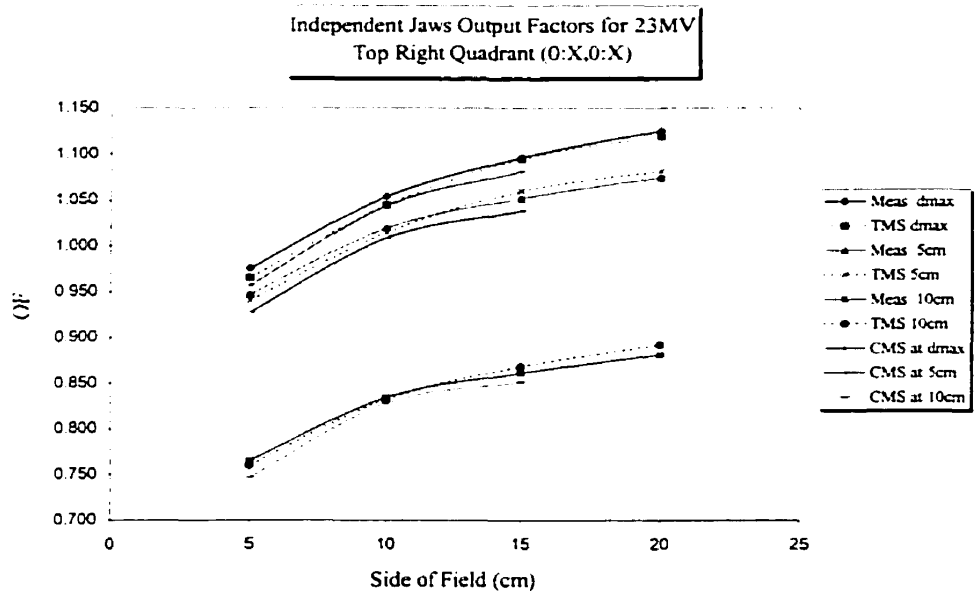

Figure B-16: 23MV asymmetric field output factors for the top right quadrant of the field. The output is determined in-phantom relative to the output for a 10x10 field at dmax. Measurements were made on Siemens dual energy linear accelerator at the centre of the field. Calculations were performed on Helax TMS and CMS-Focus.

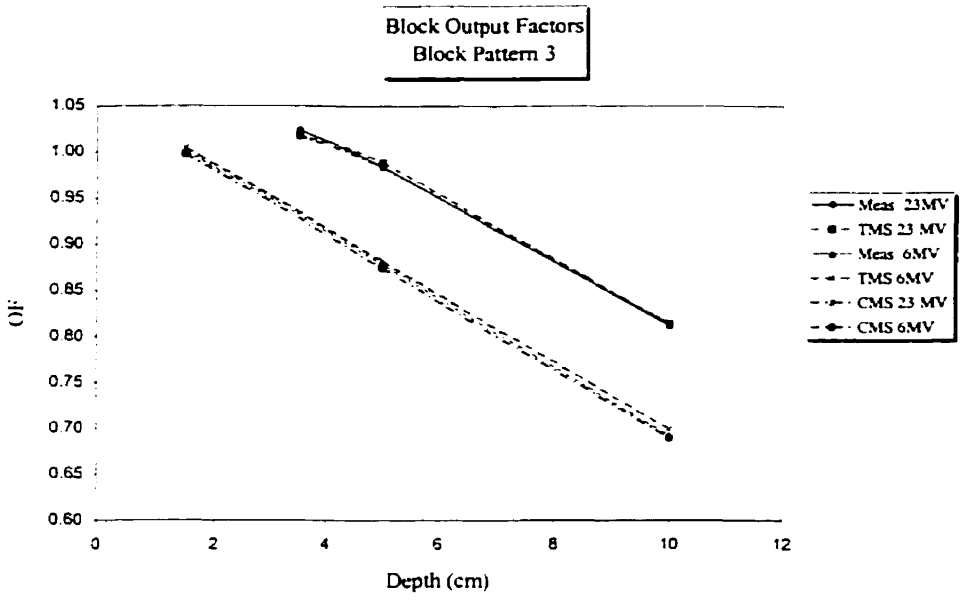

Figure B-17: Output factors for 6MV and 23 MV blocked field pattern 3. The output is determined in-phantom relative to the output for a 10x10 field at dmax. Measurements were made on Siemens dual energy linear accelerator at the centre of the field. Calculations were performed on Helax TMS and CMS-focus.

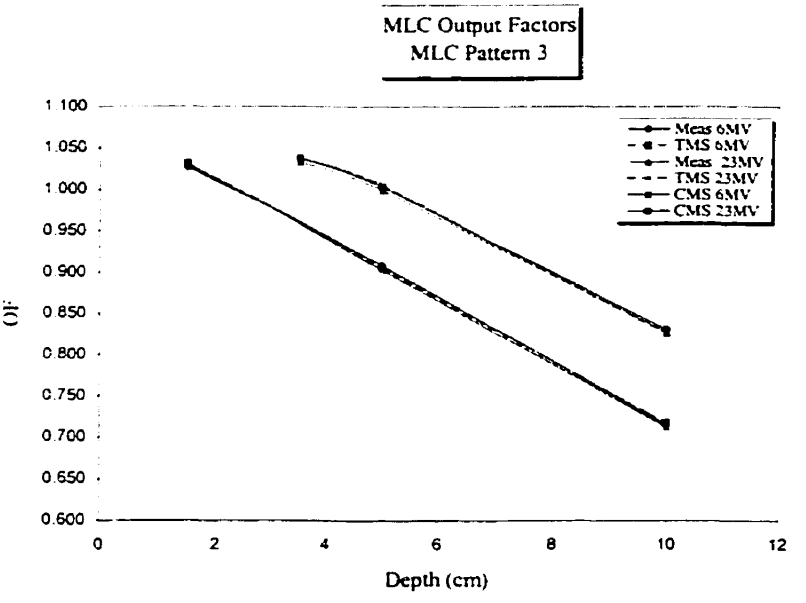

Figure B-18: Output factors for 6MV and 23 MV MLC shaped field (pattern 3). The output is determined in-phantom relative to the output for a 10x10 field at dmax. Measurements were made on Siemens dual energy linear accelerator at the centre of the field. Calculations were performed on Helax TMS and CMS-focus.

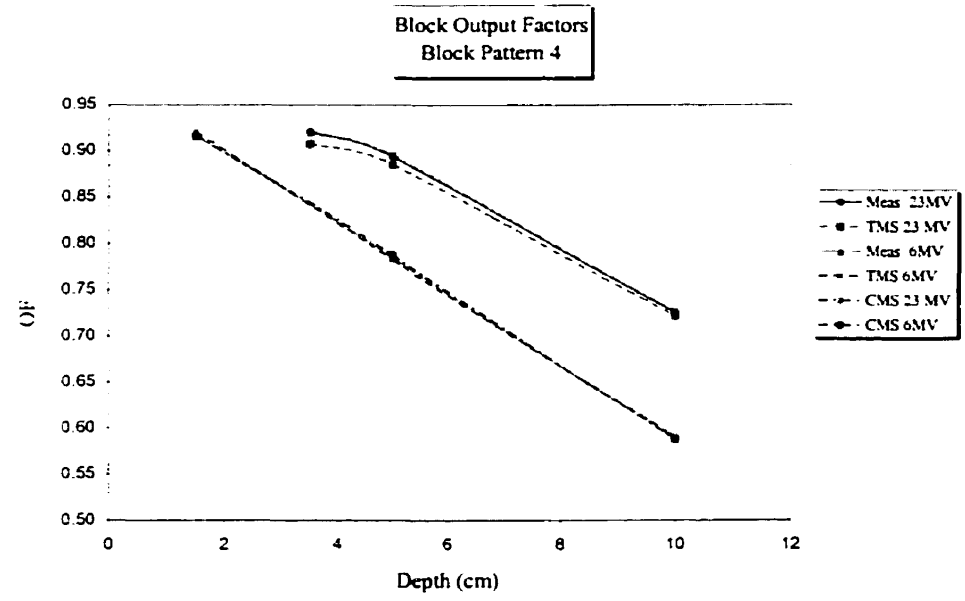

Figure B-19: Output factors for 6MV and 23 MV blocked field pattern 4. The output is determined in-phantom relative to the output for a 10x10 field at dmax. Measurements were made on Siemens dual energy linear accelerator at the centre of the field. Calculations were performed on Helax TMS and CMS-focus.

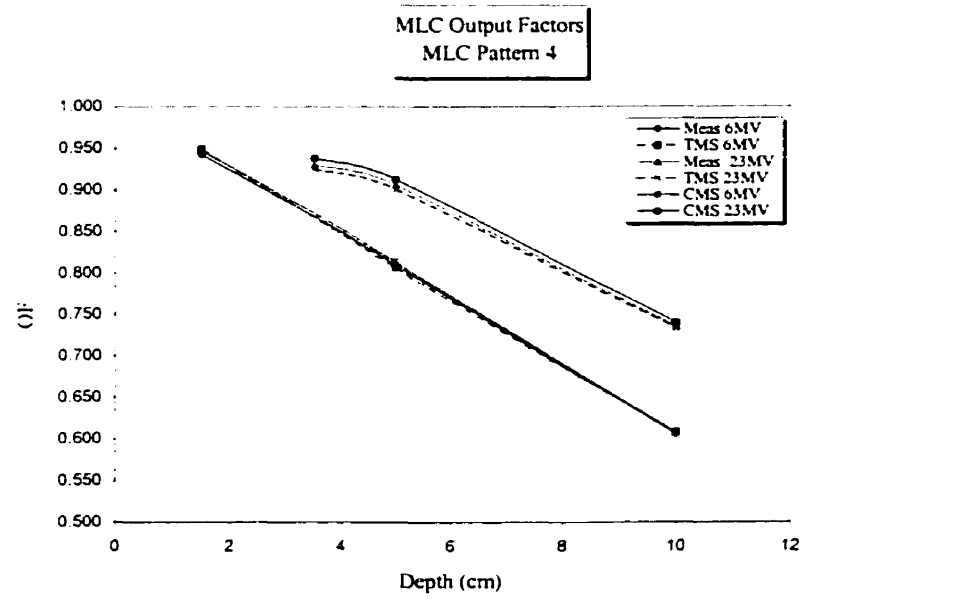

Figure B-20: Output factors for 6MV and 23 MV MLC shaped field (pattern 4). The output is determined in-phantom relative to the output for a 10x10 field at dmax. Measurements were made on Siemens dual energy linear accelerator at the centre of the field. Calculations were performed on Helax TMS and CMS-focus.

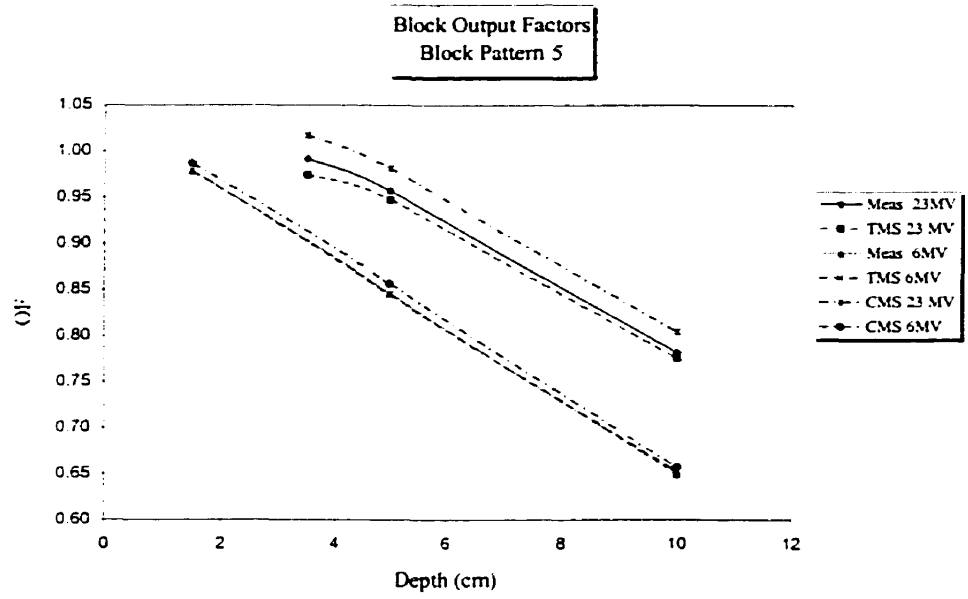

Figure B-21: Output factors for 6MV and 23 MV blocked field pattern 5. The output is determined in-phantom relative to the output for a 10x10 field at dmax. Measurements were made on Siemens dual energy linear accelerator at the centre of the field. Calculations were performed on Helax TMS and CMS-focus.

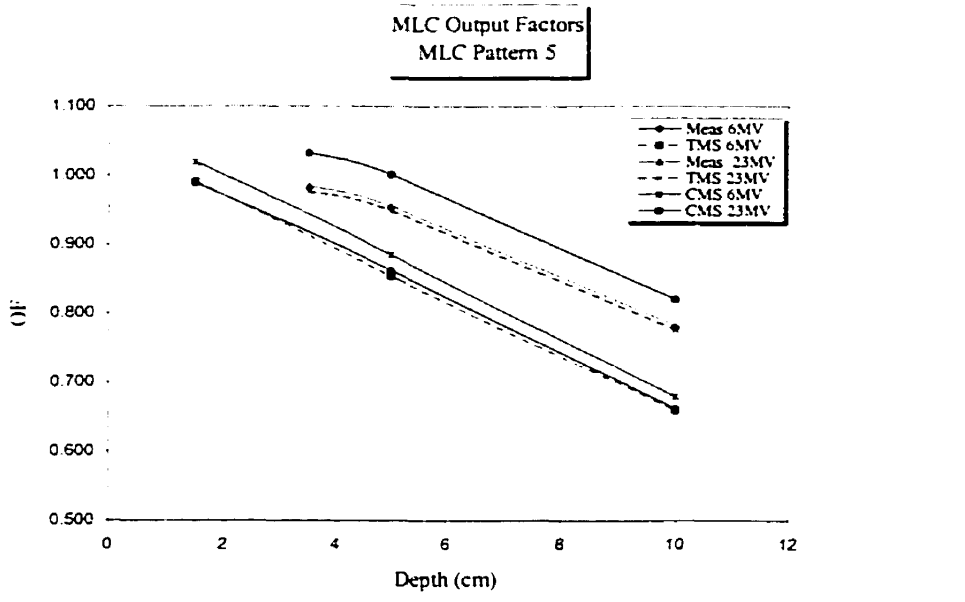

Figure B-22: Output factors for 6MV and 23 MV MLC shaped field (pattern 5). The output is determined in-phantom relative to the output for a 10x10 field at dmax. Measurements were made on Siemens dual energy linear accelerator at the centre of the field. Calculations were performed on Helax TMS and CMS-focus.

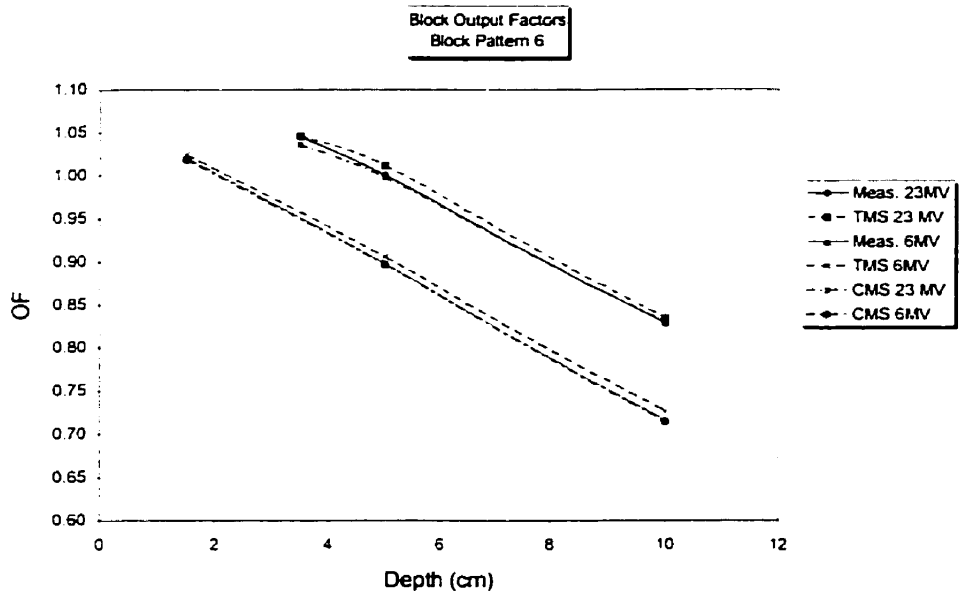

Figure B-23: Output factors for 6MV and 23 MV blocked field pattern 6. The output is determined in-phantom relative to the output for a 10x10 field at dmax. Measurements were made on Siemens dual energy linear accelerator at the centre of the field. Calculations were performed on Helax TMS and CMS-focus.

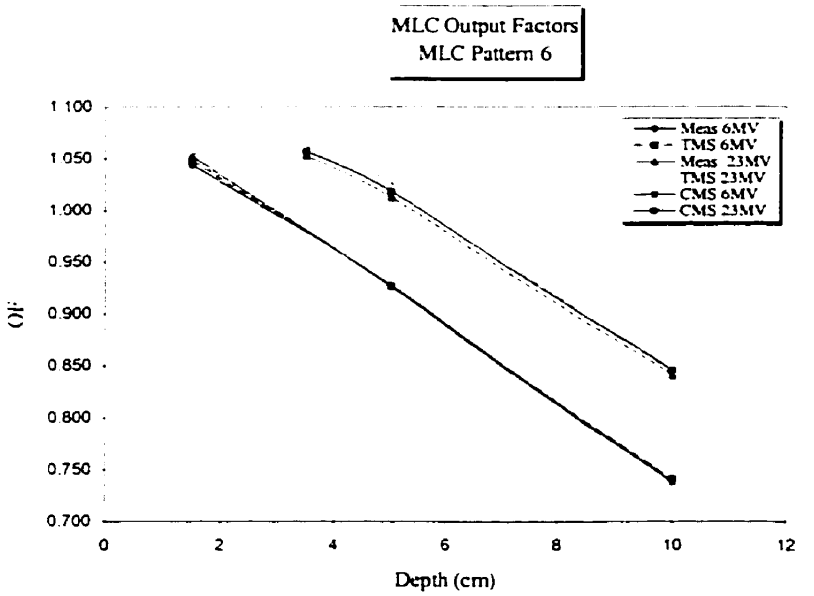

Figure B-24: Output factors for 6MV and 23 MV MLC shaped field (pattern 6). The output is determined in-phantom relative to the output for a 10x10 field at dmax. Measurements were made on Siemens dual energy linear accelerator at the centre of the field. Calculations were performed on Helax TMS and CMS-focus.

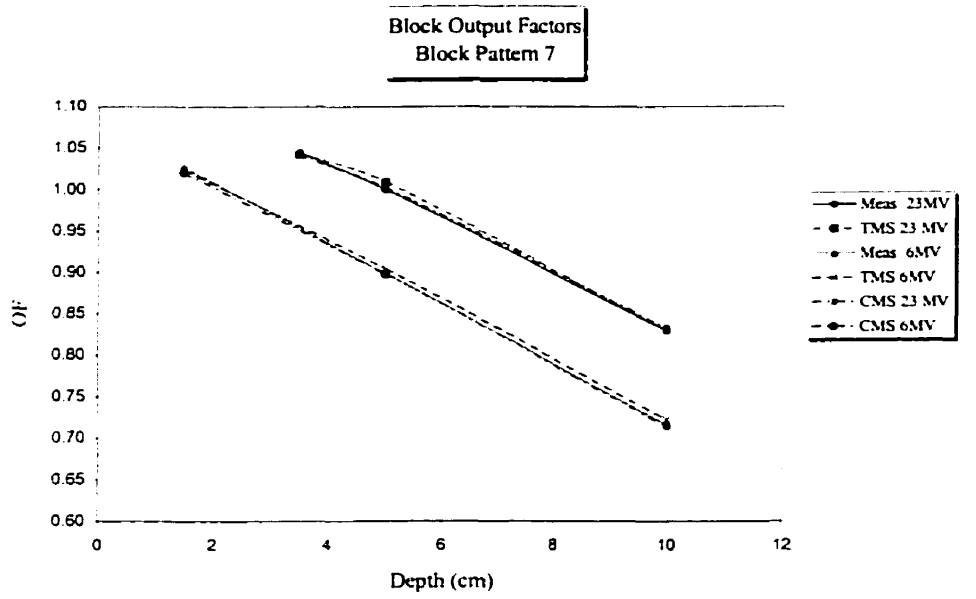

Figure B-25: Output factors for 6MV and 23 MV blocked field pattern 7. The output is determined in-phantom relative to the output for a 10x10 field at dmax. Measurements were made on Siemens dual energy linear accelerator at the centre of the field. Calculations were performed on Helax TMS and CMS-focus.

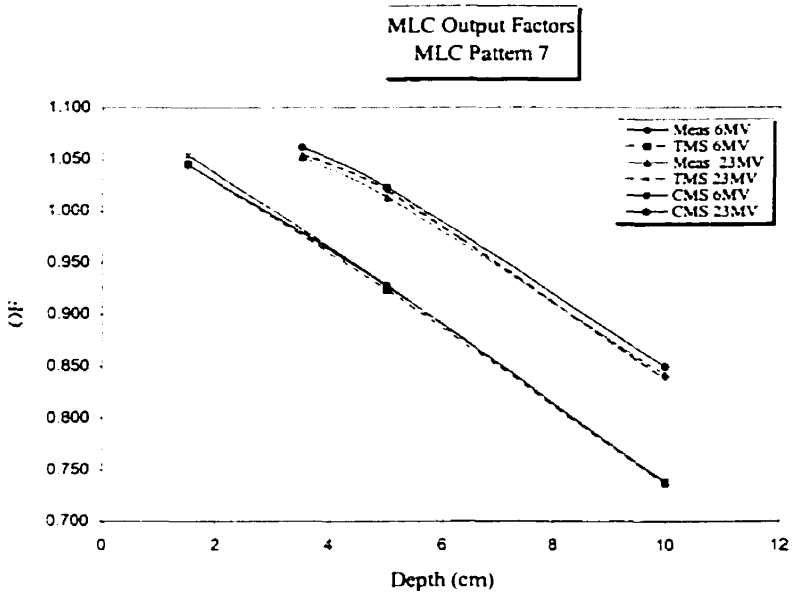

Figure B-26: Output factors for 6MV and 23 MV MLC shaped field (pattern 7). The output is determined in-phantom relative to the output for a 10x10 field at dmax. Measurements were made on Siemens dual energy linear accelerator at the centre of the field. Calculations were performed on Helax TMS and CMS-focus.

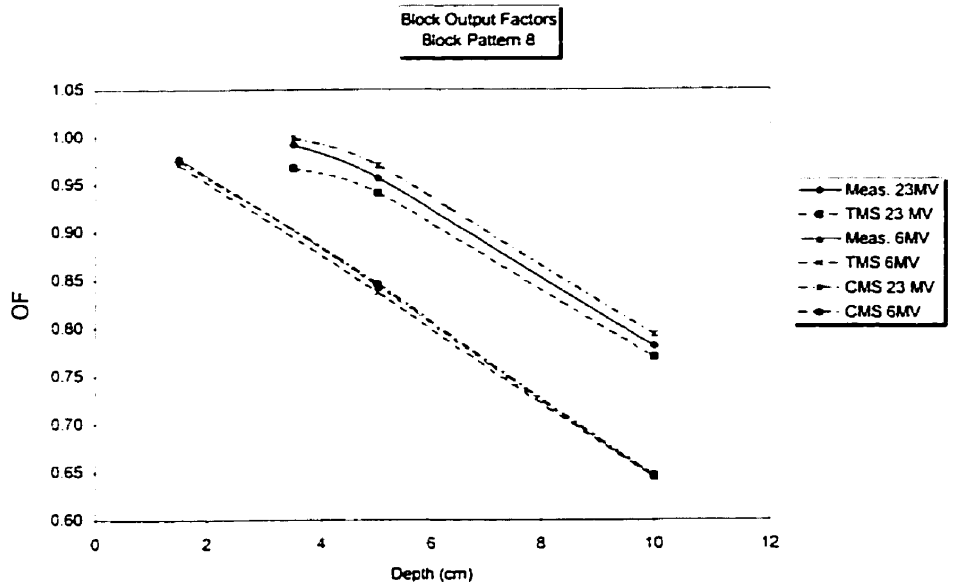

Figure B-27: Output factors for 6MV and 23 MV blocked field pattern 8. The output is determined in-phantom relative to the output for a 10x10 field at dmax. Measurements were made on Siemens dual energy linear accelerator at the centre of the field. Calculations were performed on Helax TMS and CMS-focus.

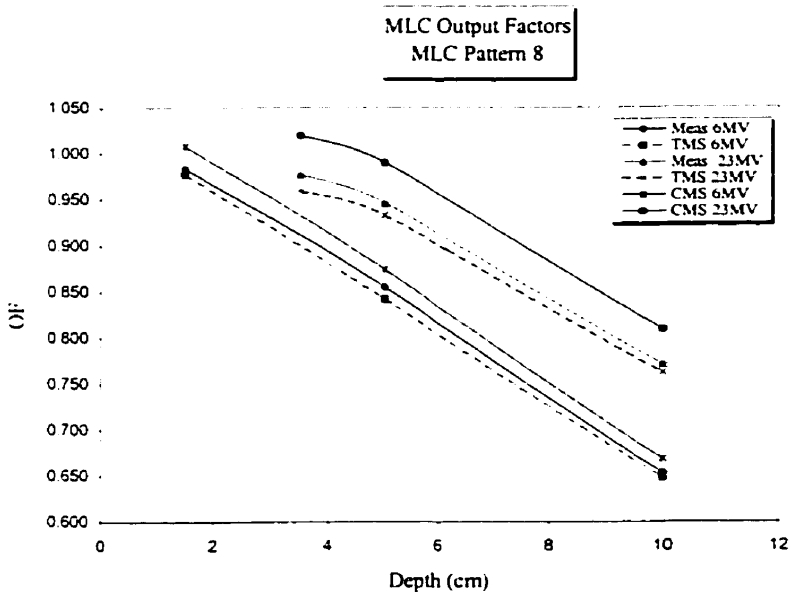

Figure B-28: Output factors for 6MV and 23 MV MLC shaped field (pattern 8). The output is determined in-phantom relative to the output for a 10x10 field at dmax. Measurements were made on Siemens dual energy linear accelerator at the centre of the field. Calculations were performed on Helax TMS and CMS-focus.

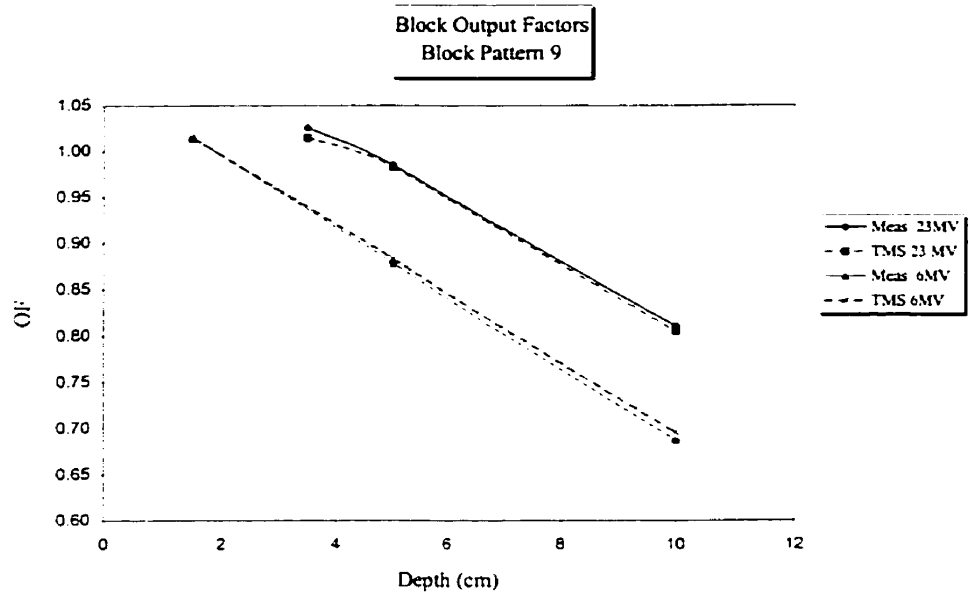

Figure B-29: Output factors for 6MV and 23 MV blocked field pattern 9. The output is determined in-phantom relative to the output for a 10x10 field at dmax. Measurements were made on Siemens dual energy linear accelerator at the centre of the field. Calculations were performed on Helax TMS.

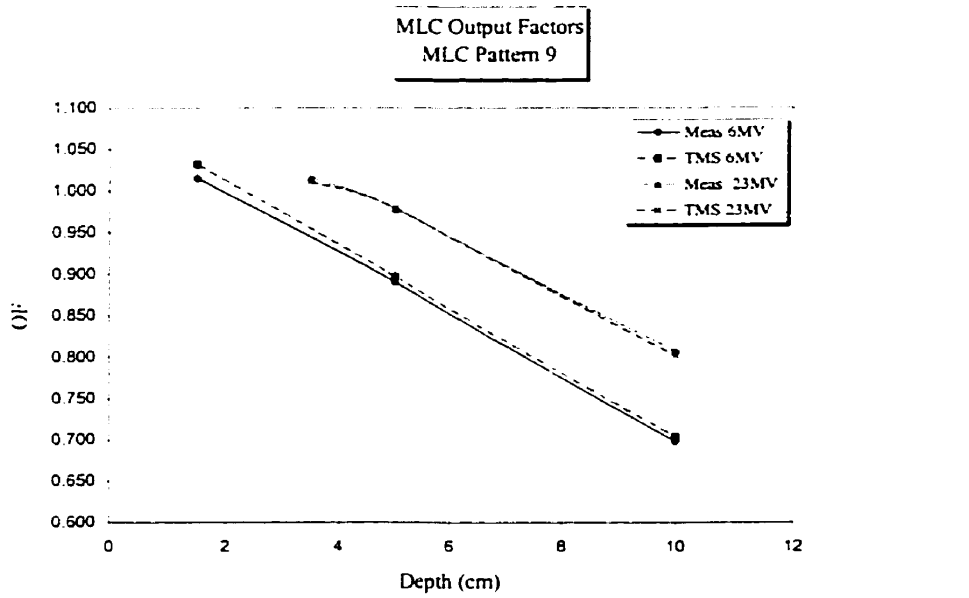

Figure B-30: Output factors for 6MV and 23 MV MLC shaped field (pattern 9). The output is determined in-phantom relative to the output for a 10x10 field at dmax. Measurements were made on Siemens dual energy linear accelerator at the centre of the field. Calculations were performed on Helax TMS.

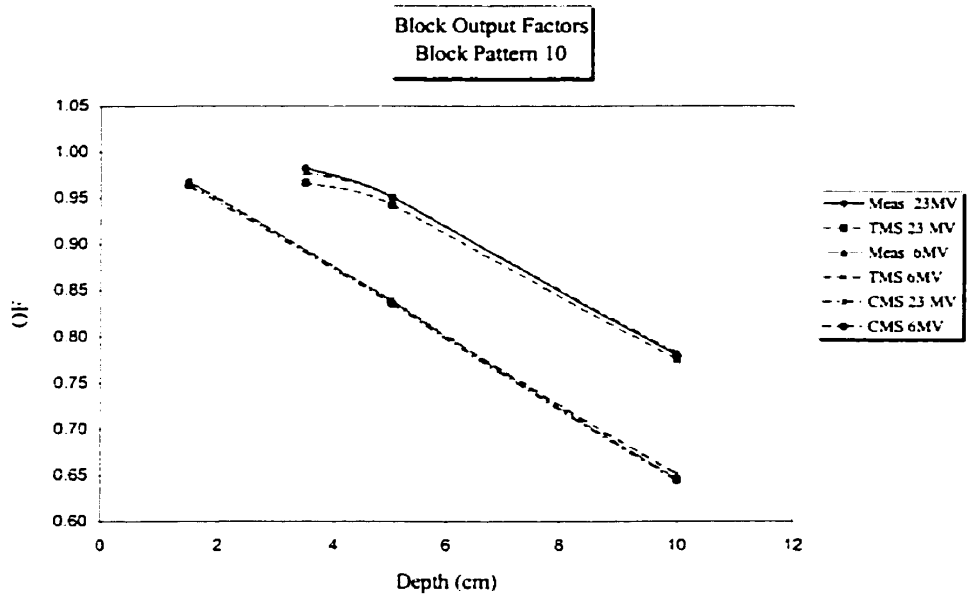

Figure B-31: Output factors for 6MV and 23 MV blocked field pattern 10. The output is determined in-phantom relative to the output for a 10x10 field at dmax. Measurements were made on Siemens dual energy linear accelerator at the centre of the field. Calculations were performed on Helax TMS.

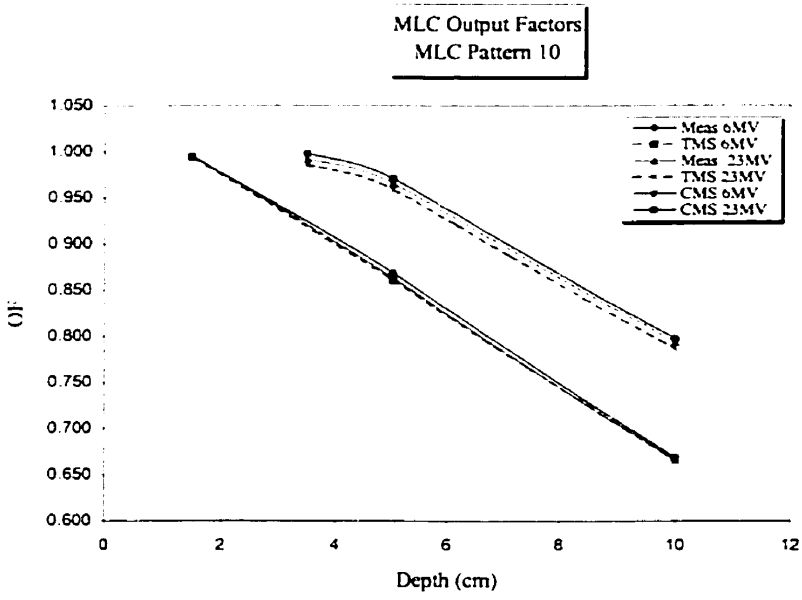

Figure B-32: Output factors for 6MV and 23 MV MLC shaped field (pattern 10). The output is determined in-phantom relative to the output for a 10x10 field at dmax. Measurements were made on Siemens dual energy linear accelerator at the centre of the field. Calculations were performed on Helax TMS.